

UNIVERSITY OF CALIFORNIA
SANTA CRUZ

**A FAST AND PORTABLE HIGH-ORDER IN TEMPORAL
METHOD FOR COMPUTATIONAL FLUID DYNAMICS**

A dissertation submitted in partial satisfaction of the
requirements for the degree of

DOCTOR OF PHILOSOPHY

in

APPLIED MATHEMATICS AND STATISTICS

by

Youngjun Lee

August 2021

The Dissertation of Youngjun Lee
is approved:

Dongwook Lee, Chair

Nicholas Brummell

Hongyun Wang

Peter F. Biehl
Vice Provost and Dean of Graduate Studies

Copyright © by

Youngjun Lee

2021

Table of Contents

List of Figures	v
List of Tables	x
Abstract	xi
Dedication	xii
Acknowledgments	xiii
1 Introduction	1
2 Discretization Methods	10
2.1 Euler Equations	10
2.2 Finite Volume Method	12
2.3 Finite Difference method	14
2.4 Conclusion	17
3 High-Order Methods for FDM	19
3.1 High-Order Reconstruction Schemes	22
3.1.1 Weighted Essentially Non-Oscillatory Methods	24
3.1.2 Gaussian Process Reconstruction	29
3.2 High-Order Time Integration Schemes	40
3.2.1 Strong Stability Preserving Runge-Kutta Methods	40
3.2.2 Lax–Wendroff Type Methods	44
4 System-Free Picard Integral Formulation	47
4.1 Picard Integral Formulation	48
4.2 System-Free Approach	56
4.2.1 The proper choices of ε	58
4.3 Recursive System-Free Approach	61
4.4 System-Free PIF method with Source term	66

4.5	Conclusion	69
5	Results	71
5.1	Performance of SF-PIF method	71
5.1.1	Sine wave advection	72
5.1.2	Nonlinear isentropic vortex advection	75
5.1.3	Sod shock tube problem	80
5.1.4	Impllosion test	82
5.1.5	Shallow water equations	84
5.2	SF-PIF method with WENO-JS	85
5.2.1	The Shu-Osher problem (rotated 45°)	85
5.2.2	2D Riemann problem: Configuration 3	89
5.2.3	Double Mach reflection	91
5.2.4	3D Riemann problem	94
5.3	SF-PIF method with GP-WENO	95
5.3.1	Hyperparameters	96
5.3.2	2D Riemann problem: Configuration 3	98
6	Conclusion	99
	Bibliography	100

List of Figures

- | | |
|---|----|
| 1.1 The numerical test results for measuring errors from different orders of temporal methods combined with the fifth-order spatial method. A numerical experiment of WENO5 with RK3 exhibits a convergence rate degradation from a higher rate of 4.5 following initially the fifth-order spatial accuracy of WENO5 to a lower third-order accuracy of RK3 later on. In WENO5+RK4, the solution continues to converge at 4.5th order without a sudden drop of convergence rate. The situation is even worse for WENO5+RK2 that the solution over the entire range of grid resolutions is bounded to be second-order. | 4 |
| 3.1 The reconstructed profiles in three sub-stencils of the fifth-order WENO-JS scheme. The black dots and horizontal dotted lines represent the volume averaged quantities. Note that there is a sharp discontinuity at $x = x_{i-\frac{1}{2}}$, resulting three different reconstructed pointwise values at $x = x_{i\pm\frac{1}{2}}$ of each polynomial, marked as stars. In ENO perspective, $p_3(x)$ is an appropriate choice, as $S_3 = \{I_i, I_{i+1}, I_{i+2}\}$ does not include the discontinuous point. . . | 26 |

3.2	The reconstructed fifth-order WENO profiles of the same data stencil in Fig. 3.1, combined with WENO-JS nonlinear weights. (Eq. (3.17)) The opacity of each line measures the nonlinear weights on that sub-stencil, and calculated nonlinear weights are noted in the figure. Note that the nonlinear weights of S_3 are dominant over other stencils, S_1 and S_2 , resulting in ENO-style stencil selection.	28
3.3	GP reconstructed profiles with the same data as Figs. 3.1 and 3.2 with different hyperparameters $\ell = 1.0, 1.5, 3.0$. Note that all the reconstructed profiles produce a new local minimum near $x = x_{i+\frac{1}{2}}$, which violates the monotonic-preserving condition and leads to numerical oscillations. The shaded areas represent 95% confidence regions from the posterior variance.	34
3.4	GP-WENO Reconstructed profiles with nonlinear weights with the same data as Fig. 3.3. Hyperparameters $\ell = 2\Delta$ and $\sigma = 2\Delta$ are used. 95% confidence regions are shaded with the corresponding colors, and the opacity of each prediction measures the nonlinear weights on that sub-stencil.	39
5.1	Convergence test for the 1D sine wave advection problem. The errors are calculated in L_1 sense against the initial density profile resolved on the computational grids refined from 32 to 1024 by a factor of 2. All numerical solutions follow the theoretical third-order convergence rate (the black-dotted line) when using the timesteps computed from the Courant condition. Also plotted are the solutions of using reduced timesteps, which follows the fifth-order convergence rate represented in the pink-dotted line.	73

5.2 The L_1 errors of the isentropic vortex advection test problem on different grid resolutions, $N_x = N_y = 50, 100, 200$, and 400 . The three different third-order temporal schemes are used combined with WENO5 spatial method. The L_1 errors with respect to the grid resolutions (left); with respect to the computation time (right).	76
5.3 The L_1 errors of the isentropic vortex advection test problem solved by third- and fourth-order temporal schemes combined with WENO5 spatial method. The L_1 errors with respect to the grid resolutions (left); with respect to the computation time (right).	78
5.4 Sod's shock tube problem at $t = 0.2$. The reference solutions are over-plotted as solid lines in each panel, which are resolved on a grid resolution of $N_x = 1024$ with RK3. The symbols in each panel represent the solution resolved on $N_x = 256$ grid cells with (a) RK3, (b) PIF3, and (c) oSF-PIF3. (d), the solution is resolved with oSF-PIF3 method combining with a new WENO- <i>like</i> numerical differentiate operator, described as in Eqs. (4.19) to (4.22).	81
5.5 The density profile of the implosion test with oSF-PIF3 (left) and with RK3 (right). The color map ranges from 0.3 to 1.2, and 40 evenly-spaced contour lines are over-plotted with the same range.	83
5.6 Snapshots of the circular dam breaking simulation at four different times, $t = 0.345, 0.69, 1.035$, and 1.38 seconds. A volume of water in rest is initially confined in a cylindrical dam of a radius $r = 11$ m and a height $h = 10$ m. The simulation starts with an instantaneous removal of the cylindrical wall located at the center of the domain [$50\text{ m} \times 50\text{ m}$] resolved on a grid resolution of 100×100 . The gravitational force is exerted on the steady water, which triggers the onset of the gravitational collapse of the entire volume of water, making the circular splash in the outer rim as well as the ripple effects in the central region that move radially outward in time.	86

5.7	2D density maps of inclined 2D Shu-Osher test problem at $t = 0$ and $t = 1.8$. The test was performed on a 2D simulation box of 1024×1024 resolution with the SF-PIF4 method. The solid black line represents the shock propagating direction, x_{\parallel} , and squares divide the line in each quartile.	88
5.8	One dimensional density profiles along the x_{\parallel} direction of the inclined Shu-Osher problem at $t = 1.8$. The solid line represents the reference solution, solved by RK4 with 1024 data points in the diagonal axis, i.e., $N_{\parallel} = 1024$. All other solutions, represented by the symbols, are resolved on an $N_{\parallel} = 256$ grid resolution in the diagonal axis. The detailed view of the high-frequency region is shown on the right panel.	88
5.9	The density maps of Configuration 3 at $t = 0.8$. Left column: The solutions using RK3 (top) and SF-PIF3 (bottom). Right column: The solutions using RK4 (top) and SF-PIF4 (bottom). Forty levels of black contour lines are over-plotted in each figure with the same range of the color map. All simulations are performed on a 1600×1600 grid resolution.	90
5.10	The solution density profile of Double Mach reflection test solved with SF-PIF4 method on a 4096×2048 grid resolution. The solid black curves represent the forty levels of contour lines ranging within the same range of the colormap. The white-dotted rectangle is the main point of interest in this simulation, where the jet and the primary triple point are formed. More detailed view of the rectangle region with different temporal solvers are plotted in Fig. 5.11.	92

5.11 The density map of the double Mach reflection test at $t = 0.25$ zoomed-in near the jet. Forty levels of contour lines are over-plotted in solid black curves with the same range of the color map. All simulation results are performed on a 4096×2048 grid resolution. Left column: The solutions using RK3 (top) and SF-PIF3 (bottom). Right column: The solutions using RK4 (top) and SF-PIF4 (bottom).	93
5.12 The density maps of the 3D Riemann problem test at $t = 0.53$. Forty contour lines are over-plotted. The left panels show each face's geometrical views, while the right panels show the detailed picture of the diagonal planes. All simulations are performed on a $256 \times 256 \times 256$ grid resolution, solved with RK4 (top) and SF-PIF4 (bottom) solvers. The Courant condition, $C_{\text{cfl}} = 0.3$ is used for calculating the timestep.	94
5.13 The log of L_1 errors of vortex advection problem solved by GP-WENO and SF-PIF3 on a 400×400 grid resolution. The radius of GP-WENO stencil is $r = 2$, which is the same stencil size of the fifth-order WENO method. The white dotted-lines are represent the hyperparameters of minimum error.	97
5.14 The slices of Fig. 5.13 at the minimum error. The horizontal dotted line is the target error obtained from WENO method with same configurations.	97

List of Tables

5.1	The L_1 errors, the rates of convergence, and the relative computation times for the vortex advection test. Here, the comparison between RK3 and oSF-PIF is only displayed, since the difference between oSF-PIF3 and PIF3 is indistinguishable. All the performance results (measured in seconds) are averaged over 10 simulation runs which are conducted on a Coffee Lake quad-core i7 Intel CPU with a clock speed of 2.7GHz, Turbo Boost up to 4.5GHz, utilizing four parallel threads.	77
5.2	The L_1 errors, the rates of convergence, and the computation times for the vortex advection test solved using RK3 and SF-PIF3 methods (top); using RK4 and SF-PIF4 methods (bottom). All simulation runs are performed on the four 20-cores Cascade Lake Intel Xeon processors, utilized 64 parallel threads. CPU times are measured in seconds, averaged over 10 individual runs.	79
5.3	Performance results for the 3DRP test problem. All performance results (measured in seconds) are averaged over five simulation runs conducted on 16 nodes. Each node has $2 \times$ 20-core Intel Xeon Gold 6248 (Cascade Lake) CPUs, and the simulation utilized 512 parallel threads for each run.	95

Abstract

A Fast and Portable High-Order in Temporal Method for Computational Fluid Dynamics

by

Youngjun Lee

A clear, concise abstract explaining the why, what, and how of your work.

A loving dedication.

Acknowledgments

The text of this dissertation includes reprints of the following previously published material:

- Youngjun Lee and Dongwook Lee. A single-step third-order temporal discretization with jacobian-free and hessian-free formulations for finite difference methods. *Journal of Computational Physics*, 427:110063, 2021.
- Youngjun Lee, Dongwook Lee, and Adam Reyes. A recursive system-free single-step temporal discretization method for finite difference methods. *Journal of Computational Physics: X*, 12:100098, 2021.

The primary co-author Dongwook Lee listed in these publications directed and supervised the research which forms the basis for this dissertation.

Chapter 1

Introduction

In past decades, the rapid evolution of the high-performance computing (HPC) systems offers growing computational capacity for the numerical simulations of various scientific fields, where conducting a direct experiment is extremely expensive or notoriously complicated. As the computing power of HPC systems gradually increases, scientists can compute more complex and computationally intensive physical models such as visualizing black holes [40, 1], simulating nuclear fusions [37, 31], studying laser-plasma interactions [53, 82], to name a few.

In order to simulate these physical phenomena, it demands meticulously designed numerical algorithms for solving nonlinear, multidimensional, and multi-physics equations judiciously. Generally speaking, numerical algorithms require more computational power for better solution accuracy, i.e., using high-resolution grid configuration.

However, the recent hardware development trend – the progression of the memory capacity per compute core has become gradually saturated [4] – is compelling the HPC community to find more efficient ways that can best exercise computing resources in pursuing computer simulations. As reported in 2014 [26], decreasing memory density per compute core will be the primary limiting factor to the

scalability of scientific simulation codes.

To meet this end, modern practitioners have relentlessly delved into advancing high-arithmetic-intensity models that can increase numerical accuracy per degree of freedom while operating with reduced memory requirements and data transfers in HPC architectures. For example, in the computational fluid dynamics (CFD) community, one such computing paradigm is to promote high-order methods in which high arithmetic intensity is achieved by using an increasing number of higher-order terms. Due to its high availability in increasing the quality of numerical solutions with fewer grid points, high-order discrete methods for hyperbolic conservation laws have become primary themes in the CFD community.

Under the dual computational need for accuracy and stability, the CFD community has developed high-order reconstruction and interpolation strategies that can achieve spatially high-order approximation. [84, 20, 51, 41, 13, 16, 54, 7]

For example, in the Piecewise Parabolic Method (PPM) [84], the given data is considered a profile with piecewise quadratic polynomials, ensuring third-order spatial accuracy of the PPM reconstruction/interpolation. The PPM uses Total Variable Diminishing (TVD) slope limiters to piecewise profiles to enhance the numerical stability in the sharp gradient regions. The robustness and compactness of PPM attract scientists in the CFD community, and it is considered a central “high-order” strategy even today.

On the other hand, the Weighted Essentially Non-Oscillatory (WENO) method [41], the improved version of the ENO method [38], takes a different route to strengthen the polynomial-based profile’s stability. The WENO method divides the given stencil into smaller sub-stencils and considers lower-order polynomials in each sub-stencil. Then, by taking a convex combination of each sub-polynomials with nonlinear weighting factors, the WENO method constructs high-order, shock-

capturing profiles in each stencil. The nonlinear weights are designed in a way that converges to the linear weights in a smooth region. (i.e., the convex combination in a smooth region is equivalent to the high-order, linear polynomial in a whole stencil) Therefore, the WENO method can be interpreted as a piecewise profile consists of varying degrees of polynomials depending on the local smoothness of the given data.

A recent study from Reyes et al. [61, 62] introduced a new high-order reconstruction/interpolation strategy without considering the polynomial functions. This new design concept utilizes Gaussian Process (GP) to estimate the data at an arbitrary point in high-order accuracy instead of constructing polynomial functions. The GP method can be combined with the WENO weighting scheme to bringing the non-oscillatory feature of the WENO method. The WENO-weighted GP method, called the GP-WENO method, employs the marginal likelihood function of GP to measure the smoothness of the given data instead of considering spatial derivatives in the conventional WENO method. The GP-WENO method demonstrated a high-order spatial accuracy and stability with a compact structure in the conventional finite volume discretization and the primitive-variable-based finite difference method.

In order to achieve highly accurate numerical solutions, the high-order temporal method must be considered alongside the spatial method since the solution lies in a spatiotemporal plane. Generally speaking, two different cases can be considered to determining the order of accuracy: the leading error term from the p -th order spatial method is dominant over the q -th order temporal error, $\mathcal{O}(\Delta s^p) > \mathcal{O}(\Delta t^q)$ or *vice versa*, $\mathcal{O}(\Delta s^p) < \mathcal{O}(\Delta t^q)$. Practically, many research articles about the high-order spatial methods for solving CFD simulation use the mediocre low-order temporal methods combined with the high-order spatial meth-

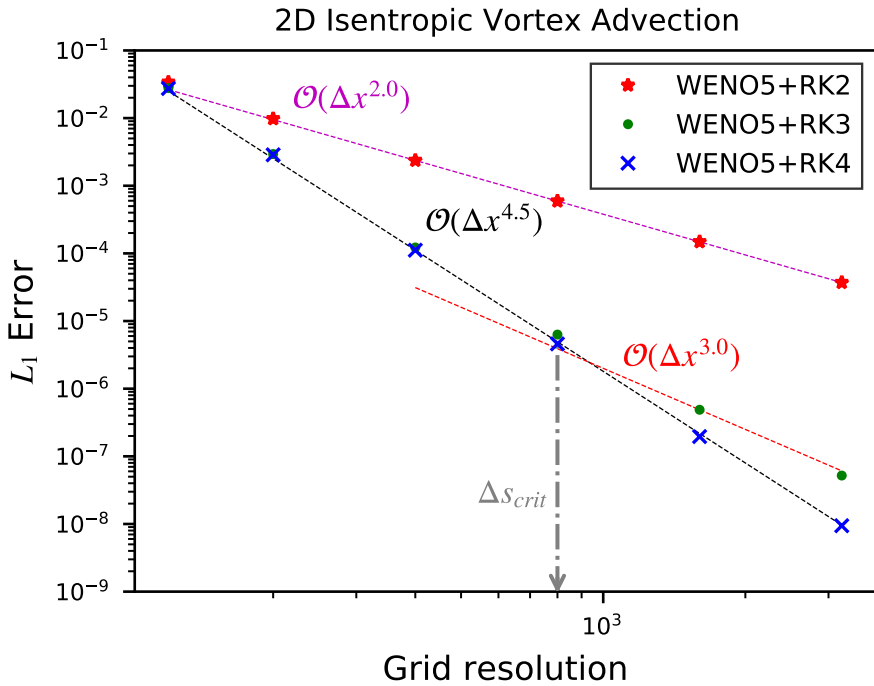


Figure 1.1: The numerical test results for measuring errors from different orders of temporal methods combined with the fifth-order spatial method. A numerical experiment of WENO5 with RK3 exhibits a convergence rate degradation from a higher rate of 4.5 following initially the fifth-order spatial accuracy of WENO5 to a lower third-order accuracy of RK3 later on. In WENO5+RK4, the solution continues to converge at 4.5th order without a sudden drop of convergence rate. The situation is even worse for WENO5+RK2 that the solution over the entire range of grid resolutions is bounded to be second-order.

ods. These combinations showed a reasonable convergence rate between p and q , meaning that the spatial error is dominant over the temporal error even with a lower order of temporal accuracy, $q < p$.

However, as reported in [49], this occurrence is flipped to other ends, i.e., temporal errors are dominant over spatial errors, particularly in a fine grid configuration. As shown in Fig. 1.1, a critical grid delta Δs_{crit} exists so that the error associated with a q -th order temporal method is comparable to and becoming dominant over the error of a p -th order spatial solver with $q < p$. This creates

a computational dilemma of not making further enhancements in solution accuracy, particularly when computational grids are progressively refined locally to put more grid resolutions for improved solution quality, such as in an adaptive mesh refinement (AMR) configuration.

Here lies the dire need for an efficient and accurate temporal scheme in predictive science territories of CFD to acquire highly accurate numerical solutions with steadfast fidelity. Although a method bearing high-order accuracy conveys the nexus of mathematical significance on its right, the performance of such a high-order method should also be accompanied by computational efficiency.

For decades, multi-stage time integrators have been considered as the standard temporal integration strategy for an extensive range of high-order numerical schemes for partial differential equation (PDE) solvers. Specifically, the Strong Stability Preserving Runge-Kutta (SSP-RK) method [35, 36, 34] is the most popular high-order time integration scheme in the CFD community. The SSP-RK method is based on the well-known ordinary differential equation (ODE) solver, the Runge-Kutta (RK) method, enforcing TVD property in each sub-stage of the RK method. The SSP-RK methods have proven high fidelity and robustness in acquiring high-order accuracy and numerical stability in compact, straightforward numerical structures.

The number of sub-stages determines the order of accuracy of the RK method in general, i.e., q multiple sub-stages for the q -th order RK method. For example, the third-order RK method integrates the solution over three sub-stages. The optimal third-order SSP-RK method also has three sub-stages with different coefficients, which ensure the TVD property. However, higher than third-order SSP-RK schemes require more sub-stages to achieve the TVD limitation. It is reported in [35], the four-stage, fourth-order SSP-RK method cannot be formu-

lated with positive coefficients, meaning that the classical four-stage, fourth-order RK4 is not SSP. Other authors have demonstrated that SSP-RK4 with positive coefficients could be constructed with increasing sub-stages from five up to eight [73, 74], requiring more computational costs.

Even though its portability and compactness for achieving high-order temporal accuracy, the multi-stage time integrators are less attractive in a perspective of efficiency due to their increasing computational costs with the order of accuracy. For instance, the high-order spatial method and boundary conditions should be applied at each sub-stage of the SSP-RK scheme, which makes the overall procedure of SSP-RK computationally expensive. In parallel simulations, these operations also increase the footprint of data movements between node communications as the number of sub-stages grows. This very nature of SSP-RK makes it less efficient for massively parallel simulations, particularly when the level of adaptive mesh refinement (AMR) progressively builds up around interesting features in simulations.

To circumvent the said issues in SSP-RK, practitioners have taken a different route of providing a high-order temporal updating strategy for solving numerical PDEs. The core design principle lies in formulating a conservative temporal integrator that works for nonlinear PDEs in multiple spatial dimensions with the equivalent high-order accuracy as in SSP-RK, but, this time, in a single-stage, single-step update. One famous strategy is to modifying the Lax-Wendroff scheme [46], which uses a time-Taylor expansion of the conservative variables to achieve high-order temporal accuracy.

The effort in this direction has resulted in the Arbitrary high order DERivative (ADER) method, which was first introduced in [80] for linear equations. Since then, ADER schemes have gone through several generations of a breakthrough by

numerous authors with the common goal of meeting the high-order requirement in a compact single-step update.

The original ADER method proposed by Toro and his collaborators [80, 76, 78] achieve high-order temporal accuracy by solving a series of generalized Riemann problems (GRPs) for temporal derivatives of the conservative variables at cell interfaces. The temporal derivatives are obtained by applying the so-called Lax-Wendroff or Cauchy-Kowalewski (LW/CK) procedure similar to the original Lax-Wendroff method. The primary purpose of the LW/CK procedure is to convert time derivatives to spatial derivatives, which are coupled through Jacobians and Hessians.

The ADER formulation has been further taken to a more modern direction. Balsara et al. [9] presented a new compact ADER framework that replaced the usual Cauchy-Kowalewski procedure in the original ADER formalism with a local continuous space-time Galerkin formulation up to fourth-order and called the new approach ADER-CG (CG for continuous Galerkin). The ADER-CG schemes are shown to be approximately twice faster than the SSP-RK methods at the same order of accuracy [8].

The Picard integral formulation (PIF) method, proposed by Christlieb et al. [19], is another single-stage time integration strategy based on the Lax-Wendroff time discretization method under the finite difference formulation. The conventional finite difference method takes the pointwise representation of data; however, the PIF method takes time-averaged quantities to achieve high-order temporal accuracy. The time-averaged data is constructed through a time-Taylor expansion, and the LW/CK procedure is used to obtain coefficients of the Taylor series. Christlieb and his collaborators demonstrated that LW/CK procedures could successfully be utilized for obtaining high-order terms of the numerical fluxes for

a single-stage update as in many Lax-Wendroff type works of literature. Other studies also have shown that single-step temporal updates are more efficient in terms of CPU time to a solution when compared to multi-stage/multi-step methods [8, 47, 48].

Nonetheless, single-stage time integrators are still less popular choices in the CFD community. Designing a single-stage method generally brings more complicated and sophisticated mathematical structures than the SSP-RK method, requiring more implementation efforts. A recent study from Montecinos [56] proposed a simplification of the LW/CK procedures in the context of the implicit Taylor series. The idea is to generalize the recursive LW/CK procedure by considering the Jacobian matrix as a function of space and time. The ADER-Taylor method [60, 58, 59] is another way to reduce the number of LW/CK calculations by adopting the Differential Transform (DT) method for high-order derivatives.

The flux Jacobians and Hessians are another implementation hurdle/bottleneck for the Lax-Wendroff type schemes. Performing LW/CK procedures to convert the time derivatives to spatial derivatives requires explicit forms of the Jacobians ($\partial_{\mathbf{U}} \mathbf{F}$), Hessians ($\partial_{\mathbf{U}}^2 \mathbf{F}$), and higher derivatives of the flux functions ($\partial_{\mathbf{U}}^k \mathbf{F}$) on high-order schemes. Finding analytical derivations of *Jacobian-like* terms is a notoriously cumbersome process, specifically for nonlinear systems. For example, in the Euler equations, the flux Jacobians are 5×5 matrices in three spatial dimensions, and the flux Hessians are $5 \times 5 \times 5$ rank three tensors. For constructing higher than third-order temporal accuracy through the LW/CK procedure, it is required to have analytic forms of the third-order derivatives of the flux functions with respect to the conservative variables, e.g., $\partial_{\mathbf{U}}^3 \mathbf{F}$. These terms are then $5 \times 5 \times 5 \times 5$ rank four tensors, which makes the LW/CK procedure less appealing in fourth- or fifth-order temporal methods.

Another limitation on *Jacobian-like* terms is the dependency on the system of equations. Since the Jacobian-like terms are based on the flux functions of the governing equations of the system, the hard-coded *Jacobian-like* terms should be re-derived and re-implemented whenever to change the system of equations. For example, the high-order scheme solving Euler equations that uses *Jacobian-like* terms needs to be modified to solve other systems, such as Magnetohydrodynamics (MHD) equations.

In this regard, this dissertation develops a single-stage, high-order time integration scheme for hyperbolic PDEs under finite difference formulation. The core design concept is to achieve high-order accuracy within a single step to reduce computational costs and data communications between parallel nodes. Alongside the computational efficiency, the newly developed high-order temporal scheme is sufficiently accurate to maintain the order of accuracy of the spatial methods, even for the fine grid configurations. Another important objective for designing a high-order time integrator in this dissertation is to increase its portability. By designing a time integrator independent of the system of equations, one can provide increased flexibility and ease of code implementation.

Consequently, a newly developed time integrator showed more than two times faster performance gain than the conventional multi-stage methods. Also, it can readily replace only the temporal part of any existing simulation code independent of system of equations.

Chapter 2

Discretization Methods

This dissertation interests in solving the general conservation laws of hyperbolic PDEs, predicting numerical solutions with high-order accuracy. This chapter introduces two general ways to discretize the Euler equations, which will be of particular interest in this dissertation.

2.1 Euler Equations

In three dimensions, the conservation laws may be written as,

$$\partial_t \mathbf{U} + \nabla \cdot \mathcal{F}(\mathbf{U}) = \partial_t \mathbf{U} + \partial_x \mathbf{F}(\mathbf{U}) + \partial_y \mathbf{G}(\mathbf{U}) + \partial_z \mathbf{H}(\mathbf{U}) = 0, \quad (2.1)$$

where \mathbf{U} is a vector of conserved variables and $\mathcal{F} = (\mathbf{F}(\mathbf{U}), \mathbf{G}(\mathbf{U}), \mathbf{H}(\mathbf{U}))^T$ is the flux function in the x , y , and z directions. The conservation law is considered hyperbolic if the flux Jacobian has only real eigenvalues and is diagonalizable. Thus,

$$\mathbf{A} = \partial_{\mathbf{U}} \mathbf{F} = \mathbf{R} \boldsymbol{\Lambda} \mathbf{L}, \quad (2.2)$$

where \mathbf{A} is the flux Jacobian in x -direction, $\mathbf{\Lambda}$ is a diagonal matrix with real eigenvalues, and \mathbf{L} and \mathbf{R} are corresponding left and right eigenvectors.

This dissertation focuses on solving Euler equations, which govern compressible, adiabatic inviscid flow. In the Euler equations, the conserved variables and the flux functions are defined as,

$$\mathbf{U} = \begin{bmatrix} \rho \\ \rho u \\ \rho v \\ \rho w \\ E \end{bmatrix}, \quad \mathbf{F}(\mathbf{U}) = \begin{bmatrix} \rho u \\ \rho u^2 + p \\ \rho u v \\ \rho u w \\ u(E + p) \end{bmatrix}, \quad \mathbf{G}(\mathbf{U}) = \begin{bmatrix} \rho v \\ \rho u v \\ \rho v^2 + p \\ \rho v w \\ v(E + p) \end{bmatrix}, \quad \mathbf{H}(\mathbf{U}) = \begin{bmatrix} \rho w \\ \rho u w \\ \rho v w \\ \rho w^2 + p \\ w(E + p) \end{bmatrix}. \quad (2.3)$$

In the above equations, ρ is the density, $\mathbf{u} = (u, v, w)^T$ is the velocity, E is the total energy, and p is the pressure of the fluid. E , the total energy of the fluid represents the sum of internal and kinetic energy,

$$E = \epsilon + \frac{1}{2}\rho\mathbf{u}^2, \quad (2.4)$$

where the internal energy of the fluid, ϵ , obeys the equation of state. (EOS) This dissertation uses the ideal gas law:

$$\epsilon = \frac{p}{\gamma - 1}, \quad (2.5)$$

where γ is the specific heat ratio.

In the following, this dissertation uses the Euler equation as an example of the conserved hyperbolic system. However, numerical methods presented in this dissertation are valid for any system of the form of Eq. (2.1). Magnetohydrodynamics (MHD) equations, for example, the general numerical strategies will

be nearly identical to the Euler equations except for the solenoidal constraint of the magnetic field. ($\nabla \cdot \mathbf{B} = 0$) Thus, the high-order methods presented in this dissertation can be applied to the MHD simulation code easily.

2.2 Finite Volume Method

The popular way to consider discretized variables for the conserved system is to cast volume integrals to the governing equations, called the finite volume method. (FVM) Consider Eq. (2.1) discretized on a uniform grid containing cells with equal spacing ($\Delta x, \Delta y, \Delta z$) in the three spatial dimensions. Then, each cell's center can be indexed by (i, j, k) at (x_i, y_j, z_k) and the cell's face centers at each interface by $(i \pm \frac{1}{2}, j, k), (i, j \pm \frac{1}{2}, k), (i, j, k \pm \frac{1}{2})$. Taking the volume average of each computational cell ($\frac{1}{V_{ijk}} \int_{V_{ijk}} \mathcal{F}(\mathbf{U}) \cdot d\mathcal{V}$) to Eq. (2.1) and applying the divergence theorem, we have,

$$\frac{1}{V_{ijk}} \int_{V_{ijk}} \partial_t \mathbf{U} d\mathcal{V} + \frac{1}{V_{ijk}} \oint_{S_{ijk}} \mathcal{F}(\mathbf{U}) \cdot \mathbf{n} d\mathcal{S} = 0, \quad (2.6)$$

where V_{ijk} is the volume of the cell at i, j, k , and S_{ijk} is the surrounding surfaces of the cell at i, j, k .

The semi-discretized form of FVM representation of the conserved system is obtained by substituting the dimensionally split flux functions $(\mathbf{F}(\mathbf{U}), \mathbf{G}(\mathbf{U}), \mathbf{H}(\mathbf{U}))$:

$$\begin{aligned} \partial_t \overline{\mathbf{U}}_{i,j,k} = & - \frac{1}{\Delta x} \left(\widetilde{\mathbf{F}}_{i+\frac{1}{2},j,k} - \widetilde{\mathbf{F}}_{i-\frac{1}{2},j,k} \right) \\ & - \frac{1}{\Delta y} \left(\widetilde{\mathbf{G}}_{i,j+\frac{1}{2},k} - \widetilde{\mathbf{G}}_{i,j-\frac{1}{2},k} \right) \\ & - \frac{1}{\Delta z} \left(\widetilde{\mathbf{H}}_{i,j,k+\frac{1}{2}} - \widetilde{\mathbf{H}}_{i,j,k-\frac{1}{2}} \right). \end{aligned} \quad (2.7)$$

In the above equation, the overline indicates a volume-averaged quantity, while

the tilde indicates a surface average at half-indexed cell face. Note that the above semi-discretized form of FVM scheme is a purely analytical result without any numerical approximation. The numerical methods are used to estimate surface-averaged fluxes at each cell's interfaces and update the volume-averaged conserved variables to the next time step.

The most common way to approximate interfacial fluxes for FVM solver for Euler equations is to solve the Riemann problem at cell interfaces following the Godunov method [33]. The Riemann problem is composed of a conservation equation with a single discontinuity in its initial condition. As firstly introduced by Godunov in [33], the Riemann solver (\mathcal{RS}) gives a numerical flux across the discontinuity in the Riemann problem. For example, the numerical flux across the discontinuity at $x_{i+\frac{1}{2},j,k}$ can be calculated as,

$$\hat{\mathbf{f}}_{i+\frac{1}{2},j,k} = \mathcal{RS}(\mathbf{U}_{i+\frac{1}{2},j,k}^L, \mathbf{U}_{i+\frac{1}{2},j,k}^R). \quad (2.8)$$

The precedent task for solving the Riemann problem is to determining Riemann states at interfaces. Note that the inputs of the Riemann solver are regarded as *pointwise* values, $(\mathbf{U}_{i+\frac{1}{2},j,k}^L, \mathbf{U}_{i+\frac{1}{2},j,k}^R)$ while the fundamental data type of FVM is the *volume-averaged* values. $(\bar{\mathbf{U}}_{i,j,k})$ To specify the pointwise Riemann states at interfaces with given volume-averaged conserved variables, they must be reconstructed from the neighboring volume-averaged quantities. For example, a one-dimensional stencil with radius= r , the left Riemann states at $i+\frac{1}{2}$ can be reconstructed from cell-centered volume-averaged conserved variables $(\bar{\mathbf{U}}_{i-r,j,k}, \dots, \bar{\mathbf{U}}_{i,j,k}, \dots, \bar{\mathbf{U}}_{i+r,j,k})$, using p -th order accurate reconstruction operator $\mathcal{R}(\cdot)$:

$$\mathbf{U}_{i+\frac{1}{2},j,k}^L = \mathcal{R}(\bar{\mathbf{U}}_{i-r,j,k}, \dots, \bar{\mathbf{U}}_{i+r,j,k}) + \mathcal{O}(\Delta x^p). \quad (2.9)$$

The spatial order of accuracy, p , of the FVM solver is thereby determined by choice of the reconstruction operator, $\mathcal{R}(\cdot)$ which will be discussed in [find my ref!](#).

It is important to note that the numerical flux resulting from the Riemann solver is also a pointwise representation, while the surface-averaged fluxes $(\tilde{\mathbf{F}}_{i \pm \frac{1}{2}, j, k}, \tilde{\mathbf{G}}_{i, j \pm \frac{1}{2}, k}, \tilde{\mathbf{H}}_{i, j, k \pm \frac{1}{2}})$ are needed for FVM formulation as presented in Eq. (2.7). This should be addressed thoroughly, as a naive approximation of the pointwise flux to the surface-averaged flux is bounded by second-order accuracy no matter the accuracy of the Riemann states:

$$\begin{aligned}\tilde{\mathbf{F}}_{i+\frac{1}{2},j,k} &= \frac{1}{\Delta y \Delta z} \int_{y_{j-\frac{1}{2}}}^{y_{j+\frac{1}{2}}} \int_{z_{k-\frac{1}{2}}}^{z_{k+\frac{1}{2}}} \mathbf{F}(x_{i+\frac{1}{2}}, y, z) dz dy \\ &= \mathbf{F}_{i+\frac{1}{2},j,k} + \mathcal{O}(\Delta y^2, \Delta z^2).\end{aligned}\quad (2.10)$$

The conventional way to achieve higher than second-order accuracy in FVM solver is to solve the Riemann problem at multiple quadrature points on each face. [77, 52, 86] More recent studies proposed ways to avoid multiple calls of Riemann solver, reconstructing surface-averaged fluxes from pointwise Riemann fluxes, [15, 30] using linear combinations of Riemann fluxes, [28, 27] to name a few.

2.3 Finite Difference method

As it firstly proposed in [70], the finite difference method (FDM) seeks a discretization of the spatial derivatives of the fluxes in *pointwise* representation.

Assuming that there exist numerical fluxes satisfy the conservative form as,

$$\begin{aligned}\partial_t \bar{\mathbf{U}}_{i,j,k} = & -\frac{1}{\Delta x} \left(\hat{\mathbf{f}}_{i+\frac{1}{2},j,k} - \hat{\mathbf{f}}_{i-\frac{1}{2},j,k} \right) \\ & -\frac{1}{\Delta y} \left(\hat{\mathbf{g}}_{i,j+\frac{1}{2},k} - \hat{\mathbf{g}}_{i,j-\frac{1}{2},k} \right) \\ & -\frac{1}{\Delta z} \left(\hat{\mathbf{h}}_{i,j,k+\frac{1}{2}} - \hat{\mathbf{h}}_{i,j,k-\frac{1}{2}} \right),\end{aligned}\quad (2.11)$$

where $\hat{\mathbf{f}}_{i\pm\frac{1}{2},j,k}$, $\hat{\mathbf{g}}_{i,j\pm\frac{1}{2},k}$, $\hat{\mathbf{h}}_{i,j,k\pm\frac{1}{2}}$ are the *pointwise* numerical fluxes in each direction at half-indexed cell-face centers. The remaining task is to identify the numerical fluxes in desired order of accuracy, p , which satisfy,

$$\partial_x \mathbf{F}|_{\mathbf{x}=\mathbf{x}_{ijk}} = \frac{1}{\Delta x} \left(\hat{\mathbf{f}}_{i+\frac{1}{2},j,k} - \hat{\mathbf{f}}_{i-\frac{1}{2},j,k} \right) + \mathcal{O}(\Delta x^p), \quad \mathbf{x}_{ijk} = (x_i, y_j, z_k), \quad (2.12)$$

and similarly in y and z fluxes.

In order to specify the numerical fluxes for FDM, consider the pointwise x -flux $\mathbf{F}(x, y_j, z_k)$ as a one-dimensional cell average of an auxiliary function $\hat{\mathbf{F}}$,

$$\mathbf{F}(x, y_j, z_k) = \frac{1}{\Delta x} \int_{x-\frac{\Delta x}{2}}^{x+\frac{\Delta x}{2}} \hat{\mathbf{F}}(\xi, y_j, z_k) d\xi. \quad (2.13)$$

Then the analytic derivative of Eq. (2.13) at $x = x_i$ in x -direction becomes

$$\partial_x \mathbf{F}|_{x=x_i} = \frac{1}{\Delta x} \left(\hat{\mathbf{F}}(x_{i+\frac{1}{2}}, y_j, z_k) - \hat{\mathbf{F}}(x_{i-\frac{1}{2}}, y_j, z_k) \right). \quad (2.14)$$

Comparing Eq. (2.12) and Eq. (2.14), the numerical fluxes in FDM are obtained with desired order of accuracy, p , if they can be defined with the following relationship with $\hat{\mathbf{F}}$,

$$\hat{\mathbf{f}}_{i+\frac{1}{2},j,k} = \hat{\mathbf{F}}(x_{i+\frac{1}{2}}, y_j, z_k) + \mathcal{O}(\Delta x^p). \quad (2.15)$$

Mathematically speaking, the inverse problem of Eq. (2.15) is exactly the same

as the conventional 1D reconstruction problem in FVM, the operation of which is specifically designed to find the primitive function value $\hat{\mathbf{F}}$ at a certain location (mostly, $x_{i \pm \frac{1}{2}}$) in the i -th cell, given the integral-averaged (or volume-averaged) values \mathbf{F} at nearby stencil points as input. Namely, this can be written as

$$\hat{\mathbf{F}}(\xi, y_j, z_k) = \mathcal{R}(\mathbf{F}_{i-r,j,k}, \dots, \mathbf{F}_{i+r,j,k}) + \mathcal{O}(\Delta x^p), \quad \xi \in [x_{i-\frac{1}{2}}, x_{i+\frac{1}{2}}], \quad (2.16)$$

where $\mathcal{R}(\cdot)$ is a p -th order accurate reconstruction operator that used for FVM formulation in Section 2.2, and will be discussed in [find my ref!](#).

Contrary to FVM, the conservative FDM uses only the pointwise values for constructing numerical strategies, not requiring the data conversion between pointwise and volume-averaged quantities. In addition, the high-order reconstruction schemes used for constructing Riemann states in FVM can be used for constructing numerical fluxes in FDM without intense changes in the simulation code – only a simple change in the input variables for the reconstruction operator. This simplicity in numerical strategy attracts researchers in the CFD community, leading various adoptions in high-order solvers. [41, 68, 54, 19, 65]

Compared to FVM, the major difference of FDM is obtaining high-order numerical fluxes directly from the reconstruction operator. Although it simplifies the numerical schemes, the direct formulation of the numerical fluxes hinders its further modifications while keeping a high-order convergence rate.

For example, the adaptive mesh refinement (AMR) grid configuration [11, 12] requires numerical fluxes splitting between the coarse grid to the fine grid in a conservative manner. Conventionally, this is ensured by an additional flux correction step in FVM formulation. [12] However, in FDM, a different approach should be taken because modifying the high-order numerical fluxes may spoil the order of accuracy. One possible way to maintain conservation across coarse to

the fine grid points is to apply nonlinear interpolation on the conserved variables, imply them as boundary conditions, and distribute the calculated errors among coarse grid points. [66]

Another limitation on the direct formulation of numerical fluxes in FDM is the lack of the option to include substructure in the wave model, which Riemann solver typically does in FVM to resolve certain features better. Del Zanna proposed one alternative way of FDM [22, 23], which views numerical fluxes as the Riemann fluxes with the series of high-order correction terms. This approach can achieve a high-order convergence rate with Riemann fluxes like in FVM, without the additional data type conversions required of conventional FVM. [62]

2.4 Conclusion

Two major discretization strategies for conservative systems have been presented. Both the finite difference and finite volume methods are able to achieve high-order spatial accuracy by reconstructing volume-averaged quantities to the pointwise values.

The finite difference method

- evolves the pointwise conserved variables,
- provides a straightforward framework without data type conversions,
- requires high-order numerical fluxes constructed from the pointwise, cell-centered physical fluxes directly from the high-order reconstruction methods and
- may be delicate with the additional modifications on the numerical fluxes.

The finite volume method

- evolves the volume-averaged conserved variables,
- requires rigorous data type conversions to maintain high-order accuracy,
- requires high-order reconstruction of the Riemann states from the cell-centered conserved variables and
- guarantees the conservation laws over the whole spatiotemporal domain by design.

Chapter 3

High-Order Methods for FDM

As mentioned in Chapter 1, the high-order numerical schemes are ideal for maximizing the solution accuracy on a given grid resolution; thus, they can produce more accurate solutions on a limited memory capacity.

The discretization strategies for conservative PDEs presented in Chapter 2 can achieve high-order solution accuracy both in spatial and temporal dimensions. Typically, the spatial accuracy is determined by the accuracy of the reconstruction scheme used for estimating Riemann states (FVM) or numerical fluxes (FDM) at cells interfaces. On the other hand, the numerical time integration strategy for the semi-discretized form of the conservative PDEs (Eqs. (2.7) and (2.11)) will settle the temporal accuracy. Since the solution lies on the spatiotemporal plane, both the temporal and spatial errors should be contemplated in a controlled manner to analyze the numerical solutions properly.

The fundamental mission of the numerical scheme is to estimate the values on unknown points with given available data in an accurate fashion. One straightforward way is to interpolate/reconstruct the data to form piecewise polynomials and estimate the desired points using the polynomials. In this way, the order of accuracy will be determined by the degree of polynomials; the number of data

points used to interpolate/reconstruct the data in each stencil.

However, nonlinear systems like Euler equations, the main interest in this dissertation, require more sophisticated care in designing high-order numerical methods because the system can form and evolve discontinuity profiles even with smooth initial conditions. Generally speaking, an artless high-degree piecewise polynomial function can not handle the discontinuous profiles and introduces spurious oscillations caused by over- and under-shot profiles of the underlying function. Therefore, the stability of the numerical method must be taken into account for solving hyperbolic PDEs in high-order accuracy.

One way to ensure the stability of the numerical scheme is to limit the total variation (TV) of the solution, called the total variation diminishing (TVD) property. The total variation of the solution in one-dimensional discrete solution u^n at time $t = t^n$ is defined as,

$$TV(u^n) := \sum_i |u_{i+1}^n - u_i^n|, \quad (3.1)$$

and it should be bounded by the total variation of the initial conditions to ensure stability as,

$$TV(u^{n+1}) \leq TV(u^n). \quad (3.2)$$

Van Leer introduced TVD flux limiters to provide TVD property on the piecewise linear functions [83] by limiting the slope of the second-degree polynomial. A simple choice of the TVD slope limiter for the second-degree profile is the minmod slope limiter,

$$\text{minmod}(a, b) = \begin{cases} a, & \text{if } |a| < |b| \text{ and } ab > 0 \\ b, & \text{if } |a| > |b| \text{ and } ab > 0 \\ 0, & \text{if } ab < 0, \end{cases} \quad (3.3)$$

where $a = \frac{u_{i+1} - u_i}{\Delta x}$ and $b = \frac{u_i - u_{i-1}}{\Delta x}$ are the forward and backward slope at the cell I_i centered at $x = x_i$. The TVD slope limiters are also used for the popular third-order scheme, the piecewise parabolic method (PPM) by Woodward and Colella [20], for enforcing the TVD property on the quadratic polynomial.

The TVD property is also crucial in designing high-order temporal integration schemes. In the *method of lines* approximations, the semi-discretized form of PDEs (Eqs. (2.7) and (2.11)) can be viewed as an ordinary differential equation (ODE) system in the temporal axis, which an ODE solver can discretize. Thus, the well-known ODE solver, Runge-Kutta (RK) method, can be used as the time integration method in the method of lines schemes; however, the TVD property must be enforced to preserve the numerical stability. Shu and Osher designed TVD limited Runge-Kutta methods [69, 67] for solving hyperbolic conservation laws. Subsequently, Gottlieb and her collaborators [35, 36, 34] further developed this idea to the strong stability preserving Runge-Kutta (SSP-RK) method, which is by far the most popular high-order time integration method used in the CFD community.

This chapter will introduce general schemes for achieving high-order accuracy both in spatial and temporal dimensions in the finite difference method, which is the main interest in this dissertation. The high-order reconstruction schemes in Section 3.1 predict FDM numerical fluxes at cell interfaces, and they are identical to the reconstruction methods used to predict interfacial Riemann states in FVM. The Runge-Kutta methods and the Lax-Wendroff type methods will be introduced in Section 3.2 for achieving high-order in time accuracy for FDM formulation.

3.1 High-Order Reconstruction Schemes

The high-order reconstruction schemes play a pivotal role in reducing numerical errors on the *spatial axis* for solving discrete PDEs under FVM and FDM formulations. The reconstruction schemes furnish a pointwise representation of the given volume-averaged data; thus, they are suitable for estimating pointwise values with given volume-averaged conserved variables (FVM) or volume-averaged auxiliary functions (FDM). Modern practitioners in the CFD community have focused on designing high-order reconstruction schemes that can generate highly accurate solutions while maintaining numerical stability at discontinuous regions. Examples include the early success of the piecewise parabolic method (PPM) by Colella and Woodward [20], which has been still actively adopted as a shock-capturing partial differential equation (PDE) solver by many CFD users after about four decades since its introduction.

In the finite difference method, the numerical fluxes can be estimated through reconstruction schemes by inputting the pointwise physical fluxes at the cell centers. Assuming that a p -th order reconstruction scheme, $\mathcal{R}(\cdot)$, taking the $2r$ length of stencil centered at cell I_i , and generating estimated pointwise value at $x = x_{i+\frac{1}{2}}$, then the FDM numerical flux $\hat{\mathbf{f}}_{i+\frac{1}{2}}$ at $x = x_{i+\frac{1}{2}}$ can be found by,

$$\hat{\mathbf{f}}_{i+\frac{1}{2}} = \mathcal{R}(\mathbf{F}_{i-r}, \dots, \mathbf{F}_{i+r}) + \mathcal{O}(\Delta x^p). \quad (3.4)$$

However, one additional numerical step should be needed for the robustness of the solution. It is well-known that the upwind numerical fluxes can provide more robust solutions in the CFD community. In FVM, this is achieved by solving the Riemann problem, but for FDM, one separated routine should be considered to provide upwind property in the numerical flux. The flux splitting method

is the general way to yield upwinding numerical flux in FDM by splitting the pointwise fluxes into two components moving towards and away from the interface of interest. For example, one can split the flux function into two parts:

$$\mathbf{F}_i = \mathbf{F}_i^+ + \mathbf{F}_i^-, \quad \mathbf{F}_i^\pm = \frac{1}{2} (\mathbf{F}_i \pm \alpha^k \mathbf{U}_i), \quad (3.5)$$

where α^k is the global maximum characteristic speed of k -th characteristic field, i.e., the maximum absolute value of k -th eigenvalue of flux Jacobian $\partial_{\mathbf{U}} \mathbf{F}$ over the whole domain. This procedure is called the global Lax–Friedrichs flux splitting [41] since we take global maximum for each α^k . The reconstruction method is applied to the positive and negative parts of the fluxes \mathbf{F}_i^\pm to construct numerical fluxes, and then they are collected at each interface:

$$\hat{\mathbf{f}}_{i+\frac{1}{2}} = \hat{\mathbf{f}}_{i+\frac{1}{2}}^+ + \hat{\mathbf{f}}_{i+\frac{1}{2}}^-, \quad \hat{\mathbf{f}}_{i+\frac{1}{2}}^+ = \mathcal{R}(\mathbf{F}_s^+), \quad \hat{\mathbf{f}}_{i+\frac{1}{2}}^- = \mathcal{R}(\mathbf{F}_{s'}^-), \quad (3.6)$$

where the sub-index s represents the stencil ranging from $i - r, \dots, i + r$, while at the same time, $s' = 2i - s + 1$.

Although the global Lax–Friedrichs flux splitting provides improved stability and robustness of the numerical scheme, it also introduces numerical dissipation into the solution. One possible way to minimize the numerical dissipation of the flux splitting is to project the fluxes into the characteristic field, so-called Rusanov Lax–Friedrichs flux splitting. [21, 54] The Rusanov Lax–Friedrichs splitting projects pointwise physical fluxes to the left- and the right-going parts according to the characteristic decomposition of the Jacobian matrix,

$$\partial_{\mathbf{U}} \mathbf{F}|_{\mathbf{U}_{i+\frac{1}{2}}} = \mathbf{R}_{i+\frac{1}{2}} \boldsymbol{\Lambda}_{i+\frac{1}{2}} \mathbf{L}_{i+\frac{1}{2}}, \quad \mathbf{U}_{i+\frac{1}{2}} = \frac{\mathbf{U}_i + \mathbf{U}_{i+1}}{2}, \quad (3.7)$$

where \mathbf{R} and \mathbf{L} are the matrices of right and left eigenvectors, and $\mathbf{\Lambda}$ is the diagonal matrix whose diagonal entries are corresponding eigenvalues. The projection proceeds to construct s different left-going ($-$) and right-going ($+$) characteristic states of the pointwise fluxes, denoted as $\mathbf{V}_{(i+\frac{1}{2}):s}^{k,\pm}$ to the cell interface $i + \frac{1}{2}$ as

$$\begin{aligned}\mathbf{V}_{(i+\frac{1}{2}):s}^{k,+} &= \frac{1}{2} \mathbf{L}_{i+\frac{1}{2}}^k \cdot (\mathbf{F}_s + \alpha^k \mathbf{U}_s), \\ \mathbf{V}_{(i+\frac{1}{2}):s}^{k,-} &= \frac{1}{2} \mathbf{L}_{i+\frac{1}{2}}^k \cdot (\mathbf{F}_{s'} - \alpha^k \mathbf{U}_{s'}).\end{aligned}\quad (3.8)$$

Again, s and s' are representing the stencil $s = i - r, \dots, i + r$, $s' = 2i - s + 1$, and the superscript k represents each characteristic field. The coefficient α^k is chosen to be the maximum absolute value of the k -th characteristic speed over the entire computational domain, resulting in the so-called global Lax-Friedrichs flux splitting. The projected fluxes will be taken into the reconstruction scheme and projected back to the numerical fluxes:

$$\hat{\mathbf{f}}_{i+\frac{1}{2}} = \sum_k \left(\hat{\mathbf{V}}_{i+\frac{1}{2}}^{k,+} + \hat{\mathbf{V}}_{i+\frac{1}{2}}^{k,-} \right) \mathbf{R}_{i+\frac{1}{2}}^k, \quad \hat{\mathbf{V}}_{i+\frac{1}{2}}^{k,\pm} = \mathcal{R} \left(\mathbf{V}_{(i+\frac{1}{2}):s}^{k,\pm} \right). \quad (3.9)$$

3.1.1 Weighted Essentially Non-Oscillatory Methods

Generally speaking, the high-order reconstruction schemes based on the polynomial approach assuming that there exists a unique polynomial $\phi(x)$ satisfies volume-averaging conditions:

$$\frac{1}{\Delta x} \int_{I_k} \phi(x) dx = \bar{q}_k, \quad I_k \in S \quad (3.10)$$

where k is the index of cell within a stencil S and \bar{q}_k is a volume-averaged quantity at k . However, when S contains a strong gradient of the volume-averaged data \bar{q}_k , then it suffers from spurious oscillations since the polynomial $\phi(x)$ is assumed to

be smooth over the stencil. Handling discontinuous profiles is essential in solving Euler equations, as it can form discontinuous profiles even with smooth initial conditions.

In 1987, Harten et al. [38] proposed an essentially non-oscillatory (ENO) scheme that chooses the appropriate stencil adaptively to avoid containing any discontinuities in the stencil. In ENO methods, the non-oscillatory stencil is chosen by considering all possible stencils of the required size and measure the smoothness on each of them. Liu et al. [51] improved this idea by introducing the weighted essentially non-oscillatory (WENO) scheme, which takes a convex combination of all possible stencils, reducing the number of logical calculations needed for the original ENO scheme. The WENO scheme was further improved by Jiang and Shu [41] and became one of the most popular high-order reconstruction and interpolation methods for solving shock-dominant CFD simulation.

Conventionally, WENO method with m sub-stencils uses $2m - 1$ data points and ensures $2m - 1$ order of accuracy in a smooth region. As an example, the popular five-points, fifth-order WENO-JS [41] method is presented below.

Consider three sub-stencils,

$$S_m = \{I_{i-3+m}, I_{i-2+m}, I_{i-1+m}\}, \quad m = 1, 2, 3, \quad (3.11)$$

then the second degree polynomials $p_m(x)$ can be constructed on each S_m as,

$$\int_{I_k} p_m(x) dx = \bar{q}_k, \quad I_k \in S_m. \quad (3.12)$$

The reconstructed profiles are depicted in Fig. 3.1. With three sub-polynomials, the reconstructed pointwise values at the cell interfaces $q_{i \pm \frac{1}{2}}$ can be represented

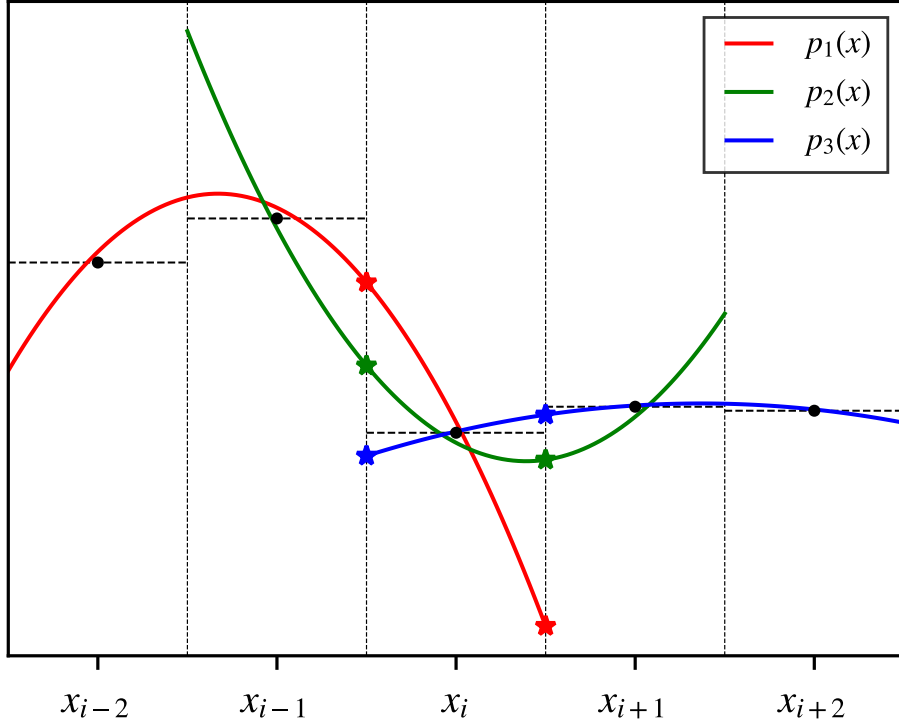


Figure 3.1: The reconstructed profiles in three sub-stencils of the fifth-order WENO-JS scheme. The black dots and horizontal dotted lines represent the volume averaged quantities. Note that there is a sharp discontinuity at $x = x_{i-\frac{1}{2}}$, resulting three different reconstructed pointwise values at $x = x_{i \pm \frac{1}{2}}$ of each polynomial, marked as stars. In ENO perspective, $p_3(x)$ is an appropriate choice, as $S_3 = \{I_i, I_{i+1}, I_{i+2}\}$ does not include the discontinuous point.

as a convex combination with nonlinear weights ω_m :

$$q_{i \pm \frac{1}{2}} = \sum_{m=1}^3 \omega_m p_m(x_{i \pm \frac{1}{2}}). \quad (3.13)$$

The core design principle of WENO is to construct nonlinear weights ω_m that adaptively select smooth stencils and converges into the linear reconstruction scheme when all stencils are smooth. Mathematically speaking, the nonlinear

weights should be converged into the *linear weights* γ_m , $m = 1, 2, 3$,

$$\phi(x) = \sum_{m=1}^3 \gamma_m p_m(x), \quad (3.14)$$

where $\phi(x)$ is the reconstructed polynomial within the whole stencil $S = \bigcup_{m=1}^3 S_m$,

$$\frac{1}{\Delta x} \int_{I_k} \phi(x) dx = \bar{q}_k, \quad I_k \in \bigcup_{m=1}^3 S_m. \quad (3.15)$$

As the $\phi(x)$ is the quartic polynomial, it ensures fifth-order convergence rate of the estimations for pointwise values,

$$q_{i \pm \frac{1}{2}} = \phi(x_{i \pm \frac{1}{2}}) + \mathcal{O}(\Delta x^5). \quad (3.16)$$

Jiang and Shu [41] proposed a functional form of the nonlinear weights by,

$$\omega_m = \frac{\tilde{\omega}_m}{\sum_s \tilde{\omega}_s}, \quad \tilde{\omega}_m = \frac{\gamma_m}{(\epsilon + \beta_m)^p}, \quad (3.17)$$

where ϵ is the small number (e.g., 1.0×10^{-36}) to prevent division by zero, β_m is the smoothness indicator which measures the smoothness of the data in the given stencil S_m . The parameter p is an amplification factor for the difference of scales when a discontinuity is present on one of the candidate stencils.

The remaining step for WENO-JS is to construct the smoothness indicator, which has large values when the stencil data is not smooth and becomes arbitrary small in a smooth stencil; thus, it converges to the linear weight. Jiang and Shu proposed a way to measure the smoothness of the profile based on its second derivatives. In the fifth-order WENO-JS method, the smoothness indicators β_m

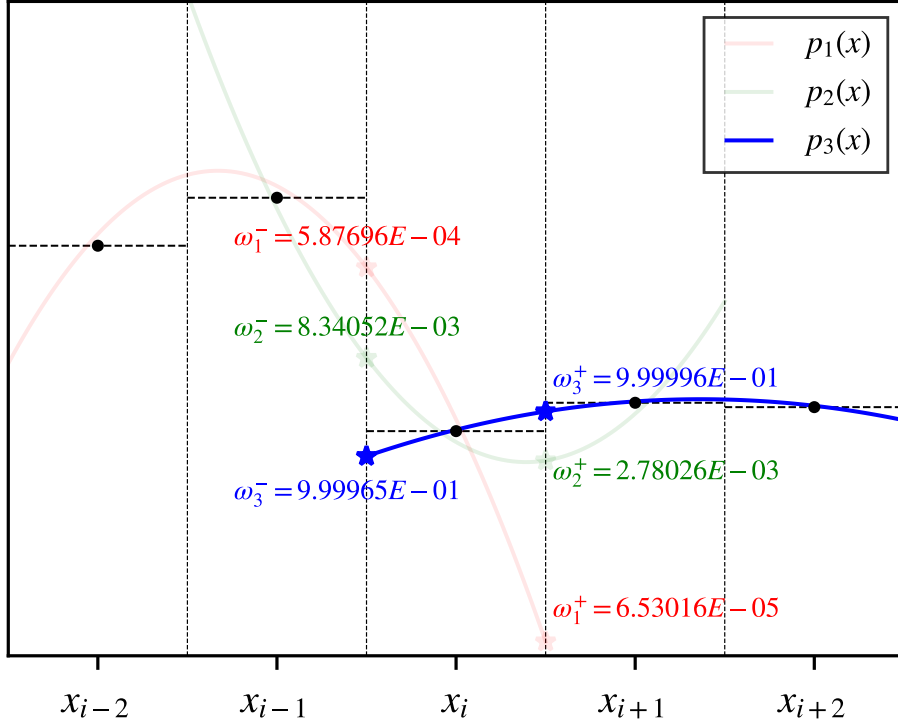


Figure 3.2: The reconstructed fifth-order WENO profiles of the same data stencil in Fig. 3.1, combined with WENO-JS nonlinear weights. (Eq. (3.17)) The opacity of each line measures the nonlinear weights on that sub-stencil, and calculated nonlinear weights are noted in the figure. Note that the nonlinear weights of S_3 are dominant over other stencils, S_1 and S_2 , resulting in ENO-style stencil selection.

are given by,

$$\beta_m = \sum_{n=1}^2 \left(\Delta x^{2n-1} \int_{I_i} \left[\frac{d^n p_m(x)}{dx^n} \right]^2 dx \right). \quad (3.18)$$

Fig. 3.2 shows the effects of the nonlinear weights on the WENO profiles. The nonlinear weights are calculated through Eq. (3.17), with $p = 2$, $\epsilon = 1.0 \times 10^{-36}$. As illustrated in the figure, the nonlinear weights successfully detect the sharp gradient at $x = x_{i-\frac{1}{2}}$ and weighting on $p_3(x)$ dominantly to avoid reconstruction on the discontinuity.

3.1.2 Gaussian Process Reconstruction

Over decades, the high-order data reconstruction/interpolation methods for solving hyperbolic PDEs are based on the polynomial approach. Like the WENO method discussed in the previous section, the idea starts by assuming a unique polynomial represents the stencil data. The polynomial-based approaches are the most successful and popular reconstruction/interpolation methods in the CFD community [83, 20, 41, 47] because of their mathematical simplicity.

However, the polynomial-based reconstruction/interpolation schemes have some downsides. Firstly, since the polynomials are not able to represent the discontinuous data, it is notoriously prone to lead numerical oscillations. There are several ways to avoid the oscillations, like the WENO method in 3.1.1, but it usually brings complexity and computational expenses. Another issue for the polynomial-based approach is that the method must be carried out on a fixed size data stencil, which means changing in stencil size – thus it changes the order of accuracy – requires a complete redesign of the code.

Recently, practitioners have designed *non-polynomial* reconstruction/interpolation methods. Reyes et al. [61, 62] proposed a novel way to use the Gaussian process (GP) to estimate the data at any arbitrary point in high-order accuracy. Based on the stochastic process, GP reconstruction/interpolation methods are able to predict the data on desired points (usually at cell interfaces) without considering any polynomials; therefore, the code is readily extended to a higher order by simply changing the size of the stencil. In the language of GP, this process can be interpreted in the way that a probability distribution for the unknown function values $f(x_*)$ (pointwise values at arbitrary points x_*) can be trained by the known data \bar{q}_i (volume-averaged quantities at cell centers), with posterior mean and uncertainty that are compatible with the known observations.

A GP is fully defined by two functions:

- a mean function $\mu_f(\mathbf{x}) = \mathbb{E}[f(\mathbf{x})]$ over \mathbb{R}^N , and
- a covariance kernel function, which is symmetric and positive-definite integral kernel $K(\mathbf{x}, \mathbf{y}) = \mathbb{E}[(f(\mathbf{x}) - \mu_f(\mathbf{x}))(f(\mathbf{y}) - \mu_f(\mathbf{y}))]$ over $\mathbb{R}^N \times \mathbb{R}^N$,

The function f is then said to belong to the GP with mean and covariance function, written as $f \sim GP(\mu_f(\mathbf{x}), K(\mathbf{x}, \mathbf{y}))$.

Suppose there are N sample points for the function f , namely, $\mathbf{f} = [f(\mathbf{x}_1), \dots, f(\mathbf{x}_N)]$ that are known, the likelihood \mathcal{L} , the probability of \mathbf{f} given the prior GP model, of the input data \mathbf{f} , is given by,

$$\mathcal{L} = P(\mathbf{f}) \equiv (2\pi)^{-\frac{N}{2}} \det |\mathbf{K}|^{-\frac{1}{2}} \exp \left[-\frac{1}{2} (\mathbf{f} - \boldsymbol{\mu}_{\mathbf{f}})^T \mathbf{K} (\mathbf{f} - \boldsymbol{\mu}_{\mathbf{f}}) \right], \quad (3.19)$$

where $\mathbf{K} = [K_{ij}]_{i,j=1,\dots,N}$ with $K_{ij} = K(\mathbf{x}_i, \mathbf{x}_j)$.

The goal of GP is to make a probabilistic statement about the value of $f_* = f(\mathbf{x}_*)$ of unknown function $f \sim GP(\mu_f, K)$ with given function samples. By utilizing the conditioning property of GP from the theory of Bayesian inference, the updated posterior mean function can be obtained as,

$$\tilde{f}_* \equiv \mu_f(\mathbf{x}_*) + \mathbf{k}_*^T \mathbf{K}^{-1} (\mathbf{f} - \boldsymbol{\mu}_{\mathbf{f}}), \quad (3.20)$$

where $\mathbf{k}_* = [k_{*,i}]_{i=1,\dots,N}$ with $k_{*,i} = K(\mathbf{x}_*, \mathbf{x}_i)$. The detailed derivations of Eq. (3.20) can be found in the Appendix of [61]. It is common practice to take the zero mean everywhere, then Eq. (3.20) becomes

$$\tilde{f}_* = \mathbf{k}_*^T \mathbf{K}^{-1} \mathbf{f}, \quad (3.21)$$

reveals GP prediction with known function samples \mathbf{f} , which is the *pointwise*

representation.

However, in the reconstruction scheme, the known function samples should be given as *volume averaged* quantities, not as pointwise values. Therefore, the GP prediction has to be modified to adapt to the data type changes.

Favorably, the volume averaging operator constitutes a linear operation (see Eq. (3.10)). The linear operations on Gaussian random variables result in new Gaussian random variables with linearly transformed mean and covariance; thus, the GP *interpolation* scheme (Eq. (3.21)) can be transformed into the GP *reconstruction* scheme with proper linear functionals that represent volume-averaging.

Consider a measure $dg_k(\mathbf{x})$ on the function $f(\mathbf{x})$ over the cell $I_k = \prod_{d=x,y,z} I_k^{(d)}$ with 1D cells $I_k^{(d)} = [x_k^{(d)} - \frac{\Delta^{(d)}}{2}, x_k^{(d)} + \frac{\Delta^{(d)}}{2}]$, where $d = x, y, z$ represent the direction of the spatial dimension. This defines the linear functionals

$$G_k \equiv \int f(\mathbf{x}) dg_k(\mathbf{x}), \quad (3.22)$$

which represent the volume integral operations on $f(\mathbf{x})$. The measure $dg_k(\mathbf{x})$ are taken to be the cell volume-average measures as,

$$dg_k(\mathbf{x}) = \begin{cases} d^3 \mathbf{x} \cdot \prod_{d=x,y,z} \frac{1}{\Delta^{(d)}} & \text{if } \mathbf{x} \in I_k \\ 0 & \text{otherwise,} \end{cases} \quad (3.23)$$

where $\Delta^{(d)}$ is the grid spacing in the d -direction. Then, the vector $\mathbf{G} [G_1, \dots, G_N]^T$ is normally distributed with mean $\mathbb{E}(\mathbf{G}) = \boldsymbol{\mu}_{\mathbf{G}} = [\mu_{G_1}, \dots, \mu_{G_N}]^T$ and covariance matrix $\mathbf{C} = [C_{kh}]_{k,h=1,\dots,N}$, where

$$\mu_{G_k} = \mathbb{E}[G_k] = \int \mathbb{E}[f(\mathbf{x})] dg_k(\mathbf{x}) = \int \mu_f(\mathbf{x}) dg_k(\mathbf{x}), \quad (3.24)$$

and

$$\begin{aligned}
C_{kh} &= \mathbb{E} [(G_k - \mu_{G_k})(G_h - \mu_{G_h})] \\
&= \int \int \mathbb{E} [(f(\mathbf{x}) - \mu_f(\mathbf{x}))(f(\mathbf{y}) - \mu_f(\mathbf{y}))] dg_k(\mathbf{x}) dg_h(\mathbf{y}) \\
&= \int \int K(\mathbf{x}, \mathbf{y}) dg_k(\mathbf{x}) dg_h(\mathbf{y}).
\end{aligned} \tag{3.25}$$

Thus, the GP distribution on the function $f \sim GP(\mu, K)$ conducts a multivariate Gaussian distribution on N -dimensional vector \mathbf{G} of linear functionals of f .

In order to generalize Eq. (3.21) for reconstruction, the remaining task is to define the prediction vector $\mathbf{T}_* = [\mathbf{T}_{*,k}]_{k=1,\dots,N}$ at any arbitrary point of interest \mathbf{x}_* as,

$$\begin{aligned}
T_{*,k} &= \mathbb{E} [(f(\mathbf{x}_*) - \mu_f(\mathbf{x}_*))(G_k - \mu_{G_k})] \\
&= \int K(\mathbf{x}_*, \mathbf{x}) dg_k(\mathbf{x}).
\end{aligned} \tag{3.26}$$

Finally, the pointwise estimation of $f(\mathbf{x}_*)$ at the point of \mathbf{x}_* , reconstructed from the volume-averaged data \mathbf{G} is given by,

$$\tilde{f}_* = \mathbf{T}_*^T \mathbf{C}^{-1} \mathbf{G}, \tag{3.27}$$

with zero mean values. Eq. (3.27) shows the explicit form of GP reconstruction with known volume-averaged data points, \mathbf{G} . The terms \mathbf{C} and \mathbf{T} are determined by the choice of the covariance kernel function, $K(\mathbf{x}, \mathbf{y})$, which measures the relationship between pairs of data. In this dissertation, the “Squared Exponential” (SE) kernel used for GP reconstruction.

$$K_{\text{SE}}(\mathbf{x}, \mathbf{y}) = \Sigma^2 \exp \left[-\frac{(\mathbf{x} - \mathbf{y})^2}{2\ell^2} \right]. \tag{3.28}$$

The SE kernel has two hyperparameters Σ and ℓ , but the hyperparameter Σ has no effect on the posterior mean function, so this dissertation set $\Sigma = 1$ for simplicity. On the other hand, the hyperparameter ℓ expresses the correlation length scale of the model, so it should be chosen meticulously corresponding to the physical length scale of the grid configuration.

For 1D reconstructions, $T_{*,k}$ and C_{kh} for SE kernel becomes,

$$T_{*,k} = \sqrt{\frac{\pi}{2}} \frac{\ell}{\Delta} \left\{ \operatorname{erf} \left[\frac{\Delta_{k*} + 1/2}{\sqrt{2}\ell/\Delta} \right] - \operatorname{erf} \left[\frac{\Delta_{k*} - 1/2}{\sqrt{2}\ell/\Delta} \right] \right\}, \quad (3.29)$$

and

$$\begin{aligned} C_{kh} = & \sqrt{\pi} \left(\frac{\ell}{\Delta} \right)^2 \left\{ \left(\frac{\Delta_{kh} + 1}{\sqrt{2}\ell/\Delta} \operatorname{erf} \left[\frac{\Delta_{kh} + 1}{\sqrt{2}\ell/\Delta} \right] + \frac{\Delta_{kh} - 1}{\sqrt{2}\ell/\Delta} \operatorname{erf} \left[\frac{\Delta_{kh} - 1}{\sqrt{2}\ell/\Delta} \right] \right) \right. \\ & + \frac{1}{\sqrt{\pi}} \left(\exp \left[-\frac{(\Delta_{kh} + 1)^2}{2(\ell/\Delta)^2} \right] + \exp \left[-\frac{(\Delta_{kh} - 1)^2}{2(\ell/\Delta)^2} \right] \right) \\ & \left. - 2 \left(\frac{\Delta_{kh}}{\sqrt{2}\ell/\Delta} \operatorname{erf} \left[\frac{\Delta_{kh}}{\sqrt{2}\ell/\Delta} \right] + \frac{1}{\sqrt{\pi}} \exp \left[-\frac{\Delta_{kh}^2}{2(\ell/\Delta)^2} \right] \right) \right\}, \end{aligned} \quad (3.30)$$

where $\Delta_{kh} = (x_k - x_h)/\Delta$ and Δ is the grid spacing along the 1D direction. Note that the analytic derivations of $T_{*,k}$ and C_{kh} above only depend on the grid spacing and the length between the prediction point \mathbf{x}_* and the locations of known training data. With uniform grid configuration, those values are established at the initial step. Since the prediction points are the cell interfaces $x_{i \pm \frac{1}{2}}$ for the conventional FDM constructions, one can save,

$$\mathbf{z}_{i \pm \frac{1}{2}} := \mathbf{T}_{i \pm \frac{1}{2}}^T \mathbf{C}^{-1}, \quad (3.31)$$

as the weighting factor for the reconstruction can be expressed as,

$$q_{i \pm \frac{1}{2}} = \mathbf{z}_{i \pm \frac{1}{2}}^T \mathbf{G}, \quad (3.32)$$

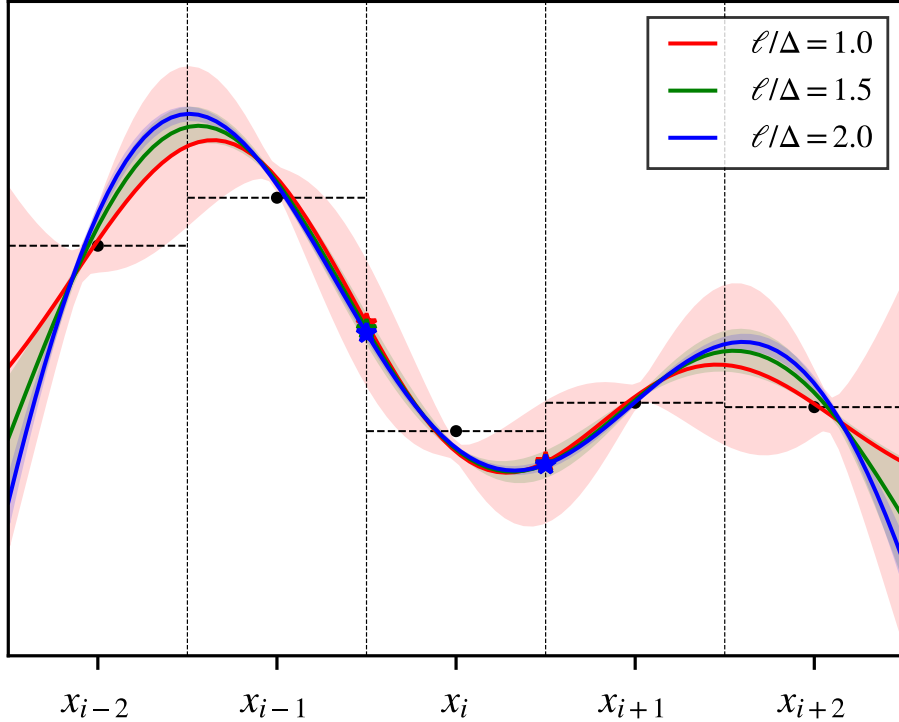


Figure 3.3: GP reconstructed profiles with the same data as Figs. 3.1 and 3.2 with different hyperparameters $\ell = 1.0, 1.5, 3.0$. Note that all the reconstructed profiles produce a new local minimum near $x = x_{i+\frac{1}{2}}$, which violates the monotonic-preserving condition and leads to numerical oscillations. The shaded areas represent 95% confidence regions from the posterior variance.

for computational efficiency.

However, the GP reconstruction also needs special handling for the discontinuous profiles, like the nonlinear weightings in the WENO method in Section 3.1.1. Fig. 3.3 shows the GP reconstructions with the same data as Figs. 3.1 and 3.2, with $\ell = 1, 1.5, 3$. The initial profile has a strong gradient at $x = x_{i-\frac{1}{2}}$; hence, the GP reconstructed profiles have undershot values at $x = x_{i+\frac{1}{2}}$.

Reyes et al. [62] proposed a WENO-like approach to the GP reconstruction/interpolations by considering the GP marginal likelihood of the local stencil data for measuring the smoothness of the stencil, and use them to construct nonlinear weights as like in the standard WENO method.

For five points, fifth-order GP reconstruction, suppose three sub-stencils as like fifth-order WENO method. (Eq. (3.11)) Then there are three reconstructed pointwise values for each of the candidate stencils S_m ,

$$q_{i \pm \frac{1}{2}, m} = \mathbf{z}_{i \pm \frac{1}{2}, m}^T \mathbf{G}_m. \quad (3.33)$$

The final reconstructed value is taken as the combinations of three candidate GP approximations with nonlinear weights,

$$q_{i \pm \frac{1}{2}} = \sum_{m=1}^3 \omega_m q_{i \pm \frac{1}{2}, m}. \quad (3.34)$$

As in the conventional WENO method, the nonlinear weights ω_m must be reduced to the optimal (linear) weights γ_m in a smooth region, so the weighted combination Eq. (3.34) converges to the GP approximation over the whole stencil $S = \bigcup_m S_m$. The optimal weights γ_m must satisfy,

$$\mathbf{z}_{i \pm \frac{1}{2}}^T \mathbf{G} = q_{i \pm \frac{1}{2}} = \sum_{m=1}^3 \gamma_m q_{i \pm \frac{1}{2}, m} = \sum_{m=1}^3 \gamma_m \mathbf{z}_{i \pm \frac{1}{2}, m}^T \mathbf{G}_m, \quad (3.35)$$

or explicitly,

$$\gamma_1 \left[\begin{array}{c} z_{1,1}^\pm \\ z_{2,1}^\pm \\ z_{3,1}^\pm \\ 0 \\ 0 \end{array} \right] + \gamma_2 \left[\begin{array}{c} 0 \\ z_{1,2}^\pm \\ z_{2,2}^\pm \\ z_{3,2}^\pm \\ 0 \end{array} \right] + \gamma_3 \left[\begin{array}{c} 0 \\ 0 \\ z_{1,3}^\pm \\ z_{2,3}^\pm \\ z_{3,3}^\pm \end{array} \right] = \left[\begin{array}{c} z_1^\pm \\ z_2^\pm \\ z_3^\pm \\ z_4^\pm \\ z_5^\pm \end{array} \right]. \quad (3.36)$$

The Eq. (3.36) can be rewritten in the matrix form of overdetermined system as,

$$\begin{bmatrix} z_{1,1}^\pm & 0 & 0 \\ z_{2,1}^\pm & z_{1,2}^\pm & 0 \\ z_{3,1}^\pm & z_{2,2}^\pm & z_{1,3}^\pm \\ 0 & z_{3,2}^\pm & z_{2,3}^\pm \\ 0 & 0 & z_{3,3}^\pm \end{bmatrix} \begin{bmatrix} \gamma_1 \\ \gamma_2 \\ \gamma_3 \end{bmatrix} = \begin{bmatrix} z_1^\pm \\ z_2^\pm \\ z_3^\pm \\ z_4^\pm \\ z_5^\pm \end{bmatrix}. \quad (3.37)$$

Thus, the optimal weights $\gamma_m, m = 1, 2, 3$ are obtained by solving the overdetermined system, Eq. (3.37). It should be noted that the optimal weights are entirely determined by the choice of kernel function and the stencil size, so they are computed and stored before the simulation begins.

For constructing WENO nonlinear weights Eq. (3.17), the only remaining task is to determine the smoothness indicator, β_m , which measures the degree of smoothness of a given stencil of data. Unlike the conventional WENO method, which measures the smoothness of the data by calculating L_2 norms of all the derivatives of the reconstructed polynomials, the GP reconstruction method should take a different approach to specify the smoothness indicator because there is no polynomial defined in GP. One successful practice is to use the marginal likelihood of the data. The likelihood function is well-furnished to gauge the deviations from smoothness given a sufficiently smooth covariance kernel function, SE kernel, for example. Thus, the GP predictions have smaller likelihoods to non-smooth function by its design.

Suppose the negative log of the GP marginal likelihood as

$$-\log \mathcal{L} = \frac{N}{2} \log [2\pi] + \frac{1}{2} \log |\det \mathbf{K}_m| + \frac{1}{2} (\mathbf{f}_m - \boldsymbol{\mu}_f)^T \mathbf{K}_m^{-1} (\mathbf{f}_m - \boldsymbol{\mu}_f), \quad (3.38)$$

then the three terms on the right-hand side of Eq. (3.38) are revealed as a normal-

ization, a complexity penalty, and a data fit term, respectively. The normalization term and the complexity penalty have no effects on defining smoothness indicators in a uniform grid configuration; only the data fit term along with the choice of zero mean is used for constructing smoothness indicators in GP,

$$\beta_m = \mathbf{f}_m^T (\mathbf{K}_m^{-1}) \mathbf{f}_m. \quad (3.39)$$

To handle discontinuity, a second hyperparameter, σ , should be used in Eq. (3.39), to discriminate discontinuities from smooth regions. σ should be on the order of the grid spacing.

Like GP reconstruction weights Eq. (3.32), the calculations of GP smoothness indicators β_m can be expressed in a more computationally efficient form. Considering the eigensystem $\mathbf{K}_m^{-1} = \sum_i \mathbf{v}_i^m (\mathbf{v}_i^m)^T / \lambda_i^m$,

$$\beta_m = \sum_{i=1}^3 \mathbf{f}_m^T \left(\frac{\mathbf{v}_i^m (\mathbf{v}_i^m)^T}{\lambda_i} \right) \mathbf{f}_m, \quad (3.40)$$

in the five-point, three-stencil GP-WENO method. Again, the observed (training) data is in the volume-averaged form; thus, the data-type conversion should be examined:

$$\mathbf{f}_m = \mathbf{Z}_m^T \mathbf{G}_m, \quad (3.41)$$

where each column vector of \mathbf{Z}_m is given by the GP reconstructing weight, \mathbf{z} , (see Eq. (3.31)) for each elements of \mathbf{f}_m .

Lastly, the calculation of the smoothness indicator beta can be expressed in

the compact form as,

$$\begin{aligned}\beta_m &= \sum_{i=1}^3 \left(\frac{(\mathbf{v}_i^m)^T \mathbf{Z}_m^T \mathbf{G}_m}{\sqrt{\lambda_i^m}} \right)^2 \\ &= \sum_{i=1}^3 (\mathbf{P}_i^m \mathbf{G}_m)^2,\end{aligned}\tag{3.42}$$

where $\mathbf{P}_i^m := \frac{(\mathbf{v}_i^m)^T \mathbf{Z}_m^T}{\sqrt{\lambda_i^m}}$, which can be established before the simulation start, in uniform grid configuration.

Now, the nonlinear weights for GP-WENO reconstruction are fully determined with Eq. (3.17). In the stepwise representation, the GP-WENO reconstruction scheme for FDM formulation in the uniform grid can be summarized as below:

1. Before the simulation starts, calculate the following values and store them for later reconstructions:
 - (a) Reconstruction weights, \mathbf{z}_m (Eq. (3.33)) for each candidate stencil, m .
 - (b) Linear weights, γ_m , by solving overdetermined system, Eq. (3.37), using the least square method.
 - (c) \mathbf{P}_i^m (Eq. (3.42)) for calculating smoothness indicator β_m in later.
2. During the simulation, at each reconstruction step of cell I_i :
 - (a) Calculate nonlinear weights, ω_m , following the conventional WENO method. (Eq. (3.17))
 - (b) Compute m -number of reconstructed candidate data, $q_{i \pm \frac{1}{2}, m}$. (Eq. (3.33))
 - (c) Taking weighted combinations of $q_{i \pm \frac{1}{2}, m}$, with nonlinear weights, ω_m , and finalize the reconstruction step at $x_i = x_{i \pm \frac{1}{2}}$. (Eq. (3.34))

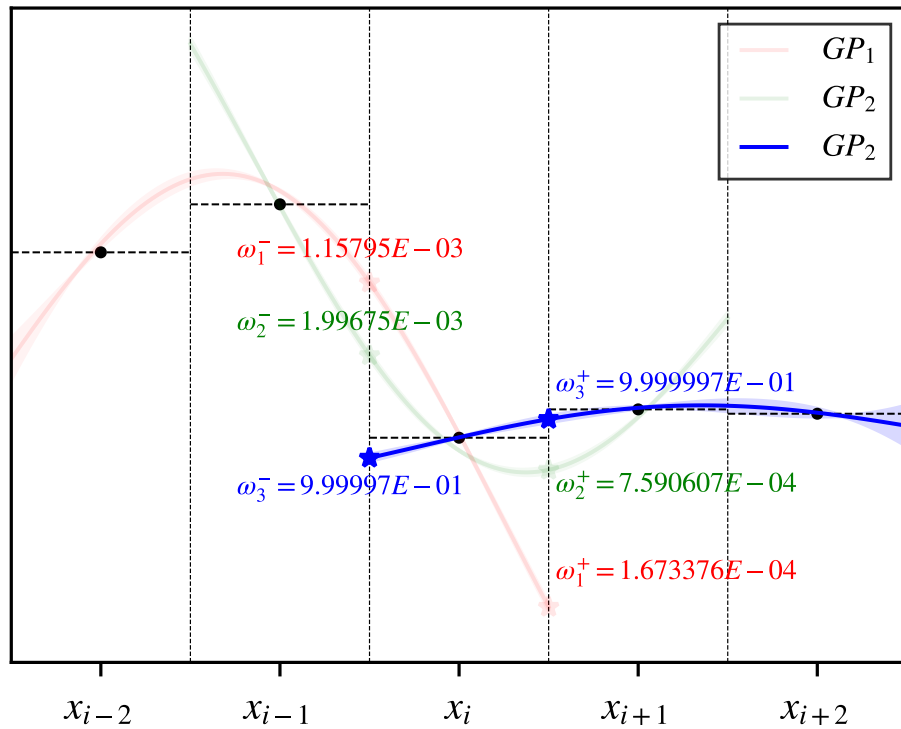


Figure 3.4: GP-WENO Reconstructed profiles with nonlinear weights with the same data as Fig. 3.3. Hyperparameters $\ell = 2\Delta$ and $\sigma = 2\Delta$ are used. 95% confidence regions are shaded with the corresponding colors, and the opacity of each prediction measures the nonlinear weights on that sub-stencil.

3.2 High-Order Time Integration Schemes

A high-order temporal discretization scheme ought to be considered alongside the high-order spatial data interpolation/reconstruction to acquire highly accurate numerical solutions in FDM formulation. The numerical errors arise from both spatial and temporal discretizations since the solution of the conservative PDEs lies on the spatio-temporal plane. The overall order of solution accuracy will be determined by the highest order term of the truncation errors both from the spatial and temporal discretization, i.e., $\mathcal{O}(\Delta s^p, \Delta t^q)$. For example, if the leading error term from the temporal discretization is significantly larger than the leading error term from the spatial discretizations, $\mathcal{O}(\Delta t^q) > \mathcal{O}(\Delta s^p)$, then the solution accuracy will be degraded by order of temporal accuracy, q , no matter the order of spatial accuracy is used. Therefore, a high-order FDM scheme requires a meticulously designed temporal discretization method that ensures the solution's accuracy and stability.

3.2.1 Strong Stability Preserving Runge-Kutta Methods

The Runge-Kutta (RK) method is the most popular way to integrate the semi-discretized form of FDM (Eq. (2.11)) over the time axis. The key idea is to treat the Eq. (2.11) as an ordinary differential equation (ODE) at each lattice point on the computational mesh as,

$$\partial_t \mathbf{U}_i = \mathcal{L}_i(\mathbf{U}), \quad (3.43)$$

where the right-hand side operator \mathcal{L}_i is given by the spatial discretization method at cell I_i . The RK approach can be viewed as a strategy to integrate PDEs by solving several ODE problems at each discretized time domain. In general, m -stage RK method which integrate Eq. (3.43) from $t = t^n$ to $t = t^n + \Delta t = t^{n+1}$ is

given by,

$$\begin{aligned}\mathbf{U}^{(0)} &= \mathbf{U}^n, \\ \mathbf{U}^{(l)} &= \sum_{k=0}^{l-1} \left(\alpha_{l,k} \mathbf{U}^{(k)} + \Delta t \beta_{l,k} \mathcal{L}(\mathbf{U}^{(k)}) \right), \quad \alpha_{l,k} \geq 0, \quad l = 1, \dots, m \\ \mathbf{U}^{n+1} &= \mathbf{U}^{(m)},\end{aligned}\tag{3.44}$$

where the spatial discretization index, i , is omitted for simplicity. Therefore, the coefficients $\alpha_{l,k}$ and $\beta_{l,k}$ fully determine the numerical accuracy and stability of the RK scheme.

Like the spatial discretization method, it is crucial to consider the TVD property of the temporal discretization scheme. Gottlieb and her collaborators [35, 36, 34] developed the so-called strong stability preserving Runge-Kutta (SSP-RK) method, which ensures TVD property by sequentially applying convex combinations of the first-order forward Euler method as a building-block at each sub-stage. In this way, the desired TVD property is achieved if each of the sub-stage is TVD.

SSP-RK method uses that the forward Euler method for building each sub-stages. Since the forward Euler method is strongly stable under the Courant–Friedrichs–Lewy (CFL) condition; thus, if all sub-stages of the RK method can be described as a form of the forward Euler method, then the TVD property is fulfilled by virtue of the forward Euler method. It is easy to see in Eq. (3.44) that the sub-stages of the RK method, $\mathbf{U}^{(l)}$ can be described as the forward Euler method if all the $\beta_{l,k}$ are nonnegative $\beta_{l,k} \geq 0$ by replacing Δt by $\frac{\beta_{l,k}}{\alpha_{l,k}} \Delta t$. For example, in [35], Gottlieb

found the optimal third-order SSP-RK method given by,

$$\begin{aligned}\mathbf{U}^{(1)} &= \mathbf{U}^n + \Delta t \mathcal{L}(\mathbf{U}^n), \\ \mathbf{U}^{(2)} &= \frac{3}{4} \mathbf{U}^n + \frac{1}{4} \mathbf{U}^{(1)} + \frac{1}{4} \Delta t \mathcal{L}(\mathbf{U}^{(1)}), \\ \mathbf{U}^{n+1} &= \frac{1}{3} \mathbf{U}^n + \frac{2}{3} \mathbf{U}^{(2)} + \frac{2}{3} \Delta t \mathcal{L}(\mathbf{U}^{(2)}),\end{aligned}\tag{3.45}$$

which requires three sub-stages for integrating from $t = t^n$ to $t = t^{n+1}$.

The above third-order, three-stages SSP-RK method Eq. (3.45) is by far the most famous high-order time integrator used in most high-order method researches in the CFD community. In practice, spatial accuracy is often considered to carry more weight than temporal accuracy in designing higher accurate spatial models [10, 54], so combining the high-order spatial method (generally, fifth-order or higher) with a relatively low-order temporal scheme (third-order SSP-RK) could be justifiable. However, as it is shown in [49], the order of convergence rate of the solution can be degraded by the order of temporal method (e.g., third-order) in high-resolution computational grids, so using a higher than third-order temporal scheme is required for maintaining desired spatial accuracy in a high-resolution grid.

In contrast to the third-order SSP-RK3 method, devising a fourth-order SSP-RK4 is more involved to meet the favorable SSP property, which is ensured by positive coefficients. Several theoretical studies have shown that a fourth-order SSP-RK4 cannot be formulated with just four sub-stages and positive coefficients [35], meaning that the classical four-stage, fourth-order RK is not SSP. For example,

by far the most optimal fourth-order, fourth-stage SSP-RK method is:

$$\begin{aligned}
\mathbf{U}^{(1)} &= \mathbf{U}^n + \frac{1}{2}\Delta t \mathcal{L}(\mathbf{U}^n), \\
\mathbf{U}^{(2)} &= \frac{649}{1600}\mathbf{U}^{(0)} - \frac{10890423}{25193600}\Delta t \tilde{\mathcal{L}}(\mathbf{U}^n) + \frac{951}{1600}\mathbf{U}^{(1)} + \frac{5000}{7873}\Delta t \mathcal{L}(\mathbf{U}^{(1)}), \\
\mathbf{U}^{(3)} &= \frac{53989}{2500000}\mathbf{U}^n - \frac{102261}{5000000}\Delta t \tilde{\mathcal{L}}(\mathbf{U}^n) + \frac{4806213}{20000000}\mathbf{U}^{(1)} \\
&\quad - \frac{5121}{20000}\Delta t \tilde{\mathcal{L}}(\mathbf{U}^{(1)}) + \frac{23619}{32000}\mathbf{U}^{(2)} + \frac{7873}{10000}\Delta t \mathcal{L}(\mathbf{U}^{(2)}), \\
\mathbf{U}^{(4)} &= \frac{1}{5}\mathbf{U}^n + \frac{1}{10}\Delta t \mathcal{L}(\mathbf{U}^n) + \frac{6127}{30000}\mathbf{U}^{(1)} + \frac{1}{6}\Delta t \mathcal{L}(\mathbf{U}^{(1)}) + \frac{7873}{30000}\mathbf{U}^{(2)} \\
&\quad + \frac{1}{3}\mathbf{U}^{(3)} + \frac{1}{6}\Delta t \mathcal{L}(\mathbf{U}^{(3)}).
\end{aligned} \tag{3.46}$$

Note that the above four-stage, fourth-order SSP-RK method uses the adjoint spatial operator, $\tilde{\mathcal{L}}$, to bear the negative coefficients, e.g., $-\frac{10890423}{25193600}$ and $-\frac{102261}{5000000}$. Numerically speaking, the only difference between \mathcal{L} and $\tilde{\mathcal{L}}$ is the direction of the upwind limiting. Although the computational cost of calculating $\mathcal{L}(\mathbf{U})$ and $\tilde{\mathcal{L}}(\mathbf{U})$ are identical, but it demands separated codes, and leads implementation complexity.

Spiteri and Ruuth [73] proposed a five-stage, fourth-order SSP-RK4 method that does not require to use adjoint operator:

$$\begin{aligned}
\mathbf{U}^{(1)} &= \mathbf{U}^n + 0.391752226571890\Delta t \mathcal{L}(\mathbf{U}^n), \\
\mathbf{U}^{(2)} &= 0.444370493651235\mathbf{U}^n + 0.555629506348765\mathbf{U}^{(1)} + 0.368410593050371\Delta t \mathcal{L}(\mathbf{U}^{(1)}), \\
\mathbf{U}^{(3)} &= 0.620101851488403\mathbf{U}^n + 0.379898148511597\mathbf{U}^{(2)} + 0.251891774271694\Delta t \mathcal{L}(\mathbf{U}^{(2)}), \\
\mathbf{U}^{(4)} &= 0.178079954393132\mathbf{U}^n + 0.821920045606868\mathbf{U}^{(3)} + 0.544974750228521\Delta t \mathcal{L}(\mathbf{U}^{(3)}), \\
\mathbf{U}^{n+1} &= 0.517231671970585\mathbf{U}^{(2)} + 0.096059710526147\mathbf{U}^{(3)} + 0.063692468666290\Delta t \mathcal{L}(\mathbf{U}^{(3)}) \\
&\quad + 0.386708617503268\mathbf{U}^{(4)} + 0.226007483236906\Delta t \mathcal{L}(\mathbf{U}^{(4)}).
\end{aligned} \tag{3.47}$$

In this dissertation, the fourth-order SSP-RK4 method refers the Spiteri and Ruuth method, Eq. (3.47).

In many studies about high-order CFD solvers [35, 36, 34, 54, 22, 23, 61, 62], the SSP-RK schemes have proven high fidelity and portability, guaranteeing high-order accuracy and numerical stability with TVD property. However, the very nature of the SSP-RK method – being a multi-stage approach – increases computational costs in CFD simulations. In SSP-RK methods, the data reconstruction/interpolation (i.e., $\mathcal{L}(\cdot)$) and the boundary condition should be applied in each sub-stage, which increases the computational resources and the footprint of data communications in the parallel computational architecture. It makes the simulations using the adaptive mesh refinement (AMR) method less attractive, which progressively refines the grid resolutions and increases data communications around the simulations' interesting features.

3.2.2 Lax–Wendroff Type Methods

The Lax-Wendroff method [46] rely on the Taylor expansion in time to achieve high-order in time accuracy:

$$\mathbf{U}^{n+1} = \mathbf{U}^n + \Delta t \partial_t \mathbf{U}|^n + \frac{\Delta t^2}{2!} \partial_t^2 \mathbf{U}|^n + \mathcal{O}(\Delta t^3). \quad (3.48)$$

The temporal derivatives can be transformed into spatial derivatives by applying the Lax-Wendroff or Cauchy-Kowalewski procedure (LW/CK hereafter). In one-

dimensional conservative PDEs, for example,

$$\begin{aligned}
\partial_t \mathbf{U} &= -\partial_x \mathbf{F}, \\
\partial_t^2 \mathbf{U} &= \partial_t (-\partial_x \mathbf{F}) \\
&= -\partial_x (\partial_{\mathbf{U}} \mathbf{F} \cdot \partial_t \mathbf{U}) \\
&= \partial_x (\partial_{\mathbf{U}} \mathbf{F} \cdot \partial_x \mathbf{F}),
\end{aligned} \tag{3.49}$$

where $\partial_{\mathbf{U}} \mathbf{F}$ is a flux Jacobian matrix. In the original Lax-Wendroff method [46] used an approximation of $\partial_x (\partial_{\mathbf{U}} \mathbf{F} \cdot \partial_x \mathbf{F}) \approx \frac{1}{\Delta x} (\partial_{\mathbf{U}} \mathbf{F}|_{i+\frac{1}{2}} \cdot \partial_x \mathbf{F} - \partial_{\mathbf{U}} \mathbf{F}|_{i-\frac{1}{2}} \cdot \partial_x \mathbf{F})$, but it is possible to get an explicit form as,

$$\partial_t^2 \mathbf{U} = \partial_x (\partial_{\mathbf{U}} \mathbf{F} \cdot \partial_x \mathbf{F}) = \partial_{\mathbf{U}}^2 \mathbf{F} \cdot \partial_x \mathbf{F} + \partial_{\mathbf{U}} \mathbf{F} \cdot \partial_x^2 \mathbf{F}, \tag{3.50}$$

with flux Hessian tensor, $\partial_{\mathbf{U}}^2 \mathbf{F}$.

The primary advantage of the Lax-Wendroff method is that it can achieve a high order in time accuracy within a single step of the calculation. The idea to construct the time-Taylor series by harnessing the tight coupling of temporal and spatial derivatives through LW/CK procedures inspires many practitioners to develop single-step, high-order methods based on the Lax-Wendroff method.

In 2001, Toro et al. [80] extended this idea by combining it with the generalized Riemann problems (GRPs) and introduced the Arbitrary high order derivative Riemann problem (ADER) method. Toro and his collaborators constructed Riemann problems for each spatial derivative at cell interface, $x_{i+\frac{1}{2}}$:

$$\begin{aligned}
\partial_t \mathbf{U}_x^{(k)} + \partial_{\mathbf{U}} \mathbf{F}|_{i+\frac{1}{2}} \partial_x \mathbf{U}_x^{(k)} &= 0, \quad \text{where } \partial_{\mathbf{U}} \mathbf{F}|_{i+\frac{1}{2}} = \partial_{\mathbf{U}} \mathbf{F}(\mathbf{U}_{i+\frac{1}{2}}, 0^+), \\
\mathbf{U}_x^{(k)}(x, 0) &= \begin{cases} \frac{\partial^k}{\partial x^k} \mathbf{U}_{i+\frac{1}{2},L}, & x < x_{i+\frac{1}{2}}, \\ \frac{\partial^k}{\partial x^k} \mathbf{U}_{i+\frac{1}{2},R}, & x > x_{i+\frac{1}{2}}, \end{cases}
\end{aligned} \tag{3.51}$$

where $\mathbf{U}_x^{(k)} = \frac{\partial^k \mathbf{U}}{\partial x^k}$, and $\mathbf{U}_{i+\frac{1}{2},LR}$ represent left and right Riemann states at cell interface, $x_{i+\frac{1}{2}}$. Reconstructed profiles can find the Riemann states of the spatial derivatives. The resulting solutions of the above Riemann problems are then applied for LW/CK procedures to get the temporal derivatives, $\frac{\partial^k \mathbf{U}}{\partial t^k} \Big|_{i+\frac{1}{2}}$, and they are used to construct the time-Taylor series of the conservative variables at cell interfaces:

$$\mathbf{U}(x_{i+\frac{1}{2}}, \tau) = \mathbf{U}(x_{i+\frac{1}{2}}, 0^+) + \sum_{k=1}^{r-1} \left[\frac{\partial^k}{\partial t^k} \mathbf{U}(x, t)(x_{i+\frac{1}{2}}, 0^+) \right] \frac{\tau^k}{k!}. \quad (3.52)$$

ADER methods were further developed in [80, 76, 78], and it has grown its popularity over decades, leading to various further modifications. ADER-DG [29, 85] and ADER-CG [9, 8, 6] in the context of discontinuous and continuous Galerkin schemes; other efforts of employing an implicit GRP solver to solve scalar equations with stiff source terms [55], its extensions to second-order schemes for nonlinear systems [57] and to general hyperbolic systems [81]. The use of an implicit time Taylor series expansion for GRP was further simplified in the study by Montecinos and Balsara [56]. Along the line of simplifying the standard ADER approach, the Differential Transform Method (DTM) [17] was also adopted to alleviate the cost of the ADER scheme, coined as ADER-DT (or ADER-Taylor) in [60, 58, 59].

In general, Lax-Wendroff type methods are able to update the solution in single-step with high-order temporal accuracy. The fundamental advantage of being a single-stage method is the enhanced performance. This becomes hugely attractive in massively parallel computing, minimizing the computational frequency of data transfers between processors each time step, which would need to be repeated for each intermediate RK stage. On the other hand, the dependence of the strong coupling on analytic derivatives of the governing PDEs makes the LW/CK approach less flexible and less broadly applicable to all systems of PDEs.

Chapter 4

System-Free Picard Integral Formulation

Unlike the broad usage of SSP-RK in various discrete PDE solvers, the developments of ADER mentioned above have been exclusively applied to FV and DG methods, but FD methods. This is mainly because the fundamental principle of obtaining high-order accuracy in the original ADER scheme relies on solving generalized (or high-order) Riemann problems, which are the characteristic building blocks of FV and DG methods.

Recently, Christlieb et al. introduced a new high-order temporal scheme for FDM, the so-called Picard integral formulation (PIF) method. [19, 65] The PIF discretization is based on the constructions of high-order approximation to the time-averaged fluxes over $[t^n, t^{n+1}]$, allowing high-order temporal accuracy in a single-step update. Firstly introduced in [19], the PIF method demonstrated third-order temporally accurate numerical fluxes by computing the coefficients of the time-Taylor expansion of the averaged fluxes via LW/CK procedure which converts the high-order temporal derivatives terms into the spatial derivatives.

However, like many Lax-Wendroff type methods, the PIF method requires

finding analytic derivations for flux Jacobians and Hessians. Although the Jacobian and the Hessian calculations can be easily obtained with the aid of symbolic manipulators such as **Sympy**, **Mathematica**, or **Maple**, it still demands complicated coding/debugging efforts and ample memory consumption. Furthermore, as the Jacobian/Hessian calculations highly depend on the type of the governing system under consideration, it is required to re-derive the Jacobian/Hessian terms analytically every time we need to solve a new system, e.g., shallow water equations or magnetohydrodynamics (MHD) equations, to name a few. In addition, the calculation complexities of the Jacobian-like terms are drastically increasing with the number of spatial dimensions and the order of accuracy.

4.1 Picard Integral Formulation

Applying the Picard integral formulation (PIF), the governing equations Eq. (2.1) can be discretized by taking a time average within a single time step Δt over an interval $[t^n, t^{n+1}]$,

$$\mathbf{U}^{n+1} = \mathbf{U}^n - \Delta t (\partial_x \mathbf{F}^{avg} + \partial_y \mathbf{G}^{avg} + \partial_z \mathbf{H}^{avg}), \quad (4.1)$$

where \mathbf{F}^{avg} , \mathbf{G}^{avg} , and \mathbf{H}^{avg} are the time-averaged fluxes in each direction,

$$\begin{aligned} \mathbf{F}^{avg}(\mathbf{x}) &= \frac{1}{\Delta t} \int_{t^n}^{t^{n+1}} \mathbf{F}(\mathbf{U}(\mathbf{x}, t)) dt, \\ \mathbf{G}^{avg}(\mathbf{x}) &= \frac{1}{\Delta t} \int_{t^n}^{t^{n+1}} \mathbf{G}(\mathbf{U}(\mathbf{x}, t)) dt, \\ \mathbf{H}^{avg}(\mathbf{x}) &= \frac{1}{\Delta t} \int_{t^n}^{t^{n+1}} \mathbf{H}(\mathbf{U}(\mathbf{x}, t)) dt, \end{aligned} \quad (4.2)$$

for $\mathbf{x} = (x, y, z) \in \mathbb{R}^3$.

The goal is to express the spatial derivatives of the time-averaged fluxes

in Eq. (4.1) using highly approximated numerical fluxes $\hat{\mathbf{f}}$, $\hat{\mathbf{g}}$, and $\hat{\mathbf{h}}$ at cell interfaces:

$$\begin{aligned}\partial_x \mathbf{F}^{avg}|_{\mathbf{x}=\mathbf{x}_{ijk}} &= \frac{1}{\Delta x} (\hat{\mathbf{f}}_{i+\frac{1}{2},j,k} - \hat{\mathbf{f}}_{i-\frac{1}{2},j,k}) + \mathcal{O}(\Delta x^p + \Delta t^q), \\ \partial_y \mathbf{G}^{avg}|_{\mathbf{x}=\mathbf{x}_{ijk}} &= \frac{1}{\Delta y} (\hat{\mathbf{g}}_{i,j+\frac{1}{2},k} - \hat{\mathbf{g}}_{i,j-\frac{1}{2},k}) + \mathcal{O}(\Delta y^p + \Delta t^q), \\ \partial_z \mathbf{H}^{avg}|_{\mathbf{x}=\mathbf{x}_{ijk}} &= \frac{1}{\Delta z} (\hat{\mathbf{h}}_{i,j,k+\frac{1}{2}} - \hat{\mathbf{h}}_{i,j,k-\frac{1}{2}}) + \mathcal{O}(\Delta z^p + \Delta t^q),\end{aligned}\quad (4.3)$$

where $\mathbf{x}_{ijk} = (x_i, y_j, z_k)$ is the discretization indices.

The above equation is almost analog to Eq. (2.12), which is the conventional way to construct numerical fluxes for FDM through the high-order reconstruction schemes (Eq. (2.16)). The only difference is to take time-averaged fluxes, \mathbf{F}^{avg} , \mathbf{G}^{avg} , and \mathbf{H}^{avg} as an input of the reconstruction scheme rather than taking pointwise fluxes. Thus Eq. (4.3) states that with highly approximated time-averaged fluxes, the resulting numerical fluxes from the conventional reconstruction schemes will be high-order in time and space.

With PIF-numerical fluxes, the governing equation can be expressed in a fully discretized form as,

$$\begin{aligned}\mathbf{U}_{i,j,k}^{n+1} &= \mathbf{U}_{i,j,k}^n - \frac{\Delta t}{\Delta x} (\hat{\mathbf{f}}_{i+\frac{1}{2},j,k} - \hat{\mathbf{f}}_{i-\frac{1}{2},j,k}) \\ &\quad - \frac{\Delta t}{\Delta y} (\hat{\mathbf{g}}_{i,j+\frac{1}{2},k} - \hat{\mathbf{g}}_{i,j-\frac{1}{2},k}) \\ &\quad - \frac{\Delta t}{\Delta z} (\hat{\mathbf{h}}_{i,j,k+\frac{1}{2}} - \hat{\mathbf{h}}_{i,j,k-\frac{1}{2}}),\end{aligned}\quad (4.4)$$

which requires only a single update while attaining high-order accuracy both in time and space.

It is worth remarking that the derived governing form in Eq. (4.4) for PIF is something in between those of FVM and FDM. It is different from that of FVM in that it does not carry any spatial average but the temporal average. It is also

different from that of FDM in that it does involve the temporal average in the fluxes in Eq. (4.2), to which the numerical fluxes $\hat{\mathbf{f}}$, $\hat{\mathbf{g}}$, and $\hat{\mathbf{h}}$ approximate.

The time-averaged fluxes are obtained through the Taylor expansion of the pointwise flux around t^n . In the q th-order PIF method, the time-averaged x -directional flux \mathbf{F}^{avg} is approximated as,

$$\begin{aligned}
\mathbf{F}^{avg}(\mathbf{x}) &= \frac{1}{\Delta t} \int_{t^n}^{t^{n+1}} \mathbf{F}(\mathbf{x}, t) dt \\
&= \mathbf{F}(\mathbf{x}, t^n) + \frac{\Delta t}{2!} \partial_t^{(1)} \mathbf{F}(\mathbf{x}, t) \Big|_{t=t^n} + \frac{\Delta t^2}{3!} \partial_t^{(2)} \mathbf{F}(\mathbf{x}, t) \Big|_{t=t^n} + \frac{\Delta t^3}{4!} \partial_t^{(3)} \mathbf{F}(\mathbf{x}, t) \Big|_{t=t^n} + \dots \\
&= \sum_{i=0}^{q-1} \frac{\Delta t^i}{(i+1)!} \partial_t^{(i)} \mathbf{F}(\mathbf{x}, t) \Big|_{t=t^n} + \mathcal{O}(\Delta t^q) \\
&= \mathbf{F}^{appx,q}(\mathbf{x}, t^n) + \mathcal{O}(\Delta t^q).
\end{aligned} \tag{4.5}$$

The *temporally* q th-order approximated fluxes $\mathbf{F}^{appx,q}$ will be used as the inputs of the p th-order reconstruction scheme $\mathcal{R}(\cdot)$ that is combined with a characteristic flux splitting method $\mathcal{FS}(\cdot)$ to apply the p th-order *spatial* approximation to the numerical flux $\hat{\mathbf{f}}$ at cell interfaces,

$$\hat{\mathbf{f}}_{i+\frac{1}{2},j,k} = \mathcal{R} \left(\mathcal{FS} \left(\mathbf{F}_{i-r,j}^{appx,q}, \dots, \mathbf{F}_{i+r+1,j}^{appx,q} \right) \right) + \mathcal{O}(\Delta x^p), \tag{4.6}$$

where r represents the stencil radius required for the p th-order reconstruction method, $\mathcal{R}(\cdot)$. The details of the high-order reconstruction methods, $\mathcal{R}(\cdot)$, and the flux-splitting methods, $\mathcal{FS}(\cdot)$ are described in Chapter 3.

Therefore, the primary objective of the PIF method is to approximate the time-averaged fluxes in the desired order q , i.e., obtaining $\mathbf{F}^{appx,q}$. For instance, the fourth-order PIF method is characterized by the fourth-order approximated time-averaged flux in the x -direction, $\mathbf{F}^{appx,4}$, from the Taylor expansion of the

pointwise flux around t^n . As expressed in Eq. (4.5), the fourth-order PIF method requires

$$\mathbf{F}^{appx,4}(\mathbf{x}) = \mathbf{F}(\mathbf{x}, t^n) + \frac{\Delta t}{2!} \partial_t^{(1)} \mathbf{F}(\mathbf{x}, t) \Big|_{t=t^n} + \frac{\Delta t^2}{3!} \partial_t^{(2)} \mathbf{F}(\mathbf{x}, t) \Big|_{t=t^n} + \frac{\Delta t^3}{4!} \partial_t^{(3)} \mathbf{F}(\mathbf{x}, t) \Big|_{t=t^n}. \quad (4.7)$$

The other y - and z -directional approximated fluxes, $\mathbf{G}^{appx,4}$ and $\mathbf{H}^{appx,4}$, are defined similarly. The only remaining task for the fourth-order PIF method (PIF4) is transforming all the time derivatives in Eq. (4.7) to the corresponding spatial derivatives via LW/CK procedures; thereby we could express Eq. (4.7) in a fully explicit form.

For simplicity, the compact subscript notation of partial derivatives is adopted in the following discussions. The subscripts represent the partial derivatives, and the temporal expression of $t = t^n$ is omitted. In the compact notation, Eq. (2.1) can be rewritten as,

$$\mathbf{U}_t + \nabla \cdot \mathcal{F}(\mathbf{U}) = \mathbf{U}_t + \mathbf{F}_x + \mathbf{G}_y + \mathbf{H}_z = 0. \quad (4.8)$$

By applying the chain rule to \mathbf{F}_t , the evolution equation of the x -flux, \mathbf{F} can be obtained as,

$$\mathbf{F}_t = \mathbf{F}_{\mathbf{U}} \mathbf{U}_t, \quad (4.9)$$

where $\mathbf{F}_{\mathbf{U}}$ is the x -directional flux Jacobian matrix. The above equation can be combined with Eq. (4.8), resulting the explicit expression for \mathbf{F}_t as,

$$\mathbf{F}_t = -\mathbf{F}_{\mathbf{U}} \nabla^f, \quad \text{where } \nabla^f = \mathbf{F}_x + \mathbf{G}_y + \mathbf{H}_z \quad (4.10)$$

The higher-order time derivatives could be achieved by taking partial derivatives

to Eq. (4.10) recursively. As an example, the second-order term is written as

$$\mathbf{F}_{tt} = \mathbf{F}_{\mathbf{UU}} \cdot \nabla^f \cdot \nabla^f - \mathbf{F}_{\mathbf{U}} \cdot \nabla_t^f, \quad (4.11)$$

where

$$\begin{aligned} \nabla_t^f = & -\mathbf{F}_{\mathbf{UU}} \cdot \mathbf{U}_x \cdot \nabla^f - \mathbf{F}_{\mathbf{U}} \cdot \nabla_x^f \\ & - \mathbf{G}_{\mathbf{UU}} \cdot \mathbf{U}_y \cdot \nabla^f - \mathbf{G}_{\mathbf{U}} \cdot \nabla_y^f \\ & - \mathbf{H}_{\mathbf{UU}} \cdot \mathbf{U}_z \cdot \nabla^f - \mathbf{H}_{\mathbf{U}} \cdot \nabla_z^f, \end{aligned} \quad (4.12)$$

and $\mathbf{F}_{\mathbf{UU}}$ is the x -directional flux Hessian tensor. In Euler equations, the flux Hessians, $\mathbf{F}_{\mathbf{UU}}$, $\mathbf{G}_{\mathbf{UU}}$, and $\mathbf{H}_{\mathbf{UU}}$ are the symmetric, rank-3 tensors, so a dot product between the Hessian tensor and a vector is to be understood as a tensor contraction. Thus a double dot product between the Hessian tensor and two vectors, i.e., $\mathbf{F}_{\mathbf{UU}} \cdot (\) \cdot (\)$ yields a vector of the same dimension with \mathbf{U} .

Following the same procedure, an explicit form of the third-order time derivative of the flux can be obtained as,

$$\mathbf{F}_{ttt} = -\mathbf{F}_{\mathbf{UUU}} \cdot \nabla^f \cdot \nabla^f \cdot \nabla^f + 3\mathbf{F}_{\mathbf{UU}} \cdot \nabla^f \cdot \nabla_t^f - \mathbf{F}_{\mathbf{U}} \cdot \nabla_{tt}^f, \quad (4.13)$$

where

$$\begin{aligned} \nabla_{tt}^f = & \mathbf{F}_{\mathbf{UUU}} \cdot \nabla^f \cdot \mathbf{U}_x \cdot \nabla^f + 2\mathbf{F}_{\mathbf{UU}} \cdot \nabla^f \cdot \nabla_x^f - \mathbf{F}_{\mathbf{UU}} \cdot \mathbf{U}_x \cdot \nabla_t^f - \mathbf{F}_{\mathbf{U}} \cdot \nabla_{tx}^f \\ & + \mathbf{G}_{\mathbf{UUU}} \cdot \nabla^f \cdot \mathbf{U}_y \cdot \nabla^f + 2\mathbf{G}_{\mathbf{UU}} \cdot \nabla^f \cdot \nabla_y^f - \mathbf{G}_{\mathbf{UU}} \cdot \mathbf{U}_y \cdot \nabla_t^f - \mathbf{G}_{\mathbf{U}} \cdot \nabla_{ty}^f \\ & + \mathbf{H}_{\mathbf{UUU}} \cdot \nabla^f \cdot \mathbf{U}_z \cdot \nabla^f + 2\mathbf{H}_{\mathbf{UU}} \cdot \nabla^f \cdot \nabla_z^f - \mathbf{H}_{\mathbf{UU}} \cdot \mathbf{U}_z \cdot \nabla_t^f - \mathbf{H}_{\mathbf{U}} \cdot \nabla_{tz}^f, \end{aligned} \quad (4.14)$$

and

$$\begin{aligned}
\nabla_{tx}^f = & \mathbf{F}_{UUU} \cdot \mathbf{U}_x \cdot \nabla^f \cdot \mathbf{U}_x - \mathbf{F}_{UU} \cdot \mathbf{U}_{xx} \cdot \nabla^f - 2\mathbf{F}_{UU} \cdot \nabla_x^f \cdot \mathbf{U}_x - \mathbf{F}_U \cdot \nabla_{xx}^f \\
& - \mathbf{G}_{UUU} \cdot \mathbf{U}_x \cdot \nabla^f \cdot \mathbf{U}_y - \mathbf{G}_{UU} \cdot \mathbf{U}_{xy} \cdot \nabla^f - \mathbf{G}_{UU} \cdot \nabla_x^f \cdot \mathbf{U}_y \\
& - \mathbf{G}_{UU} \cdot \mathbf{U}_x \cdot \nabla_y^f - \mathbf{G}_U \cdot \nabla_{xy}^f \\
& - \mathbf{H}_{UUU} \cdot \mathbf{U}_x \cdot \nabla^f \cdot \mathbf{U}_z - \mathbf{H}_{UU} \cdot \mathbf{U}_{xz} \cdot \nabla^f - \mathbf{H}_{UU} \cdot \nabla_x^f \cdot \mathbf{U}_z \\
& - \mathbf{H}_{UU} \cdot \mathbf{U}_x \cdot \nabla_z^f - \mathbf{H}_U \cdot \nabla_{xz}^f,
\end{aligned} \tag{4.15}$$

and similarly for ∇_{ty}^f and ∇_{tz}^f .

Collecting Eqs. (4.10) to (4.15) the fourth-order approximation of the time-averaged x -flux, $\mathbf{F}^{appx,4}$ can be expressed in the explicit form, as the spatial derivatives are readily approximated through the conventional central differencing schemes. In this dissertation, the conventional five-point central differencing formulae are used:

$$\mathbf{F}_x|_{\mathbf{x}=\mathbf{x}_{ijk}} = \frac{\mathbf{F}_{i-2} - 8\mathbf{F}_{i-1} + 8\mathbf{F}_{i+1} - \mathbf{F}_{i+2}}{12\Delta x} + \mathcal{O}(\Delta x^4), \tag{4.16}$$

$$\mathbf{F}_{xx}|_{\mathbf{x}=\mathbf{x}_{ijk}} = \frac{-\mathbf{F}_{i-2} + 16\mathbf{F}_{i-1} - 30\mathbf{F}_i + 16\mathbf{F}_{i+1} - \mathbf{F}_{i+2}}{12\Delta x^2} + \mathcal{O}(\Delta x^4). \tag{4.17}$$

For the cross derivatives,

$$\mathbf{F}_{xy}|_{\mathbf{x}=\mathbf{x}_{ijk}} = \frac{\mathbf{F}_{i+1,j+1} - \mathbf{F}_{i-1,j+1} - \mathbf{F}_{i+1,j-1} + \mathbf{F}_{i-1,j-1}}{4\Delta x \Delta y} + \mathcal{O}(\Delta x^2, \Delta y^2). \tag{4.18}$$

The above five-points central differencing formulae can produce sufficiently accurate predictions of spatial derivatives for the PIF method. However, these conventional approaches cannot capture the shock discontinuities, leading to unforeseen spurious oscillations at strong shock profiles. (e.g., Sod shock problem)

One solution to this issue is to introduce WENO nonlinear weights in Eq. (3.17) to the central differencing formula. Alike the fifth-order WENO reconstruction scheme, consider the three central differencing schemes approximating the first-order derivatives at $x = x_i$, in each sub-stencil as,

$$\begin{aligned}\mathbf{d}_1 &= \frac{1}{2\Delta x} (\mathbf{F}_{i-2} - 4\mathbf{F}_{i-1} + 3\mathbf{F}_i), \\ \mathbf{d}_2 &= \frac{1}{2\Delta x} (-\mathbf{F}_{i-1} + \mathbf{F}_{i+1}), \\ \mathbf{d}_3 &= \frac{1}{2\Delta x} (-3\mathbf{F}_i + 4\mathbf{F}_{i+1} - \mathbf{F}_{i+2}).\end{aligned}\tag{4.19}$$

Then the goal is to make a convex combination with the nonlinear weights ω_m describing the first-order derivatives at $x = x_i$:

$$\mathbf{F}_x|_{x=x_i} \approx \omega_1 \mathbf{d}_1 + \omega_2 \mathbf{d}_2 + \omega_3 \mathbf{d}_3.\tag{4.20}$$

In a smooth region, following the original context of WENO, the nonlinear weights ω_m are anticipated to be reduced to the linear weights γ_m so that the convex combination represents the approximation of \mathbf{F}_x in a whole five-point stencil. That is to say, the convex combination with the linear weights should be equal to Eq. (4.16),

$$\gamma_1 \mathbf{d}_1 + \gamma_2 \mathbf{d}_2 + \gamma_3 \mathbf{d}_3 = \frac{1}{12\Delta x} (\mathbf{F}_{i-2} - 8\mathbf{F}_{i-1} + 8\mathbf{F}_{i+1} - \mathbf{F}_{i+2}).\tag{4.21}$$

Explicitly, the linear weights for the five-point WENO-*like* central differencing are given by,

$$\gamma_1 = \frac{1}{6} \quad \gamma_2 = \frac{4}{6} \quad \gamma_3 = \frac{1}{6}.\tag{4.22}$$

The nonlinear weights ω_m are calculated in the same way as the classical WENO-JS reconstruction method in Eq. (3.17), with the same choice of the smoothness

indicators, β_m in Eq. (3.18).

Although the fourth-order PIF method requires the second-order derivatives Eq. (4.17) and cross derivatives Eq. (4.18); however, using the WENO-*like* central differencing formula above only for the first-order derivative effectively reduces the oscillations of the PIF method. Needless to say, the WENO-*like* central differencing Eq. (4.20) increases the overall computational loads of the PIF method.

In practical code implementation, it is worth noting that reusing the flux divergence ∇^f for calculating high-order spatial derivatives is more efficient than calculating them directly. For example, ∇_x^f can be calculated as $\text{dx}(\nabla^f)$, with the numerical spatial derivative function $\text{dx}(\cdot)$, rather than calculating as $\nabla_x^f = \mathbf{F}_{xx} + \mathbf{G}_{yx} + \mathbf{H}_{zx}$. This approach requires an additional guard cell layer (resulting in two more guard cells for the five-points derivatives). However, the overall code performance is better than evaluating high-order derivatives in each direction without affecting the accuracy of the scheme.

The PIF method is a very efficient numerical strategy to update the solution in FDM formulation. Once the high-order time-averaged fluxes are determined, the solution can be updated through a single step by following the exact same process for the conventional FDM spatial reconstruction. Using the conventional spatial strategy of the FDM formulation, the PIF method can be “swapped” readily with the SSP-RK scheme in the existing simulation code for improving the code performance.

However, the direct analytic derivations for flux Jacobians, Hessians (and more) remain as the implementation hurdle for the PIF method. Unlike SSP-RK methods, the PIF method requires different code implementation for a different system of equations only because of the *Jacobian-like* terms. (e.g., $\mathbf{F}_U, \mathbf{F}_{UU}, \mathbf{F}_{UUV}, \dots$) This dissertation aims to tackle this problem, making a different strategy to use

the LW/CK procedure, which does not require analytical derivations of *Jacobian-like* terms.

4.2 System-Free Approach

This section aims to provide a new alternate formulation of computing the multiplications of Jacobian-vector and Hessian-vector-vector terms in Eqs. (4.10) to (4.15). The new approach will replace the necessity for analytical derivations of the Jacobian-like terms in the original PIF method that is system-dependent, with a new system-independent formulation, based on the so-called “Jacobian-free” method, which is widely used for Newton-Krylov-type iterative schemes [32, 14, 44, 45].

Suppose the Taylor expansion for the flux vector \mathbf{F} at a small displacement from \mathbf{U} ,

$$\mathbf{F}(\mathbf{U} + \varepsilon\mathbf{V}) = \mathbf{F}(\mathbf{U}) + \varepsilon\mathbf{F}_\mathbf{U} \cdot \mathbf{V} + \frac{1}{2}\varepsilon^2\mathbf{F}_{\mathbf{U}\mathbf{U}} \cdot \mathbf{V} \cdot \mathbf{V} + \mathcal{O}(\varepsilon^3), \quad (4.23a)$$

$$\mathbf{F}(\mathbf{U} - \varepsilon\mathbf{V}) = \mathbf{F}(\mathbf{U}) - \varepsilon\mathbf{F}_\mathbf{U} \cdot \mathbf{V} + \frac{1}{2}\varepsilon^2\mathbf{F}_{\mathbf{U}\mathbf{U}} \cdot \mathbf{V} \cdot \mathbf{V} + \mathcal{O}(\varepsilon^3), \quad (4.23b)$$

where \mathbf{V} is an arbitrary vector that has the same number of components as \mathbf{U} , and ε is a small scalar perturbation. By subtracting Eq. (4.23b) from Eq. (4.23a), we get an expression of a central differencing that is of second-order in ε ,

$$\mathbf{F}_\mathbf{U} \cdot \mathbf{V} = \frac{1}{2\varepsilon} \left[\mathbf{F}(\mathbf{U} + \varepsilon\mathbf{V}) - \mathbf{F}(\mathbf{U} - \varepsilon\mathbf{V}) \right] + \mathcal{O}(\varepsilon^2). \quad (4.24)$$

Alternatively, the first-order forward differencing or the backward differencing can be used here. However, the above second-order central differencing is used for this dissertation, so that the order of accuracy of the entire system-free approach

consistently scales with $\mathcal{O}(\varepsilon^2)$, given that the Hessian approximation described in the following is to be bounded by $\mathcal{O}(\varepsilon^2)$. With the system-free approximation of Jacobian, all the Jacobian-vector products in Eqs. (4.10) to (4.15) are to be replaced with the central differencing in Eq. (4.24).

For the approximation for Hessians, it is imperative to classify the types of the Hessian tensor contraction. The first type is the Hessian tensor contracts with the same vector twice, e.g., $\mathbf{F}_{\mathbf{U}\mathbf{U}} \cdot \mathbf{V} \cdot \mathbf{V}$, and the second type is the tensor contracts with two different vectors, e.g., $\mathbf{F}_{\mathbf{U}\mathbf{U}} \cdot \mathbf{V} \cdot \mathbf{W}$.

For the first type, we use a Taylor expansion analogous to Eq. (4.23) to approximate the Hessian-vector-vector product with a central differencing of order $\mathcal{O}(\varepsilon^2)$,

$$\mathbf{F}_{\mathbf{U}\mathbf{U}} \cdot \mathbf{V} \cdot \mathbf{V} = \frac{1}{\varepsilon^2} \left[\mathbf{F}(\mathbf{U} + \varepsilon \mathbf{V}) - 2\mathbf{F}(\mathbf{U}) - \mathbf{F}(\mathbf{U} - \varepsilon \mathbf{V}) \right] + \mathcal{O}(\varepsilon^2). \quad (4.25)$$

Using a simple vector calculus, the second type can be derived from the first type in Eq. (4.25) by exploring a symmetric property of the Hessians,

$$\mathbf{F}_{\mathbf{U}\mathbf{U}} \cdot \mathbf{V} \cdot \mathbf{W} = \frac{1}{2} \left[\mathbf{F}_{\mathbf{U}\mathbf{U}} \cdot (\mathbf{V} + \mathbf{W}) \cdot (\mathbf{V} + \mathbf{W}) - (\mathbf{F}_{\mathbf{U}\mathbf{U}} \cdot \mathbf{V} \cdot \mathbf{V} + \mathbf{F}_{\mathbf{U}\mathbf{U}} \cdot \mathbf{W} \cdot \mathbf{W}) \right]. \quad (4.26)$$

The Hessian approximations derived here are now ready to be substituted in Eqs. (4.11) to (4.15).

Theoretically speaking, the system-free procedure in the above can be applied to any arbitrary order of derivatives of the flux function \mathbf{F} with respect to the conservative variable \mathbf{U} . For instance, the fourth-order PIF method Eq. (4.7) requires the third-order derivative of \mathbf{F} , i.e., $\mathbf{F}_{\mathbf{U}\mathbf{U}\mathbf{U}}$. Following the same mathematical basis of Eqs. (4.24) and (4.25), the tensor contractions with the same

vectors can be approximated as,

$$\begin{aligned} \mathbf{F}_{\mathbf{U}\mathbf{U}\mathbf{U}} \cdot \mathbf{V} \cdot \mathbf{V} \cdot \mathbf{V} = & \frac{1}{2\varepsilon^3} \left[-\mathbf{F}(\mathbf{U} - 2\varepsilon\mathbf{V}) + 2\mathbf{F}(\mathbf{U} - \varepsilon\mathbf{V}) \right. \\ & \left. - 2\mathbf{F}(\mathbf{U} + \varepsilon\mathbf{V}) + \mathbf{F}(\mathbf{U} + 2\varepsilon\mathbf{V}) \right] + \mathcal{O}(\varepsilon^2). \end{aligned} \quad (4.27)$$

We can further extend the procedure to compute the contraction with three different vectors, \mathbf{V} , \mathbf{W} , and \mathbf{X} ,

$$\begin{aligned} \mathbf{F}_{\mathbf{U}\mathbf{U}\mathbf{U}} \cdot \mathbf{V} \cdot \mathbf{W} \cdot \mathbf{X} = & \frac{1}{6} \left[\mathbf{F}_{\mathbf{U}\mathbf{U}\mathbf{U}} \cdot (\mathbf{V} + \mathbf{W} + \mathbf{X}) \cdot (\mathbf{V} + \mathbf{W} + \mathbf{X}) \cdot (\mathbf{V} + \mathbf{W} + \mathbf{X}) \right. \\ & - \mathbf{F}_{\mathbf{U}\mathbf{U}\mathbf{U}} \cdot (\mathbf{V} + \mathbf{W}) \cdot (\mathbf{V} + \mathbf{W}) \cdot (\mathbf{V} + \mathbf{W}) \\ & - \mathbf{F}_{\mathbf{U}\mathbf{U}\mathbf{U}} \cdot (\mathbf{V} + \mathbf{X}) \cdot (\mathbf{V} + \mathbf{X}) \cdot (\mathbf{V} + \mathbf{X}) \\ & - \mathbf{F}_{\mathbf{U}\mathbf{U}\mathbf{U}} \cdot (\mathbf{W} + \mathbf{X}) \cdot (\mathbf{W} + \mathbf{X}) \cdot (\mathbf{W} + \mathbf{X}) \\ & + \mathbf{F}_{\mathbf{U}\mathbf{U}\mathbf{U}} \cdot \mathbf{V} \cdot \mathbf{V} \cdot \mathbf{V} \\ & + \mathbf{F}_{\mathbf{U}\mathbf{U}\mathbf{U}} \cdot \mathbf{W} \cdot \mathbf{W} \cdot \mathbf{W} \\ & \left. + \mathbf{F}_{\mathbf{U}\mathbf{U}\mathbf{U}} \cdot \mathbf{X} \cdot \mathbf{X} \cdot \mathbf{X} \right], \end{aligned} \quad (4.28)$$

and only to see that the number of terms to be computed rapidly increases in high-order tensor contraction terms.

4.2.1 The proper choices of ε

In the above system-free approximations, the choice of ε has to be considered carefully as it affects the solution accuracy and stability. On one hand, ε is needed to be minimized to improve the approximated solution accuracy, the quality of which will scale as the truncation error of $\mathcal{O}(\varepsilon^2)$. On the other hand, if it is too small the solution would be contaminated by the floating-point roundoff

error which is bounded by the machine accuracy $\varepsilon_{\text{mach}}$ [44]. Therefore, ε is to be determined judiciously to provide a good balance between the two types of error.

A recent study by An et al. [3] presents an effective analysis of choosing ε in the context of the Jacobian-free Newton-Krylov iterative framework. The authors have shown how to compute an ideal value of ε which minimizes the error of the central differencing in the Jacobian-vector approximation.

The main idea in [3] is to find a good balance between the truncation error $\mathcal{O}(\varepsilon^2)$ of each Jacobian-free approximation in Eq. (4.24) and Hessian-free approximation in Eq. (4.25), and the intrinsic floating-point roundoff error $\delta\mathbf{F}(\mathbf{U})$ when calculating the target exact function value $\mathbf{F}(\mathbf{U})$ with an approximate value $\mathbf{F}(\mathbf{U}) + \delta\mathbf{F}(\mathbf{U})$. The perturbation $\delta\mathbf{F}(\mathbf{U})$ may include any errors characterized in computer arithmetic such as roundoff errors, and is assumed to be bounded by the machine accuracy.

Let $\mathbf{F}(\mathbf{U})$ be an exact function value of \mathbf{F} at \mathbf{U} , and let $\mathbf{F}^*(\mathbf{U}) = \mathbf{F}(\mathbf{U}) + \delta\mathbf{F}(\mathbf{U})$ be an approximation to $\mathbf{F}(\mathbf{U})$, where $\delta\mathbf{F}(\mathbf{U})$ is a perturbation of $\mathbf{F}(\mathbf{U})$ that is potentially due from roundoff errors and truncation errors and is assumed to be bounded by the machine accuracy, i.e., $\|\delta\mathbf{F}(\mathbf{U})\| \leq \varepsilon_{\text{mach}}$. The main idea is to choose an optimal ε value for the Jacobian-free approximation Eq. (4.24), $\varepsilon_{\text{jac}}^{op}$, in such a way that the error is minimized when approximating $\mathbf{F}_{\mathbf{U}} \cdot \mathbf{V}$ using the central differencing approximation of $\mathbf{F}^*(\mathbf{U})$ in Eq. (4.24), i.e.,

$$\begin{aligned}\mathbf{F}_{\mathbf{U}} \cdot \mathbf{V} &\approx \frac{1}{2\sigma} [\mathbf{F}^*(\mathbf{U} + \sigma\mathbf{V}) - \mathbf{F}^*(\mathbf{U} - \sigma\mathbf{V})] \\ &= \frac{1}{2\sigma} [\mathbf{F}(\mathbf{U} + \sigma\mathbf{V}) + \delta\mathbf{F}(\mathbf{U} + \sigma\mathbf{V}) - \mathbf{F}(\mathbf{U} - \sigma\mathbf{V}) - \delta\mathbf{F}(\mathbf{U} - \sigma\mathbf{V})].\end{aligned}\tag{4.29}$$

For the sake of this analysis, we assume that the function $\mathbf{F} : \mathbb{R}^n \rightarrow \mathbb{R}^n$ is defined to be continuously differentiable sufficiently everywhere, $\mathbf{F} \in C^k(\mathbb{R}^n)$. We now

define the error E by the difference between the central differencing approximation in Eq. (4.29) and $\mathbf{F}_U \cdot \mathbf{V}$,

$$\begin{aligned}
E &= \frac{1}{2\sigma} [\mathbf{F}^*(\mathbf{U} + \sigma\mathbf{V}) - \mathbf{F}^*(\mathbf{U} - \sigma\mathbf{V})] - \mathbf{F}_U \cdot \mathbf{V} \\
&= \frac{1}{2\sigma} [\mathbf{F}(\mathbf{U} + \sigma\mathbf{V}) - \mathbf{F}(\mathbf{U} - \sigma\mathbf{V})] + \frac{1}{2\sigma} [\delta\mathbf{F}(\mathbf{U} + \sigma\mathbf{V}) - \delta\mathbf{F}(\mathbf{U} - \sigma\mathbf{V})] - \mathbf{F}_U \cdot \mathbf{V} \\
&= \frac{1}{2\sigma} \left[2\sigma\mathbf{F}_U \cdot \mathbf{V} + \sigma^3 \int_0^1 (1-t)^2 \mathbf{F}^{(3)}(\mathbf{U} + t\sigma\mathbf{V}) \cdot \mathbf{V}^3 dt \right] \\
&\quad + \frac{1}{2\sigma} [\delta\mathbf{F}(\mathbf{U} + \sigma\mathbf{V}) - \delta\mathbf{F}(\mathbf{U} - \sigma\mathbf{V})] - \mathbf{F}_U \cdot \mathbf{V} \\
&= \mathcal{O}\left(\frac{\sigma^2}{2} + \frac{\varepsilon_{\text{mach}}}{2\sigma}\right),
\end{aligned} \tag{4.30}$$

where the Taylor series expansion around \mathbf{U} is used for each term in which the remainders after the third power are given as the integral form as below,

$$\begin{aligned}
\mathbf{F}(\mathbf{U} + \sigma\mathbf{V}) &= \mathbf{F}(\mathbf{U}) + \sigma\mathbf{F}_U \cdot \mathbf{V} + \frac{\sigma^2}{2} \partial_U^2 \mathbf{F} \cdot \mathbf{V} \cdot \mathbf{V} \\
&\quad + \frac{\sigma^3}{2} \int_0^1 (1-t)^2 \mathbf{F}^{(3)}(\mathbf{U} + t\sigma\mathbf{V}) \cdot \mathbf{V}^3 dt, \\
\mathbf{F}(\mathbf{U} - \sigma\mathbf{V}) &= \mathbf{F}(\mathbf{U}) - \sigma\mathbf{F}_U \cdot \mathbf{V} + \frac{\sigma^2}{2} \partial_U^2 \mathbf{F} \cdot \mathbf{V} \cdot \mathbf{V} \\
&\quad - \frac{\sigma^3}{2} \int_0^1 (1-t)^2 \mathbf{F}^{(3)}(\mathbf{U} + t\sigma\mathbf{V}) \cdot \mathbf{V}^3 dt.
\end{aligned} \tag{4.31}$$

The optimal choice of $\varepsilon_{\text{jac}}^{op}$ is to be obtained by considering the minimization problem of the leading error term in the last line in Eq. (4.30),

$$\varepsilon_{\text{jac}}^{op} = \arg \min_{\sigma>0} \left(\frac{\sigma^2}{2} + \frac{\varepsilon_{\text{mach}}}{2\sigma} \right) = \left(\frac{\varepsilon_{\text{mach}}}{2} \right)^{\frac{1}{3}} \approx 4.8062 \times 10^{-6}, \tag{4.32}$$

where $\varepsilon_{\text{mach}} \sim 2.2204 \times 10^{-16}$ is used assuming a double-precision in a typical 64-bit machine.

Following the similar procedures, the optimal epsilon value for the Hessian-free

approximation Eq. (4.25), $\varepsilon_{\text{hes}}^{op}$ can be found as,

$$\varepsilon_{\text{hes}}^{op} = \arg \min_{\sigma > 0} \left(\frac{\sigma^2}{3} + \frac{\varepsilon_{\text{mach}}}{\sigma^2} \right) = (3\varepsilon_{\text{mach}})^{\frac{1}{4}} \approx 1.6065 \times 10^{-4}. \quad (4.33)$$

However, direct use of ε^{op} as the displacement step size in the central differencing schemes in Eq. (4.24) and Eq. (4.25) is not a good idea for stability reasons. Usually, the vector \mathbf{V} in Eq. (4.24) and Eq. (4.25) could have an enormous value in a strong shock region, so it is safer to use a smaller step size to preserve the needed stability. To meet this, the ideal value, ε^{op} should be normalized by the magnitude of the vector \mathbf{V} . There are several prescriptions available in the Jacobian-free Newton–Krylov literatures [44, 14] to help finalize the decision of choosing a proper value of ε as a function of ε^{op} . Nonetheless, as reported in [48], a simple approach of taking a square root of ε^{op} with a simple normalization is sufficient to attain the desired accuracy and stability, which is given as,

$$\bar{\varepsilon} = \frac{\sqrt{\varepsilon^{op}}}{\|\mathbf{V}\|_2}. \quad (4.34)$$

Lastly, the ε estimation can be finalized by taking the minimum value between $\bar{\varepsilon}$ and Δt ,

$$\varepsilon = \min(\bar{\varepsilon}, \Delta t), \quad (4.35)$$

to prevent the division by zero case.

4.3 Recursive System-Free Approach

The original system-free (SF) approach presented in the previous section provides good approximations of tensor contractions between *Jacobian-like* terms and vectors. However, the original SF method becomes less attractive for any PIF

method higher than third-order accuracy, as it demands increasing complexity in code implementation, which results in a significant loss in the overall performance of the code. For example, Eq. (4.28) requires 28 times flux function calls for just getting a single tensor contraction, $\mathbf{F}_{\mathbf{U}\mathbf{U}} \cdot \mathbf{V} \cdot \mathbf{W} \cdot \mathbf{X}$. It is worth noting that the major bottleneck of the original SF method stems from Eq. (4.26) and Eq. (4.28) that require to perform the *Jacobian-like* approximations multiple times.

To avoid the additional modifications for the case of the tensor contractions with different vectors, the improved version of the SF method was proposed in [49]. This new, improved SF method, apply the Jacobian-free method recursively to construct the high-order Jacobian-like terms.

The recursive SF method starts from defining a functional \mathcal{D}_u that represents the Jacobian-free method denoted in Eq. (4.24):

$$\mathbf{F}_{\mathbf{U}} \cdot \mathbf{V} \approx \mathcal{D}_u(\mathbf{F}; \mathbf{V}) := \frac{1}{2\varepsilon_v} \left[\mathbf{F}(\mathbf{U} + \varepsilon_v \mathbf{V}) - \mathbf{F}(\mathbf{U} - \varepsilon_v \mathbf{V}) \right], \quad (4.36)$$

where ε_v is the appropriately calculated ε corresponding to the vector \mathbf{V} by following the original system-free method Eq. (4.34),

$$\varepsilon_v = \min (\bar{\varepsilon}_v, \Delta t), \quad \text{where } \bar{\varepsilon}_v = \frac{\sqrt{\varepsilon^{op}}}{\|\mathbf{V}\|_2}. \quad (4.37)$$

The recursive SF method uses $\varepsilon^{op} = 4.8062 \times 10^{-6}$ that is the optimal ε value for the second-order Jacobian-free approximation in the 64-bit machine as it shown in Eq. (4.32). This choice is also justifiable for the recursive scheme considered below, where the functional \mathcal{D}_u itself is defined as the Jacobian-free method fundamentally.

By applying \mathcal{D}_u in the following successive fashion, the tensor contractions between higher order derivatives for the flux function \mathbf{F} and arbitrary vectors.

For instance, the Hessian approximation becomes,

$$\begin{aligned}
\mathbf{F}_{\mathbf{U}\mathbf{U}} \cdot \mathbf{V} \cdot \mathbf{W} &\approx \mathcal{D}_u \left(\mathcal{D}_u(\mathbf{F}; \mathbf{V}); \mathbf{W} \right) \\
&= \frac{1}{4\varepsilon_v\varepsilon_w} \left[\mathbf{F}(\mathbf{U} + \varepsilon_v \mathbf{V} + \varepsilon_w \mathbf{W}) - \mathbf{F}(\mathbf{U} - \varepsilon_v \mathbf{V} + \varepsilon_w \mathbf{W}) \right. \\
&\quad \left. - \mathbf{F}(\mathbf{U} + \varepsilon_v \mathbf{V} - \varepsilon_w \mathbf{W}) + \mathbf{F}(\mathbf{U} - \varepsilon_v \mathbf{V} - \varepsilon_w \mathbf{W}) \right]. \tag{4.38}
\end{aligned}$$

Again, following Eq. (4.37), ε_v and ε_w are the optimal ε values normalized by its corresponding vectors \mathbf{V} and \mathbf{W} , respectively.

Note that the improved version of the Hessian-free method in Eq. (4.38) is applicable regardless the tensor contraction is with two identical vectors (e.g., $\mathbf{F}_{\mathbf{U}\mathbf{U}} \cdot \mathbf{V} \cdot \mathbf{V}$) or with two distinct vectors (e.g., $\mathbf{F}_{\mathbf{U}\mathbf{U}} \cdot \mathbf{V} \cdot \mathbf{W}$), hence it does not require separate formulations as in Eqs. (4.26) and (4.28).

The simplicity gain from the improved version of the system-free method is further rewarded when considering the higher-order derivatives of \mathbf{F} . Following the equivalent strategy, the tensor contraction of the third-order derivative of the flux function, $\mathbf{F}_{\mathbf{U}\mathbf{U}\mathbf{U}}$ with three distinct vectors, \mathbf{V} , \mathbf{W} , and \mathbf{X} is written compactly as,

$$\begin{aligned}
\mathbf{F}_{\mathbf{U}\mathbf{U}\mathbf{U}} \cdot \mathbf{V} \cdot \mathbf{W} \cdot \mathbf{X} &\approx \mathcal{D}_u \left(\mathcal{D}_u \left(\mathcal{D}_u(\mathbf{F}; \mathbf{V}); \mathbf{W} \right); \mathbf{X} \right) \\
&= \frac{1}{8\varepsilon_v\varepsilon_w\varepsilon_x} \left[\mathbf{F}(\mathbf{U} + \varepsilon_v \mathbf{V} + \varepsilon_w \mathbf{W} + \varepsilon_x \mathbf{X}) - \mathbf{F}(\mathbf{U} - \varepsilon_v \mathbf{V} + \varepsilon_w \mathbf{W} + \varepsilon_x \mathbf{X}) \right. \\
&\quad - \mathbf{F}(\mathbf{U} + \varepsilon_v \mathbf{V} - \varepsilon_w \mathbf{W} + \varepsilon_x \mathbf{X}) + \mathbf{F}(\mathbf{U} - \varepsilon_v \mathbf{V} - \varepsilon_w \mathbf{W} + \varepsilon_x \mathbf{X}) \\
&\quad - \mathbf{F}(\mathbf{U} + \varepsilon_v \mathbf{V} + \varepsilon_w \mathbf{W} - \varepsilon_x \mathbf{X}) + \mathbf{F}(\mathbf{U} - \varepsilon_v \mathbf{V} + \varepsilon_w \mathbf{W} - \varepsilon_x \mathbf{X}) \\
&\quad \left. + \mathbf{F}(\mathbf{U} + \varepsilon_v \mathbf{V} - \varepsilon_w \mathbf{W} - \varepsilon_x \mathbf{X}) - \mathbf{F}(\mathbf{U} - \varepsilon_v \mathbf{V} - \varepsilon_w \mathbf{W} - \varepsilon_x \mathbf{X}) \right] \tag{4.39}
\end{aligned}$$

Here, the performance between the recursive SF method and the original SF method can be compared by the number of flux function calls. For instance, considering the case of approximating $\mathbf{F}_{UUU} \cdot \mathbf{V} \cdot \mathbf{W} \cdot \mathbf{X}$ term, the original SF method requires 28 function calls. On the other hand, the recursive SF method needs only eight evaluations. This is a huge improvement in both performance and compactness.

By utilizing Eqs. (4.36) to (4.39), all the tensor contractions needed in the fourth-order PIF method in Eqs. (4.10) to (4.15) can be approximated without the analytical calculations of the *Jacobian-like* terms. Combining the recursive SF method, the PIF method can be implemented more efficiently, allowing the system independence of the high-order scheme. It should be noted that the recursive modifications of the SF method presented in this section do not affect the solution's accuracy and stability compared to the original SF method.

The fourth-order SF-PIF4 method can be summarized as the following step-wise fashion. The discretization indices i, j, k and n are omitted for simplicity in representing the conservative variables \mathbf{U}_{ijk}^n and the corresponding fluxes $\mathcal{F}_{ijk}^n = (\mathbf{F}_{ijk}^n, \mathbf{G}_{ijk}^n, \mathbf{H}_{ijk}^n)$.

Step 1: Calculate $\nabla^f = \mathbf{F}_x + \mathbf{G}_y + \mathbf{H}_z$ via the standard fourth-order accurate, five-point central differencing scheme on every grid point and save them. These saved flux divergences will be used as inputs for the central differencing formulae in the following steps to get higher-order spatial derivatives.

Step 2: Apply the Jacobian approximation in Eq. (4.36) in preparation for \mathbf{F}_t as expressed in Eq. (4.10), and construct the second-order temporally averaged flux $\mathbf{F}^{appx,2} = \mathbf{F} + \Delta t \mathbf{F}_t / 2$. Apply the similar procedures to $y-$ and $z-$ directional fluxes to obtain $\mathbf{G}^{appx,2}$ and $\mathbf{H}^{appx,2}$. This finalizes the

second-order temporal approximations of pointwise fluxes in all directions.

Step 3: Given the pointwise conservative variables \mathbf{U} and the divergence of fluxes ∇^f from **Step 1**, calculate $\mathbf{U}_x, \mathbf{U}_y, \mathbf{U}_z, \nabla_x^f, \nabla_y^f$, and ∇_z^f via the same five-point central differencing operator in **Step 1**. They will be used as building blocks for constructing $\mathbf{F}_{tt}, \mathbf{G}_{tt}$ and \mathbf{H}_{tt} in the following steps.

Step 4: Apply the Jacobian and Hessian approximations in Eqs. (4.36) and (4.38) to the spatially approximated derivative quantities in **Step 3** in order to compute ∇_t^f by following the explicit expression in Eq. (4.12).

Step 5: Apply the Jacobian approximation in (4.36) to ∇_t^f from **Step 4** and the Hessian approximation in (4.38) to ∇^f from **Step 1** in order to get \mathbf{F}_{tt} using Eq. (4.11); add the computed \mathbf{F}_{tt} to the results of **Step 2** to update the second-order temporal fluxes in **Step 2** to the third-order temporally averaged flux, $\mathbf{F}^{appx,3} = \mathbf{F}^{appx,2} + \Delta t^2 \mathbf{F}_{tt}/6$. Perform the similar procedures in y - and z -directions to obtain $\mathbf{G}^{appx,3}$ and $\mathbf{H}^{appx,3}$. This finalizes the third-order temporal approximations of pointwise fluxes in all directions.

Step 6: Using the five-point central differencing, compute the fourth-order accurate approximations of the second derivatives and the mixed-derivatives of the conservative variables and the divergence of fluxes to obtain $\mathbf{U}_{xx}, \mathbf{U}_{xy}, \mathbf{U}_{yy}, \dots$ etc. and $\nabla_{xx}^f, \nabla_{xy}^f, \nabla_{yy}^f, \dots$ etc.

Step 7: Apply the tensor contractions of the first, second, and third-order flux derivatives in Eqs. (4.36), (4.38) and (4.39) to the quantities computed and stored from the previous steps in order to calculate ∇_{tt}^f and ∇_{tx}^f by following the explicit relations in Eqs. (4.14) and (4.15) respectively. Also calculate ∇_{ty}^f and ∇_{tz}^f similarly.

Step 8: Next, perform the last set of tensor contractions in Eqs. (4.36), (4.38) and (4.39) to construct \mathbf{F}_{ttt} as expressed in Eq. (4.13). Add the resulting \mathbf{F}_{ttt} to the result of **Step 5** to obtain the fourth-order temporally averaged flux, $\mathbf{F}^{appx,4} = \mathbf{F}^{appx,3} + \Delta t^3 \mathbf{F}_{ttt} / 24$. Perform the similar procedures in $y-$ and $z-$ directions to obtain $\mathbf{G}^{appx,4}$ and $\mathbf{H}^{appx,4}$. This finalizes the fourth-order temporal approximations of pointwise fluxes in all directions.

Step 9: Proceed with the conventional FDM procedures for high-order spatial accuracy, viz., apply a high-order reconstruction method with a characteristic flux-splitting strategy in Eq. (4.6) to the results, $\mathbf{F}^{appx,4}$, $\mathbf{G}^{appx,4}$, and $\mathbf{H}^{appx,4}$, from **Step 8**. For example, taking WENO-JS (Section 3.1.1) as a reconstruction method using $\mathbf{F}^{appx,4}$ ensures a temporally fourth-order and spatially fifth-order accurate approximation to the numerical flux, $\hat{\mathbf{f}} = \text{WENO-JS}(\mathbf{F}^{appx,4}) + \mathcal{O}(\Delta x^5, \Delta t^4)$. Perform the similar procedures in $y-$ and $z-$ directions to obtain $\hat{\mathbf{g}}$ and $\hat{\mathbf{h}}$.

Step 10: Lastly, update the solution following Eq. (4.4).

4.4 System-Free PIF method with Source term

Math is looking good, but missing numerical results

Since the PIF method depends on the LW/CK procedure, the PIF method must be modified accordingly when the governing equation has changed. For instance, the non-homogeneous system of equations with source term $\mathbf{S}(\mathbf{U})$, the solution updating strategy for the original PIF method Eq. (4.1) should be modified with appropriately time-averaged source term. Consider a conservative equations

with a source term $\mathbf{S}(\mathbf{U})$,

$$\mathbf{U}_t + \nabla \cdot \mathcal{F}(\mathbf{U}) = \mathbf{S}(\mathbf{U}), \quad (4.40)$$

taking time-averaging,

$$\mathbf{U}^{n+1} = \mathbf{U}^n - \Delta t (\partial_x \mathbf{F}^{avg} + \partial_y \mathbf{G}^{avg} + \partial_z \mathbf{H}^{avg}) + \Delta t \mathbf{S}^{avg}, \quad (4.41)$$

where

$$\begin{aligned} \mathbf{S}^{avg}(\mathbf{x}) &= \frac{1}{\Delta t} \int_{t^n}^{t^{n+1}} \mathbf{S}(\mathbf{x}, t) dt \\ &= \sum_{i=0}^{q-1} \frac{\Delta t^i}{(i+1)!} \partial_t^{(i)} \mathbf{S}(\mathbf{x}, t) \Big|_{t=t^n} + \mathcal{O}(\Delta t^q) \\ &= \mathbf{S}^{appx,q}(\mathbf{x}, t^n) + \mathcal{O}(\Delta t^q). \end{aligned} \quad (4.42)$$

for the fourth-order PIF method,

$$\mathbf{S}^{appx,4}(\mathbf{x}) = \mathbf{S}(\mathbf{x}, t^n) + \frac{\Delta t}{2!} \partial_t^{(1)} \mathbf{S}(\mathbf{x}, t) \Big|_{t=t^n} + \frac{\Delta t^2}{3!} \partial_t^{(2)} \mathbf{S}(\mathbf{x}, t) \Big|_{t=t^n} + \frac{\Delta t^3}{4!} \partial_t^{(3)} \mathbf{S}(\mathbf{x}, t) \Big|_{t=t^n}. \quad (4.43)$$

In order to modify the conventional PIF procedures in a way that maintaining the general mathematical structures in Section 4.1, consider a modified flux divergence $\widetilde{\nabla}^f$ defined as,

$$\widetilde{\nabla}^f := \nabla^f - \mathbf{S}. \quad (4.44)$$

Then, the time derivatives of the source term can be calculated through the LW/CK procedures as,

$$\mathbf{S}_t = -\mathbf{S}_{\mathbf{U}} \widetilde{\nabla}^f, \quad (4.45)$$

$$\mathbf{S}_{tt} = \mathbf{S}_{\mathbf{U}\mathbf{U}} \cdot \widetilde{\nabla}^f \cdot \widetilde{\nabla}^f - \mathbf{S}_{\mathbf{U}} \cdot \widetilde{\nabla}_t^f, \quad (4.46)$$

$$\mathbf{S}_{ttt} = -\mathbf{S}_{UUU} \cdot \widetilde{\nabla}^f \cdot \widetilde{\nabla}^f \cdot \widetilde{\nabla}^f + 3\mathbf{S}_{UU} \cdot \widetilde{\nabla}^f \cdot \widetilde{\nabla}_t^f - \mathbf{S}_U \cdot \widetilde{\nabla}_{tt}^f. \quad (4.47)$$

The equation independence property of the system-free method is rewarded in calculations of the source Jacobian \mathbf{S}_U and Hessian \mathbf{S}_{UU} , since the only required job is to change the flux function in Eqs. (4.36) and (4.38) to the source function, $\mathbf{S}(\mathbf{U})$.

The time derivatives of the modified flux divergence, $\widetilde{\nabla}_t^f$ and $\widetilde{\nabla}_{tt}^f$, can be defined as linear combinations with the time derivatives of the conventional flux divergence terms as,

$$\begin{aligned}\widetilde{\nabla}_t^f &= \nabla_t^f - \mathbf{S}_t \\ &= \nabla_t^f + \mathbf{S}_U \cdot \widetilde{\nabla}^f,\end{aligned}\quad (4.48)$$

and

$$\begin{aligned}\widetilde{\nabla}_{tt}^f &= \nabla_{tt}^f + (\mathbf{S}_U \cdot \widetilde{\nabla}^f)_t \\ &= \nabla_{tt}^f - \mathbf{S}_{UU} \cdot \widetilde{\nabla}^f \cdot \widetilde{\nabla}^f + \mathbf{S}_U \cdot \widetilde{\nabla}_t^f,\end{aligned}\quad (4.49)$$

where ∇_t^f and ∇_{tt}^f are defined in Eqs. (4.12) and (4.14), respectively.

With a new governing equation, Eq. (4.40), the high-order time derivatives of the flux functions, e.g., \mathbf{F}_t , \mathbf{F}_{tt} , and \mathbf{F}_{ttt} in Eq. (4.7) should be adjusted with the modified flux divergence, $\widetilde{\nabla}^f$. The governing equation Eq. (4.40) leads the adjusted first time derivative as,

$$\mathbf{F}_t = -\mathbf{F}_U \widetilde{\nabla}^f. \quad (4.50)$$

Using the modified flux divergence, $\widetilde{\nabla}^f$, the adjusted time derivatives of the flux functions maintain the similar mathematical structures in Eqs. (4.10), (4.11)

and (4.13) as,

$$\mathbf{F}_{tt} = \mathbf{F}_{\mathbf{UU}} \cdot \widetilde{\nabla}^f \cdot \widetilde{\nabla}^f - \mathbf{F}_{\mathbf{U}} \cdot \widetilde{\nabla}_t^f, \quad (4.51)$$

and

$$\mathbf{F}_{ttt} = -\mathbf{F}_{\mathbf{UUU}} \cdot \widetilde{\nabla}^f \cdot \widetilde{\nabla}^f \cdot \widetilde{\nabla}^f + 3\mathbf{F}_{\mathbf{UU}} \cdot \widetilde{\nabla}^f \cdot \widetilde{\nabla}_t^f - \mathbf{F}_{\mathbf{U}} \cdot \widetilde{\nabla}_{tt}^f, \quad (4.52)$$

where $\widetilde{\nabla}_t^f$ and $\widetilde{\nabla}_{tt}^f$ are defined as in Eqs. (4.48) and (4.49) respectively.

4.5 Conclusion

The Picard integral formulation (PIF) method is one of the Lax-Wendroff class high-order in temporal integration strategies for FDM discretization. By virtue of a single-stage time integrator, the PIF method can perform faster than the traditional multi-stage method. Also, the PIF method does not depend on the spatial reconstruction scheme; thus, it can be combined with any high-order spatial method in general.

However, as like other Lax-Wendroff type schemes, the PIF method highly depends on the system of equations, requiring analytical derivations for *Jacobian-like* terms. Although the symbolic manipulation tools can aid these calculations, *Jacobian-like* terms remain as a major implementation hurdle due to their perplexing structures.

The (original, non-recursive) system-free (SF) approach provides capability to Lax-Wendroff type scheme to bypass all the analytical derivations of Jacobian-like terms, approximating tensor contractions between Jacobian-like terms and arbitrary vectors. The major advantage of SF method lies in ease of its code implementation for practical use. By combining with PIF method, SF-PIF method can be applied to any system of equations to furnish high-order in temporal accuracy in a single-step. However, the increasing number of calculations needed for

higher order derivatives of the flux function \mathbf{F} with respect to the conservative variables \mathbf{U} makes the SF method less attractive for higher than third-order PIF method.

The improved version, recursive SF approach is then introduced to minimize the number of calculation needed for approximating the tensor contractions. The recursive SF method introduced a functional representing the Jacobian-free method, then the higher order derivative terms can be obtained by applying the functional recursively. This feature allows to extend SF-PIF method to the fourth-order accuracy efficiently.

It is important to note that the SF method is neither designed particularly for the PIF method nor any specific numerical methods in CFD. Instead, it is solely intended for approximating the Jacobian-like tensor contractions, so the SF approach is applicable in other numerical algorithms to enhance the calculation speed and implementation efficiency.

Chapter 5

Results

This chapter will provide various numerical test results of SF-PIF methods. In order to examine the numerical capabilities of the SF method, several well-known numerical benchmark problems are conducted, and the traditional SSP-RK methods' results will be provided with the same initial conditions as counterparts of SF-PIF methods for comparisons. SF-PIF3 and SF-PIF4 will refer to the *recursive* SF method in Section 4.3 with third-order and fourth-order PIF methods, respectively, and RK3 and RK4 will refer to the three-stage, third-order SSP-RK method Eq. (3.45), five-stage, fourth-order SSP-RK method Eq. (3.47), respectively. The original SF approach (Section 4.2) with the PIF method is denoted by oSF-PIF. The conventional five-point central differencing formulae Eqs. (4.16) to (4.18) are used for SF-PIF and PIF methods otherwise specified.

5.1 Performance of SF-PIF method

The main advantage of the PIF method is the performance gain compared to the SSP-RK methods. This section will compare the performance of PIF methods (with or without the SF approach) and the SSP-RK method. The main purpose of

this section is to check if the SF-PIF methods provide improved performance while maintaining the same accuracy as SSP-RK methods. Theoretically speaking, the SF and oSF approach should not affect the solution's accuracy and stability, so the original PIF method's results are presented for comparisons.

All test results in this section use the standard fifth-order WENO-JS method (Section 3.1.1) for the spatially high-order reconstruction scheme. Therefore, the expected truncation error is $\mathcal{O}(\Delta s^5, \Delta t^q)$, where q is the order of the temporal scheme.

5.1.1 Sine wave advection

The first choice of the benchmark problem is the sine wave advection to test if the desired solution accuracy is retrieved in smooth flows. The initial condition follows the setup in [47], where the density profile is initialized with a sinusoidal wave, $\rho(x) = 1.5 - 0.5 \sin(2\pi x)$. The x -velocity and the pressure are set as constant values of $u = 1$ and $p = 1/\gamma$ with the specific heat ratio, $\gamma = 5/3$. Albeit solved using the nonlinear Euler equations, the problem is solved in a linear regime, viz., the velocity and pressure remain constant for all $t \geq 0$ so that the initial sinusoidal density profile is purely advected by the constant velocity $u = 1$ without any nonlinear dynamics such as a formation of shocks and rarefactions.

The simulation domain is defined on a one-dimensional box of $[0, 1]$ with the periodic boundary condition on both ends. The density profile will propagate one period through the computational domain and will return to its initial position at $t = 1$. In return, any shape deformation of the density profile from the initial density profile can be considered as a numerical error associated with phase errors or numerical diffusions. The accuracy of the numerical solutions is measured by computing L_1 error between the initial and the final density profiles. The

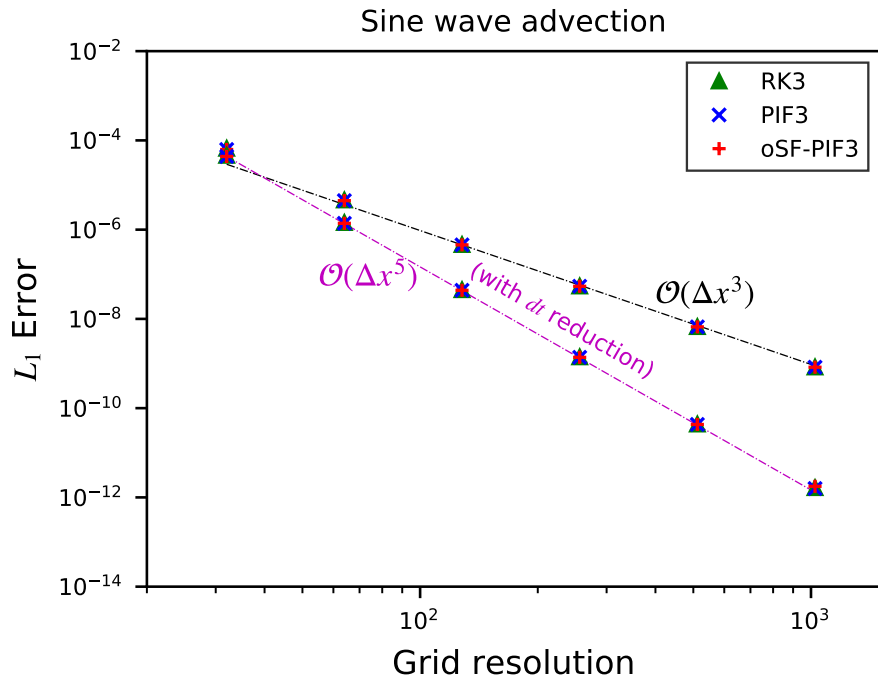


Figure 5.1: Convergence test for the 1D sine wave advection problem. The errors are calculated in L_1 sense against the initial density profile resolved on the computational grids refined from 32 to 1024 by a factor of 2. All numerical solutions follow the theoretical third-order convergence rate (the black-dotted line) when using the timesteps computed from the Courant condition. Also plotted are the solutions of using reduced timesteps, which follows the fifth-order convergence rate represented in the pink-dotted line.

numerical experiment results from the sine wave advection test on different number of grid points, $N_x = 32, 64, 128, 256, 512$, and 1024 are depicted in Fig. 5.1 for three different temporal methods, Rk3, PIF3, and oSF-PIF3.

There are two types of convergence rates demonstrated in Fig. 5.1. In the first type, the numerical solutions of three different temporal methods advanced with timesteps computed from the Courant condition with $C_{\text{cfl}} = 0.7$. Interestingly, the numerical solutions from all three different temporal methods show a third-order convergence rate, indicating that the leading error term from third-order temporal methods dominates the spatial error from the fifth-order WENO-JS method. These results are different from Fig. 1.1, calculating L_1 error from the 2D nonlinear vortex advection case, where the solution accuracy follows the spatial order at low-resolution regions until the leading error of the solution is caught up by the temporal error as computational grids get further refined to higher resolutions. However, in this test case, the third-order temporal accuracy quickly takes control throughout the entire range of the grid resolutions tested herein. This solution behavior strongly supports the importance of integrating spatially reconstructed solutions with a temporal scheme whose accuracy is sufficiently high enough to be well comparable to that of the spatial solver.

In the second type of the convergence rate, on the other hand, the timesteps are restricted in order to match up the lower third-order temporal accuracy with the higher fifth-order spatial accuracy. Following the usual trick of timestep reduction in [54], the timestep Δt_N is manually adjusted on a grid size of N to satisfy the equal rate of change between the spatial and temporal variations. The restricted timestep is defined by,

$$\Delta t_N = \Delta t_0 \left(\frac{\Delta x_N}{\Delta x_0} \right)^{\frac{5}{3}}, \quad (5.1)$$

where the sub-indices “0” and N refer to the time and grid scales on a nominal

coarse and fine resolution, respectively. In the current configuration, Δx_0 is the grid-scale of $N_x = 32$, and Δt_0 is the corresponding timestep subject to the Courant condition with $C_{\text{cfl}} = 0.7$. With the timestep reduction, the overall leading error from the spatial and temporal methods are matched with the fifth-order spatial accuracy of WENO5, and the numerical solution of PIF3 and oSF-PIF3 follows the fifth-order convergence rate as expected. In all test cases for linear advection problems, the oSF-PIF3 solutions behave almost equally well with the solutions of the original PIF3 and RK3 both quantitatively and qualitatively.

5.1.2 Nonlinear isentropic vortex advection

The isentropic vortex advection problem [68] is one of the most popular benchmark tests to measure the numerical method's accuracy and performance in the nonlinear case. Although the problem is fully nonlinear, the exact solution always exists in the form of its initial condition, from which an isentropic vortex is advected through periodic boundaries in a 2D computational box. The accuracy of a numerical method on a nonlinear problem can be evaluated by comparing the final density profile with the initial condition.

The initial condition consists of a constant background mean flow with $\rho = 1$, $(u, v) = (1, 1)$ and $p = 1$ on the 2D computational domain with periodic boundary conditions. The isentropic vortex is given by the velocity perturbations $(\delta u, \delta v)$, and the temperature perturbation δT . The perturbation terms are designed to set the constant entropy S everywhere in the simulation domain, i.e., $\delta S = 0$. The perturbations are given as,

$$(\delta u, \delta v) = \frac{\epsilon}{2\pi} e^{-\frac{1}{2}(1-r^2)}(-y, x), \quad \delta T = -\frac{(\gamma - 1)\epsilon^2}{8\gamma\pi^2}e^{1-r^2}, \quad (5.2)$$

where $\epsilon = 5$ is the vortex strength and $r^2 = x^2 + y^2$. The vortex is initially located

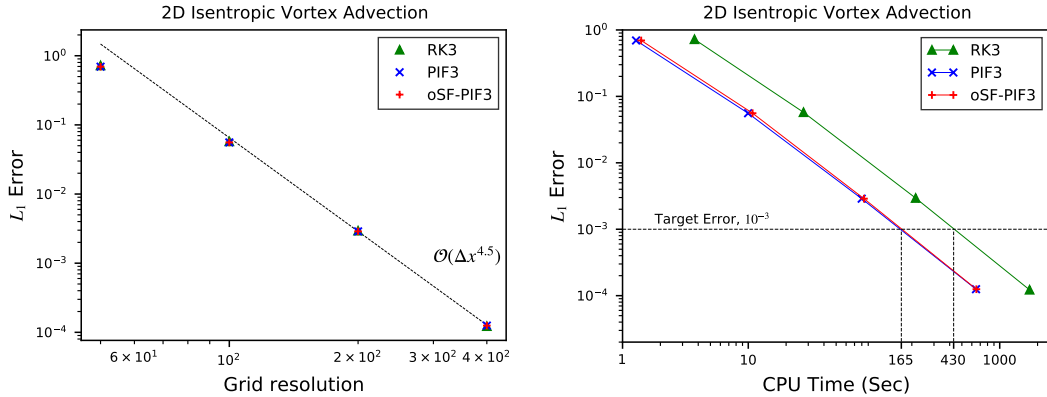


Figure 5.2: The L_1 errors of the isentropic vortex advection test problem on different grid resolutions, $N_x = N_y = 50, 100, 200$, and 400 . The three different third-order temporal schemes are used combined with WENO5 spatial method. The L_1 errors with respect to the grid resolutions (**left**); with respect to the computation time (**right**).

at the domain center, and it advects to the diagonal directions, then returns to its original position after one cycle. The simulation domain size is doubled-up as $[0, 20] \times [0, 20]$ compared to the original setup in [68], to prevent vortex-vortex couplings near the periodic boundaries as reported in [72].

The results of the convergence test are depicted on the left panel in Fig. 5.2. Three different temporal schemes, RK3, PIF3, and oSF-PIF3, show an excellent comparable match in magnitudes and slopes of the L_1 errors with varying grid resolution, $N_x = N_y = 50, 100, 200$, and 400 . One important finding in this figure is that there is no significant distinction between PIF3 and oSF-PIF3 in accuracy and performance. These results demonstrate that the original SF method does not affect the solution accuracy and performance of the PIF method.

The performance results of three different temporal schemes are presented on the right panel of Fig. 5.2 and summarized in Table 5.1. Both the PIF3 and oSF-PIF3 methods perform more than two times faster than the multi-stage method, RK3. It is worth noting that the original SF-PIF method, oSF-PIF, can be readily swappable with an RK integrator in an existing code without too much

Table 5.1: The L_1 errors, the rates of convergence, and the relative computation times for the vortex advection test. Here, the comparison between RK3 and oSF-PIF is only displayed, since the difference between oSF-PIF3 and PIF3 is indistinguishable. All the performance results (measured in seconds) are averaged over 10 simulation runs which are conducted on a Coffee Lake quad-core i7 Intel CPU with a clock speed of 2.7GHz, Turbo Boost up to 4.5GHz, utilizing four parallel threads.

$N_x = N_y$	RK3				oSF-PIF3			
	L_1 error	L_1 order	CPU Time	Speedup	L_1 error	L_1 order	CPU Time	Speedup
50	7.22×10^{-1}	—	3.73 s	1.0	6.95×10^{-1}	—	1.41 s	0.38
100	5.76×10^{-2}	3.65	27.51 s	1.0	5.58×10^{-2}	3.64	10.82 s	0.39
200	2.94×10^{-3}	4.29	214.44 s	1.0	2.89×10^{-3}	4.27	83.21 s	0.39
400	1.22×10^{-4}	4.59	1727.71 s	1.0	1.26×10^{-4}	4.52	652.18 s	0.38

effort, leaving any existing spatial implementations intact. Moreover, such a code transformation with oSF-PIF is more advantageous in simplicity than the original PIF method because oSF-PIF replaces the analytic derivations of the Jacobian and Hessian terms with the system-free approximations, which have shown to be highly commensurate with the analytical counterparts of the original PIF scheme.

Unlike the 1D linear sine advection test in Section 5.1.1, the overall solution accuracy is not completely dominated by the third-order temporal discretizations, which could reduce the overall convergence rate down to third-order as observed in the sine advection case. Concurrently, the solution does not converge at full fifth-order either, the rate due to the use of WENO5. This can be explained as a nonlinear effect in which the lower third-order time integration schemes slightly compromise the overall leading error term of the fifth-order spatial discretization.

However, the third-order temporal schemes gradually degrade the overall solution accuracy on the fine grid resolutions. Fig. 5.3 illustrates the same convergence test results, but in this case, containing more higher grid resolutions, $N_x = N_y = 120, 200, 400, 800, 1600$, and 3200. Notice that the recursive SF-PIF method, SF-PIF3, and SF-PIF4 are used instead of the original SF-PIF

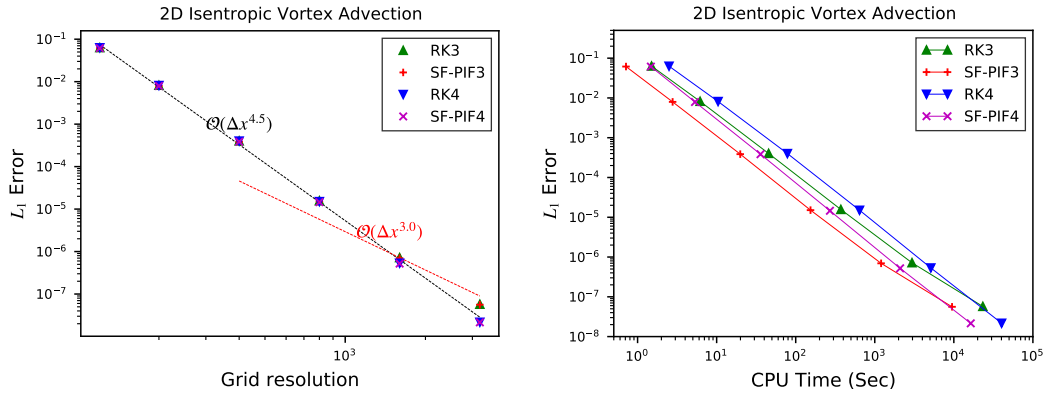


Figure 5.3: The L_1 errors of the isentropic vortex advection test problem solved by third- and fourth-order temporal schemes combined with WENO5 spatial method. The L_1 errors with respect to the grid resolutions (**left**); with respect to the computation time (**right**).

method. As expected, all temporal methods follow the convergence line of order $\sim \mathcal{O}(\Delta x^{4.5})$, which is nearly the same as WENO’s fifth-order spatial accuracy, equivalently in Fig. 5.2. However, at the critical grid resolution, $N_x = N_y = 1600$, the third-order temporal schemes of RK3 and SF-PIF3 start to compromise the overall solution accuracy. This behavior can be explained that the spatial errors from the fifth-order WENO method are dominant on the grid resolutions up to $N_x = N_y = 1600$, after which the truncation errors associated with the third-order temporal methods become dominant over the error of the fifth-order spatial solver, WENO5. This result emphasizes the importance of high-order temporal methods in fine grid resolution: a high-order spatial method does require a *comparably* high-order temporal method to maintain the overall quality of the solutions, mainly when adding more grid resolutions to resolve finer scales more accurately. Otherwise, lower-order accuracy from the temporal solver can potentially degrade the solution accuracy, contradicting the intended motivation.

The performance results of recursive SF-PIF methods can be found on the right panel of Fig. 5.3 and Table 5.2. As shown in the right panel of Fig. 5.3,

Table 5.2: The L_1 errors, the rates of convergence, and the computation times for the vortex advection test solved using RK3 and SF-PIF3 methods (**top**); using RK4 and SF-PIF4 methods (**bottom**). All simulation runs are performed on the four 20-cores Cascade Lake Intel Xeon processors, utilized 64 parallel threads. CPU times are measured in seconds, averaged over 10 individual runs.

$N_x = N_y$	RK3				SF-PIF3			
	L_1 error	L_1 order	CPU Time	Speedup	L_1 error	L_1 order	CPU Time	Speedup
120	6.31×10^{-2}	—	1.50 s	1.0	6.16×10^{-2}	—	0.71 s	0.48
200	8.20×10^{-3}	4.00	6.17 s	1.0	7.96×10^{-3}	4.00	2.77 s	0.45
400	4.02×10^{-4}	4.35	45.44 s	1.0	3.86×10^{-4}	4.37	19.89 s	0.44
800	1.57×10^{-5}	4.68	372.47 s	1.0	1.51×10^{-5}	4.68	153.92 s	0.41
1600	7.18×10^{-7}	4.45	2957.26 s	1.0	6.95×10^{-7}	4.44	1203.10 s	0.41
3200	5.72×10^{-8}	3.65	23 274.37 s	1.0	5.60×10^{-8}	3.63	9494.65 s	0.41

$N_x = N_y$	RK4				SF-PIF4			
	L_1 error	L_1 order	CPU Time	Speedup	L_1 error	L_1 order	CPU Time	Speedup
120	6.30×10^{-2}	—	2.50 s	1.0	6.14×10^{-2}	—	1.47 s	0.59
200	8.15×10^{-3}	4.00	10.42 s	1.0	7.91×10^{-3}	4.01	5.33 s	0.51
400	4.01×10^{-4}	4.35	78.47 s	1.0	3.85×10^{-4}	4.36	35.89 s	0.46
800	1.51×10^{-5}	4.73	641.50 s	1.0	1.46×10^{-5}	4.72	270.94 s	0.42
1600	5.33×10^{-7}	4.82	5115.47 s	1.0	5.21×10^{-7}	4.81	2091.20 s	0.41
3200	2.17×10^{-8}	4.62	40 195.034 s	1.0	2.15×10^{-8}	4.60	16 377.73 s	0.41

the SF-PIF3 method is the fastest method in reaching any given target L_1 error threshold until $N_x = 1600$. However, on any grid resolutions finer than the critical resolution, $N_x = 1600$, SF-PIF3’s L_1 error drops to the third-order convergence rate, which ultimately crosses the straight convergence line of SF-PIF4. SF-PIF3’s error will remain larger than the errors from the fourth-order temporal methods as long as the convergence rate follows the pattern at the high-resolution trail.

On the other hand, it is distinctively superior to see that SF-PIF4’s solution reaches any fixed target error in a *faster* CPU time than the third-order RK3’s solution while keeping the numerical errors as low as RK4 results at all grid resolution tested herein. Remark that Table 5.2 shows quantitatively that the SF-PIF4 method performs *faster* than the RK3 method, producing more accurate solutions at any grid resolution.

5.1.3 Sod shock tube problem

The Sod's shock tube problem [71] is the one of the most famous 1D hydrodynamics test problems for testing a numerical scheme's capability to handle discontinuities and shocks. The initial condition is given as,

$$(\rho, u, p) = \begin{cases} (1, 0, 1) & \text{for } x \leq 0.5, \\ (0.125, 0, 0.1) & \text{for } x > 0.5, \end{cases} \quad (5.3)$$

in a simulation box of $[0, 1]$, with outflow boundary conditions on both ends at $x = 0$ and $x = 1$. This benchmark problem is an excellent practice to test if the PIF and oSF-PIF methods can capture the shock discontinuities appropriately.

The numerical solutions with the grid size of $N_x = 256$ at $t = 0.2$ are plotted as symbols in each panel of Fig. 5.4. The solid lines on each panel represent the reference solution resolved on a more finer grid size, $N_x = 1024$, by using WENO5+RK3. The results resolved with recursive SF-PIF3 methods are omitted in this figure, since the differences between SF-PIF3 and oSF-PIF3 are indistinguishable.

As illustrated in Fig. 5.4b and Fig. 5.4c, oSF-PIF3 method produce almost identical results of PIF3, agreeing with the reference solutions and RK3's solutions in Fig. 5.4a. However, both in PIF3 and oSF-PIF3 methods, there is a slight oscillation in the x-velocity immediately behind the shock front. This small oscillation is originated from the use of the conventional central differencing formulae in Eq. (4.16) for both oSF-PIF3 and PIF3.

The WENO-*like* differencing strategy in Eqs. (4.19) to (4.22) can resolve this oscillation. As displayed in Fig. 5.4d, the interchanging central differencing to WENO-differencing helps to improve the performance of oSF-PIF3 at the

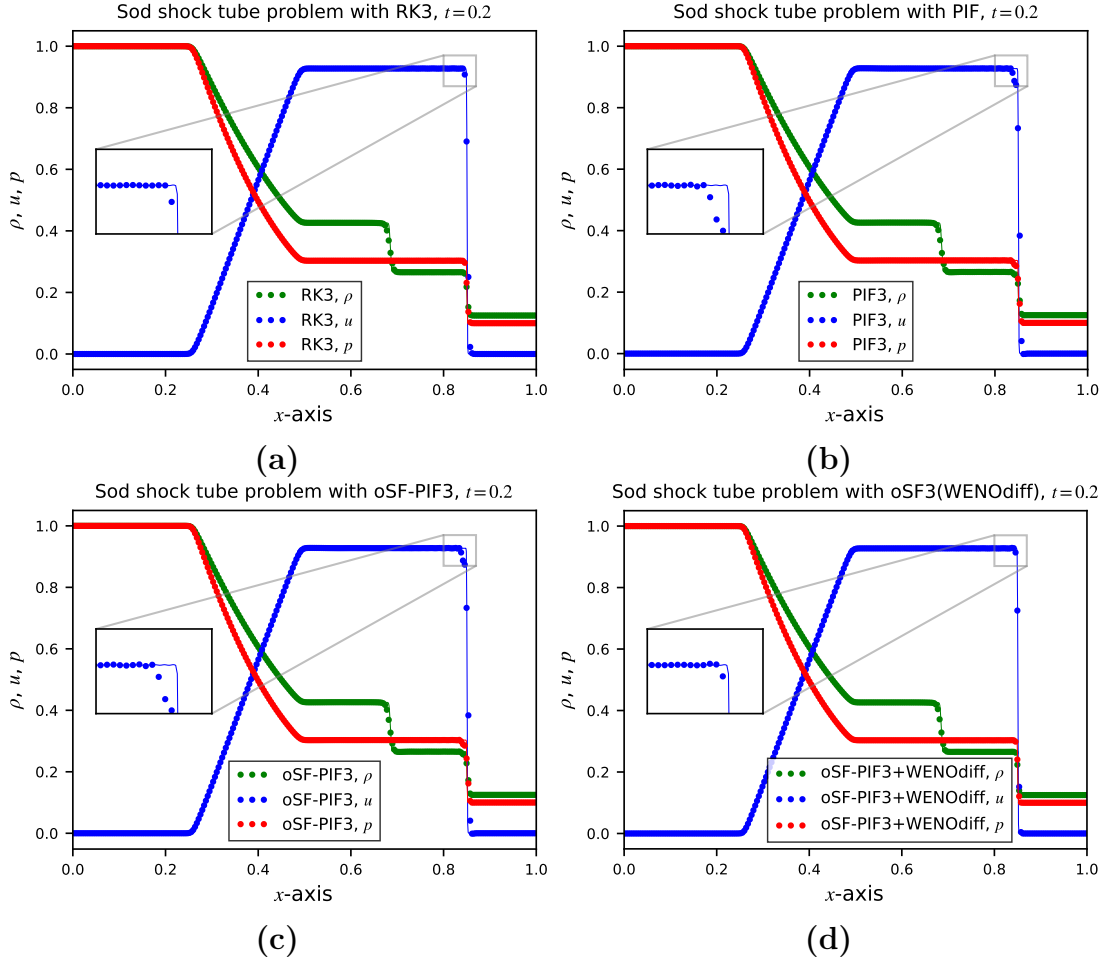


Figure 5.4: Sod's shock tube problem at $t = 0.2$. The reference solutions are over-plotted as solid lines in each panel, which are resolved on a grid resolution of $N_x = 1024$ with RK3. The symbols in each panel represent the solution resolved on $N_x = 256$ grid cells with (a) RK3, (b) PIF3, and (c) oSF-PIF3. (d), the solution is resolved with oSF-PIF3 method combining with a new WENO-like numerical differentiate operator, described as in Eqs. (4.19) to (4.22).

shock, suppressing the post-shock oscillations observed in Fig. 5.4b and Fig. 5.4c. With this small fix, the oSF-PIF3 results are almost identical to the RK3 results in Fig. 5.4a. Computationally, the WENO-*like* differencing adds extra floating-point operations, which consequently slows down oSF-PIF's and SF-PIF's overall performance. For this reason, the WENO-*like* discretization was employed only on the Sod's shock-tube test as a guide, while it was opt-out on the rest of the test problems in this dissertation where any unphysical has not been observed shock/discontinuity oscillations.

5.1.4 Implosion test

The next problem to consider is the implosion test problem introduced by Hui et al. [39]. An unsteady flow configuration is given as an initial condition which launches a converging shock wave towards the domain center. Following a more straightforward version by Liska and Wendroff [50], the only right upper quadrant of the original setup in [39] is taken as the simulation domain. In this setup, the simulation is initialized on a region of a 2D square box, $[0, 0.3] \times [0, 0.3]$, enclosed with reflecting walls, in which case a converging shock wave is launched toward the lower-left corner at $(x, y) = (0, 0)$. The initial shock wave bounces at the reflecting walls and produces a double Mach reflection along two edges of $x = 0$ and $y = 0$. Consequently, two jets are formed along the edges, moving toward the origin $(x, y) = (0, 0)$ and collide with each other. This two-jet collision then ejects a newly-formed jet into the diagonal direction $x = y$. Reflecting shocks continuously interact with the diagonal jet, turning it into a long and narrow shape over time. The observed structures of filaments and fingers along with the diagonal jet and at its base are progressively intensified by the Ritchmyer-Meshkov instability, a level of which depends sensitively on numerical dissipation.

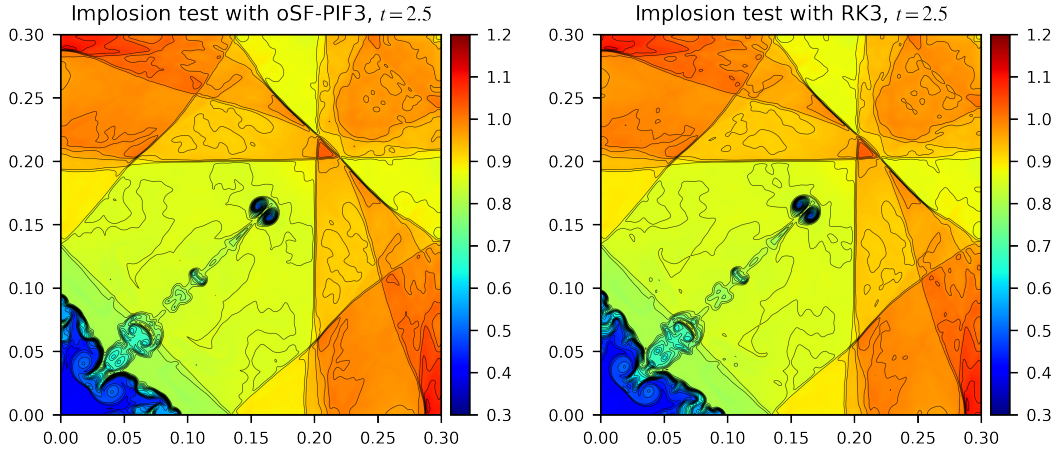


Figure 5.5: The density profile of the implosion test with oSF-PIF3 (left) and with RK3 (right). The color map ranges from 0.3 to 1.2, and 40 evenly-spaced contour lines are over-plotted with the same range.

The shape of the jet is the key view point of the implosion test since it is a good indicator of a numerical method's symmetric property and numerical dissipation. If the numerical scheme fails to maintain a high level of symmetry, the jet will eventually be derailed off-diagonally and deformed over time. Besides, an excess amount of numerical dissipation will turn the jet into a less narrow and less elongated shape along the diagonal.

The density maps of the implosion test performed on 400×400 grid resolution at $t = 2.5$ are displayed in Fig. 5.5. The result with oSF-PIF3 is on the left panel in Fig. 5.5 and RK3 on the right. These results can also be directly compared with Fig. 4.7 in [50] and Fig. 17 in [75]. The results of oSF-PIF3 (as well as RK3) present the well-maintained symmetric jet along the diagonal direction at a sufficient level. At the same time, the shape of the diagonal jet using oSF-PIF3 matches well with the shape using RK3, and hence is sufficient to demonstrate that the numerical dissipation in oSF-PIF3 is well-managed compared with RK3.

5.1.5 Shallow water equations

One of the essential features of the SF-PIF methods is that the SF-PIF methods can be applicable to any other system without changing the high-order parts of the simulation codes. As an example of the system independence feature, the simulation result by changing the system of equations to the 2D shallow water equations (SWE) without a source term is presented in this section. In SWE, the conservative variables and the flux functions are defined by,

$$\mathbf{U} = \begin{bmatrix} h \\ hu \\ hv \end{bmatrix}, \quad \mathbf{F}(\mathbf{U}) = \begin{bmatrix} hu \\ hu^2 + \frac{1}{2}gh^2 \\ huv \end{bmatrix}, \quad \mathbf{G}(\mathbf{U}) = \begin{bmatrix} hv \\ huv \\ hv^2 + \frac{1}{2}gh^2 \end{bmatrix}. \quad (5.4)$$

Here, h is the vertical depth of the fluid, $\mathbf{v} = (u, v)$ is a vector of vertically-averaged velocity components in x - and y -directions. Denoted as g is a gravitational acceleration in the negative vertical z -direction, which is averaged out in the derivation of the shallow water equations.

The sole purpose of presenting the new system of equations above is to demonstrate the flexibility of SF-PIF schemes, in that the system-free approach allows an easy code implementation without the need for other analytical derivations of new Jacobian-*like* terms of the new governing system. By virtue of the system-independent property of the SF-PIF methods, the process of changing from the 2D Euler code to the 2D SWE code is no more than switching the governing equations without touching anything on the high-order numerical parts. This process is much simpler than other Lax-Wendroff type schemes (PIF, for example), where each governing system should re-calculate the Jacobian-*like* terms.

The well-known circular dam-breaking problem [2, 79, 24] is conducted to validate the numerical capability of the SF-PIF method in SWE. Initially, a

volume of still water is confined in the virtual (i.e., invisible) cylindrical wall with a radius of 11 meters (m), located at the center of simulation domain, [50 m × 50 m] resolved on a 100×100 grid resolution. The depth of the water inside of the wall is 10 m and 1 m outside. This configuration would be considered as an SWE version of 2D Riemann problem. Explicitly, the initial condition is given as,

$$(h, u, v) = \begin{cases} (10 \text{ m}, 0, 0) & \text{for } r \leq 11 \text{ m}, \\ (1 \text{ m}, 0, 0) & \text{for } r > 11 \text{ m}, \end{cases} \quad (5.5)$$

where r is the distance from the center of domain, $r = \sqrt{(x - 25 \text{ m})^2 + (y - 25 \text{ m})^2}$. The outflow boundary condition is applied for both directions, and the gravitational acceleration is $g = 9.81 \text{ m s}^{-2}$. Again, the Courant number is set to $C_{\text{cfl}} = 0.4$.

The results of the simulation with the oSF-PIF3 method are presented in Fig. 5.6. The figure represents well-comparable numerical solutions with the results using the same configuration reported in [2, 79, 24]. As shown in Fig. 5.6, the overall spherical symmetry and the sharp profile at the wavefront are well-maintained in each snapshot at four different times, $t = 0.345, 0.69, 1.035$, and 1.38 .

5.2 SF-PIF method with WENO-JS

All recursive SF-PIFs

5.2.1 The Shu-Osher problem (rotated 45°)

The Shu-Osher problem [70] is a well-known benchmark problem that describes the interactions between a Mach 3 shock and a smooth density profile. Initially, a Mach 3 shock wave travels to the right through a sinusoidally perturbed density

Circular Dam Breaking with oSF-PIF3

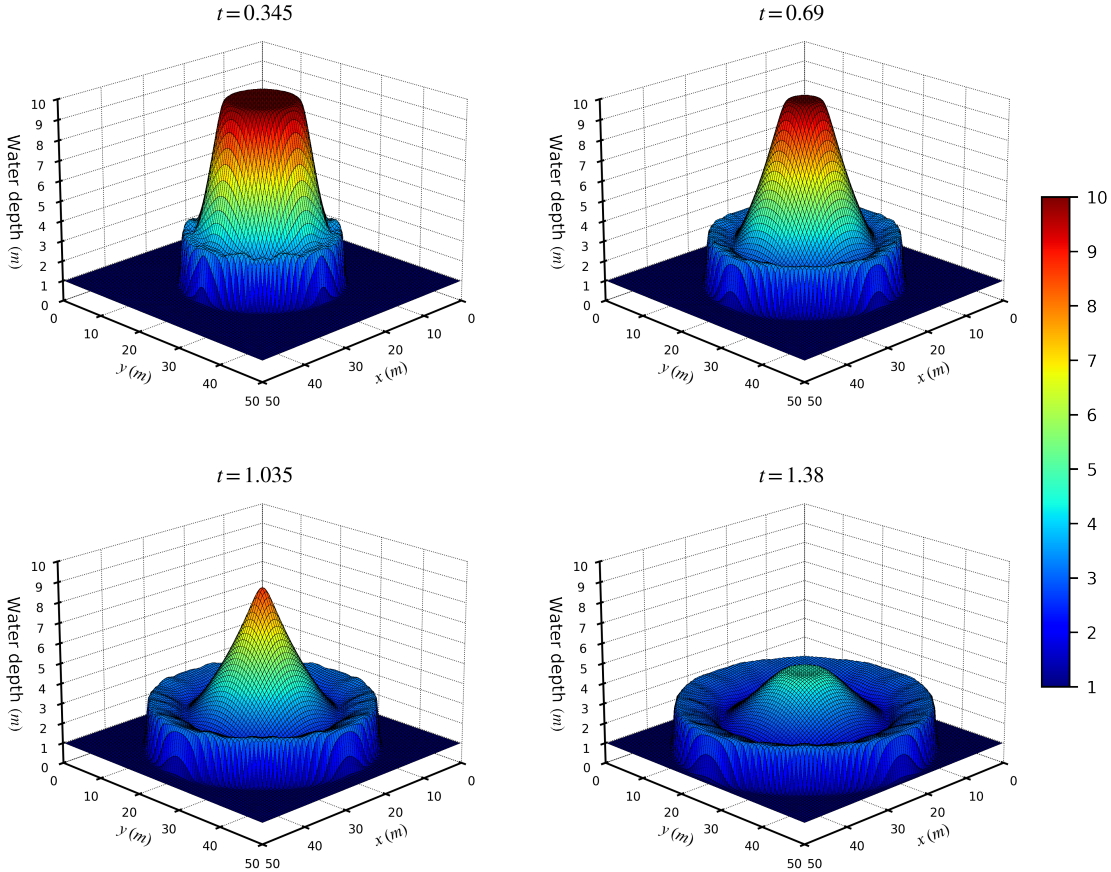


Figure 5.6: Snapshots of the circular dam breaking simulation at four different times, $t = 0.345, 0.69, 1.035$, and 1.38 seconds. A volume of water in rest is initially confined in a cylindrical dam of a radius $r = 11$ m and a height $h = 10$ m. The simulation starts with an instantaneous removal of the cylindrical wall located at the center of the domain $[50 \text{ m} \times 50 \text{ m}]$ resolved on a grid resolution of 100×100 . The gravitational force is exerted on the steady water, which triggers the onset of the gravitational collapse of the entire volume of water, making the circular splash in the outer rim as well as the ripple effects in the central region that move radially outward in time.

profile. As the shock wave propagates along the perturbed region, the profile gets compressed, resulting in a frequency-doubled region behind the shock. As the shock wave moves further to the right, the doubled-frequency region returns to its original frequency, at which point it becomes a sequence of sharp profile instead of smooth sine wave due to the shock-steepening.

In this section, the Shu-Osher problem is performed in 2D by inclining the shock wave direction by an angle of $\theta = 45^\circ$, adopting the idea of Kawai [42], where the initial conditions are repeated multiple times along the direction of the wave propagation so that the problem may be executed with periodic boundary conditions. Explicitly, the initial condition is given as,

$$\mathbf{U}(x_{\parallel}, t = 0) = \begin{cases} \mathbf{U}_L & \text{for } x_{\parallel} \leq 1, \quad 11 < x_{\parallel} \leq 21, \quad 31 < x_{\parallel} \leq 40, \\ \mathbf{U}_R & \text{for } 1 < x_{\parallel} \leq 11, \quad 21 < x_{\parallel} \leq 31, \end{cases}$$

$$\text{where } \mathbf{U}_L = \begin{bmatrix} \rho = 3.857143 \\ u = 2.629369 \cos(\pi/4) \\ v = 2.629369 \sin(\pi/4) \\ p = 10.33333 \end{bmatrix}, \quad \mathbf{U}_R = \begin{bmatrix} \rho = 1 + 0.2 \sin(5x_{\parallel}) \\ u = 0 \\ v = 0 \\ p = 1 \end{bmatrix}. \quad (5.6)$$

$x_{\parallel} = x \cos \theta + y \sin \theta$ is the direction parallel to the wave propagation and the simulation domain is a periodic box of $[0, 20/\cos \theta] \times [0, 20/\sin \theta]$. With this configuration, the 1D test problem, Shu-Osher test, can be performed on the diagonal direction of 2D periodic box. The same 1D solution is expected by following the diagonal direction, x_{\parallel} , and taking only the bottom-left quarter of the diagonal axis. Therefore, the number of data points of this result profiles would be a quarter of the 2D grid resolution, i.e., $N_{\parallel} = N_x/4 = N_y/4$. The 2D density map of the initial and final conditions are plotted in Fig. 5.7.

The density profiles of the bottom-left quarter of the diagonal axis x_{\parallel} are given

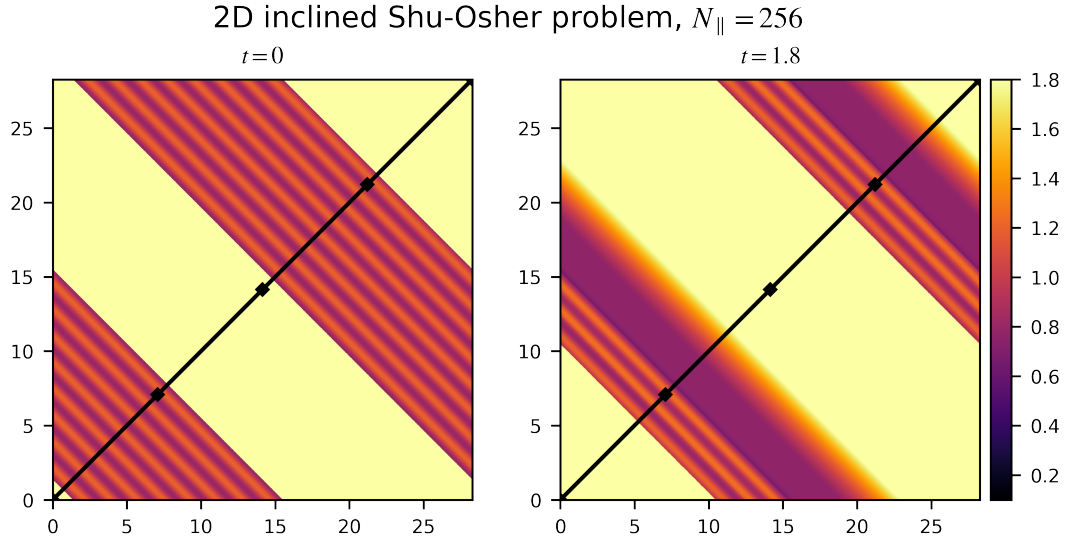


Figure 5.7: 2D density maps of inclined 2D Shu-Osher test problem at $t = 0$ and $t = 1.8$. The test was performed on a 2D simulation box of 1024×1024 resolution with the SF-PIF4 method. The solid black line represents the shock propagating direction, x_{\parallel} , and squares divide the line in each quartile.

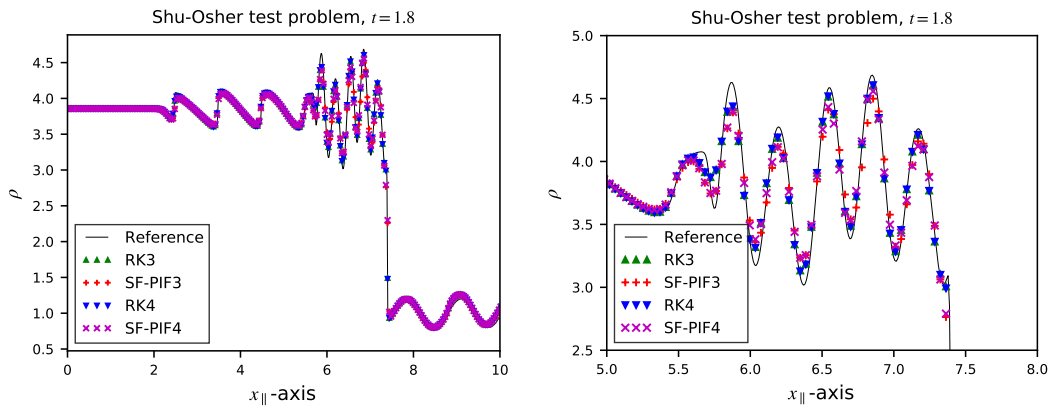


Figure 5.8: One dimensional density profiles along the x_{\parallel} direction of the inclined Shu-Osher problem at $t = 1.8$. The solid line represents the reference solution, solved by RK4 with 1024 data points in the diagonal axis, i.e., $N_{\parallel} = 1024$. All other solutions, represented by the symbols, are resolved on an $N_{\parallel} = 256$ grid resolution in the diagonal axis. The detailed view of the high-frequency region is shown on the right panel.

in Fig. 5.8. All tests are performed on a box of resolution $N_x = N_y = 1024$, so the effective resolution of each profile is $N_{\parallel} = 256$, except for the reference solution, which performed on a finer grid, $N_{\parallel} = 1024$. The four different temporal methods, RK3, RK4, SF-PIF3, and SF-PIF4 produce reasonably acceptable solution profiles capturing the high-frequency amplitudes fairly well in the frequency-doubled region. Generally, RK methods capture the amplitudes marginally better, but in the left-most part of the double-frequency region, $x \approx 5.8$, SF-PIF methods capture the highest peak of the amplitude better than the RK methods near the transition between the frequency doubling and the shock steepened perturbations.

5.2.2 2D Riemann problem: Configuration 3

The two-dimensional Riemann problem is a widespread benchmark problem to test the methods' ability to capture the complex fluid structures in 2D. This specific setup and other types of configurations have been extensively studied in [87, 63, 64] and have been adopted as prevalent benchmark test problems. This dissertation follows the initial condition of Configuration 3 described in [25, 47, 48, 49].

The simulation domain is set on 1600×1600 grid resolution, which is generally considered as a very high resolution in 2D simulation. This grid resolution choice is made based on the observation in Section 5.1.2 to ensure that the temporal errors are comparable to or dominant over the spatial errors; thereby, the temporal error dominant results are anticipated that allows to see the different behaviors of four different temporal solvers.

The results at $t = 0.8$ are shown in Fig. 5.9. The pseudo-colors represent the density map ranging between $[0.1, 1.8]$, and 40 contour lines within the same range are over-plotted as solid black lines.

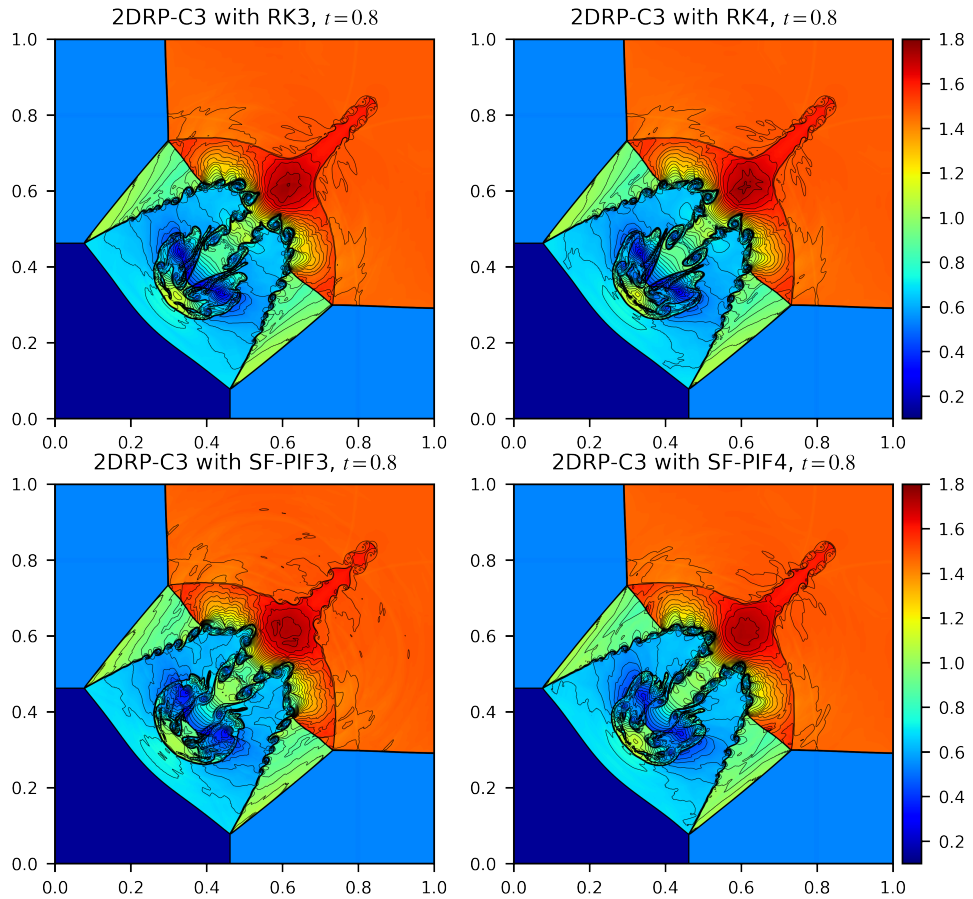


Figure 5.9: The density maps of Configuration 3 at $t = 0.8$. **Left column:** The solutions using RK3 (top) and SF-PIF3 (bottom). **Right column:** The solutions using RK4 (top) and SF-PIF4 (bottom). Forty levels of black contour lines are over-plotted in each figure with the same range of the color map. All simulations are performed on a 1600×1600 grid resolution.

As illustrated in the figures, all four different temporal schemes produce well-known, acceptable results, keeping the assumed diagonal symmetry exceptionally well on this high resolution. This problem is highly nonlinear, involving formations of the upward-moving jet, the downward-moving mushroom-jet, secondary Kelvin-Helmholtz instabilities exhibited as the small-scale vortical rollups along the slip lines and along the stems of the two jets. Therefore, it is a non-trivial task to address if a method under consideration is *better* or *worse* based on the number of such rollups in the simulations without a systemic comparison analysis requiring extensive, careful validation and verification tests that are beyond the scope of this dissertation. At best, such quantification can only provide proof of intrinsic information about the amount of numerical dissipation of each method. From this perspective, one concludes that the two SF-PIF solutions produce the equivalent amount of vortical rollups compared with the corresponding RK solutions, although their different shapes on the downward jets, confirming the validity of the recursive SF-PIF methods on the presence of the shocks in 2D simulations.

5.2.3 Double Mach reflection

The double Mach reflection (DMR) test problem was firstly introduced by Woodward and colella [84]. At initial, a planar shock is located at the left side of the domain with a 30° to the reflecting bottom surface. As the shock propagates to the right, the bottom wall continuously bounces off the shock wave and creates a round reflected shock. The initial condition is the same as the original setup in [84], except for the doubled the y -domain size following [43] to prevent numerical artifacts from the top boundary interaction with the secondary shock wave and the slip line.

As the solution evolves, two contact discontinuities and two Mach stems are

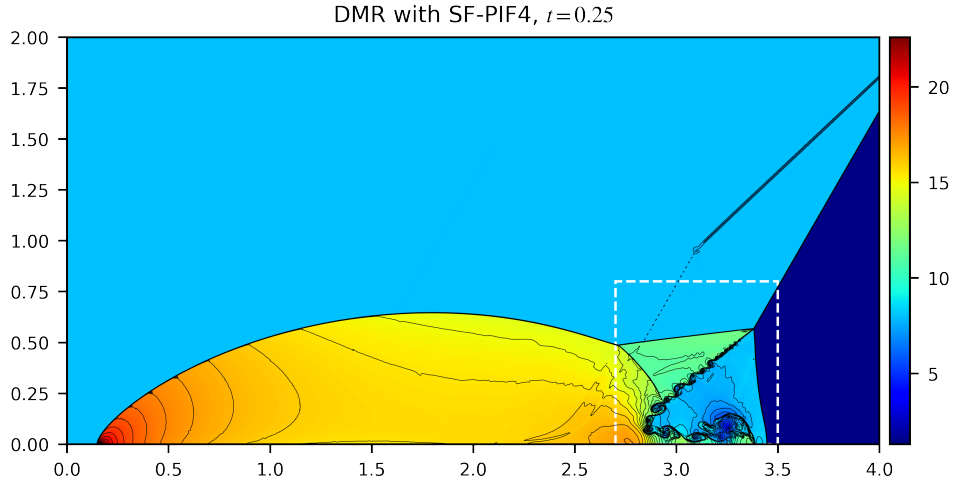


Figure 5.10: The solution density profile of Double Mach reflection test solved with SF-PIF4 method on a 4096×2048 grid resolution. The solid black curves represent the forty levels of contour lines ranging within the same range of the colormap. The white-dotted rectangle is the main point of interest in this simulation, where the jet and the primary triple point are formed. More detailed view of the rectangle region with different temporal solvers are plotted in Fig. 5.11.

formed, as well as a jet along the bottom surface. The formation of the jet is similar to the formation of the two jets in implosion test (Section 5.1.4), the collision of which led to the upward moving diagonal jet. The solution density profiles resolved with the SF-PIF4 method is portrayed in Fig. 5.10.

Fig. 5.11 shows the zoomed-in views of the main point of interest in the DMR problem, the vicinity of the jet and the primary triple point, resolved with four different temporal solvers. Again, the results from the third- and fourth-order SF-PIF methods produce well-acceptable results compared to the corresponding RK methods. There are minor differences in the shape of Kelvin-Helmholtz instabilities along the primary slip line and the bottom jet, but the overall dynamics of the two SF-PIF solutions match well with the RK solutions, validating the fidelity of the proposed SF-PIF methods in the presence of a strong shock.

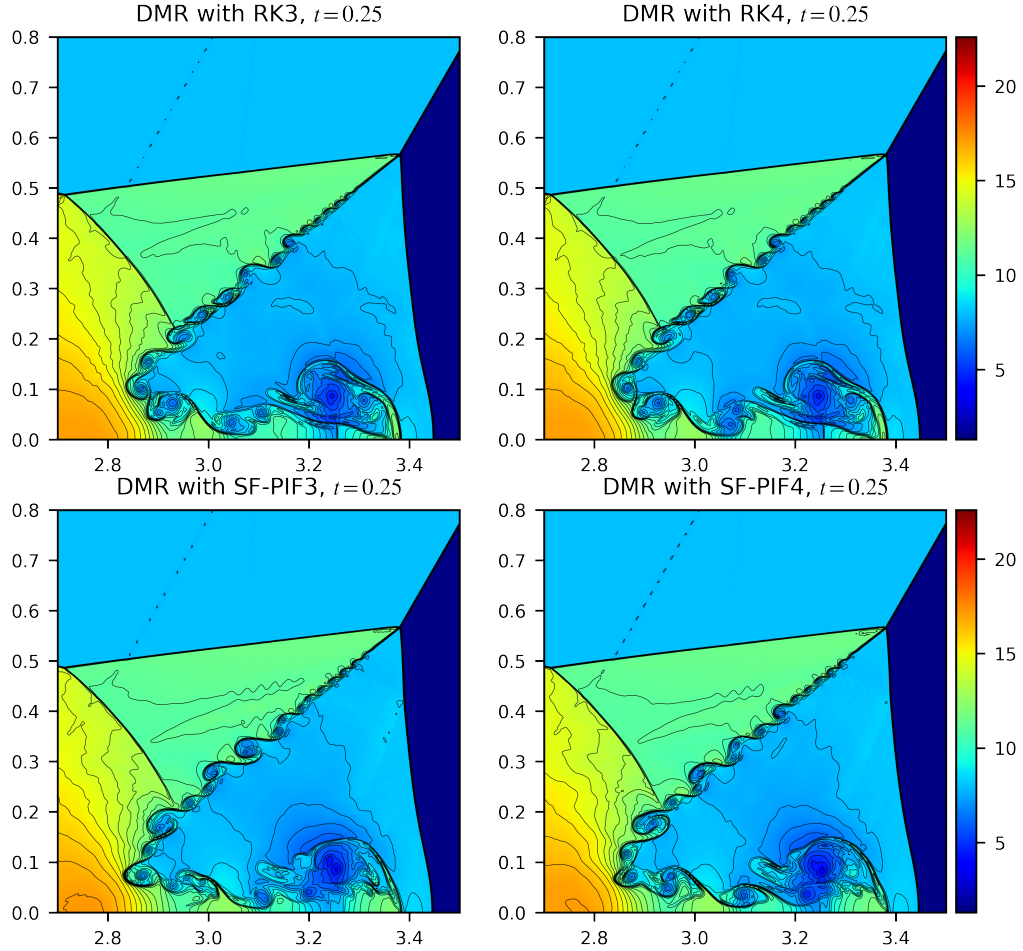


Figure 5.11: The density map of the double Mach reflection test at $t = 0.25$ zoomed-in near the jet. Forty levels of contour lines are over-plotted in solid black curves with the same range of the color map. All simulation results are performed on a 4096×2048 grid resolution. **Left column:** The solutions using RK3 (top) and SF-PIF3 (bottom). **Right column:** The solutions using RK4 (top) and SF-PIF4 (bottom).

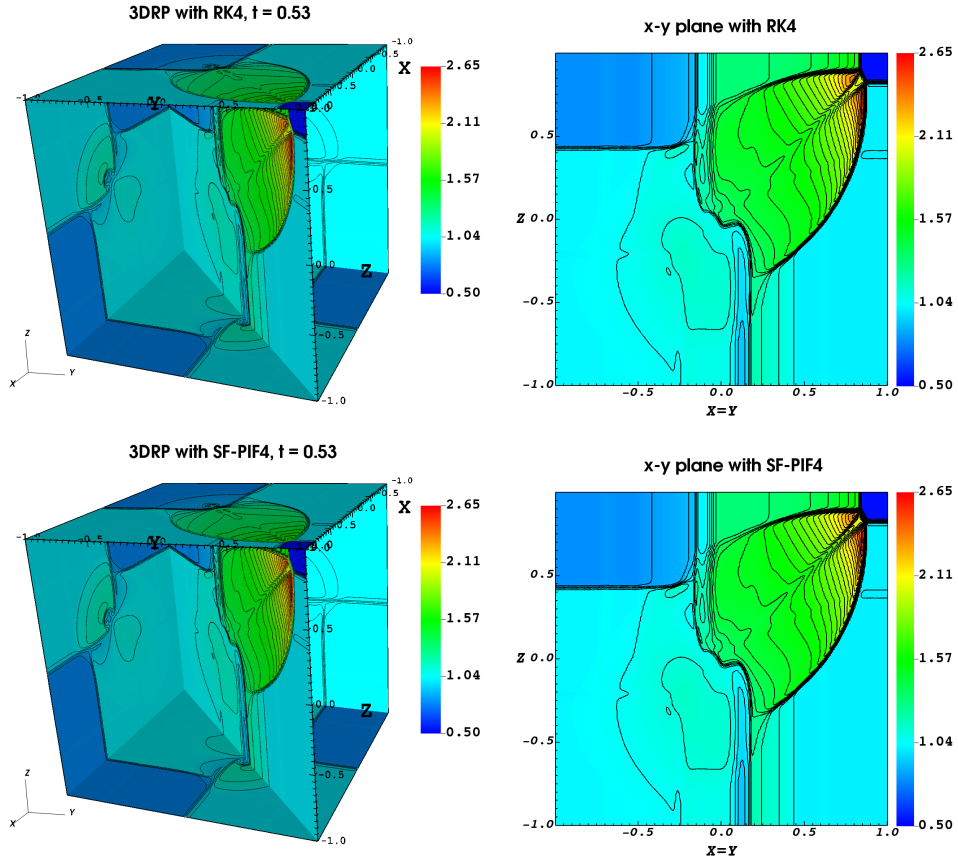


Figure 5.12: The density maps of the 3D Riemann problem test at $t = 0.53$. Forty contour lines are over-plotted. The left panels show each face’s geometrical views, while the right panels show the detailed picture of the diagonal planes. All simulations are performed on a $256 \times 256 \times 256$ grid resolution, solved with RK4 (**top**) and SF-PIF4 (**bottom**) solvers. The Courant condition, $C_{\text{cfl}} = 0.3$ is used for calculating the timestep.

5.2.4 3D Riemann problem

The 3D Riemann problem is the 3D extension of the 2D Riemann problem described in Section 5.2.2, introduced by Balsara [5]. Initially, each octant of the computational domain, $[-1, 1] \times [-1, 1] \times [-1, 1]$, has constant initial conditions, each of which will carry out 2D Riemann problem including the diagonal plane of the 3D computational cubic.

The results of 3D Riemann problem solved with RK4 and SF-PIF4 are illus-

Table 5.3: Performance results for the 3DRP test problem. All performance results (measured in seconds) are averaged over five simulation runs conducted on 16 nodes. Each node has 2×20 -core Intel Xeon Gold 6248 (Cascade Lake) CPUs, and the simulation utilized 512 parallel threads for each run.

Grid Resolution	RK3		SF-PIF3		RK4		SF-PIF4	
	CPU Time	Speedup						
$64 \times 64 \times 64$	1.79 s	1.0	1.09 s	0.61	2.95 s	1.64	2.67 s	1.49
$128 \times 128 \times 128$	15.62 s	1.0	7.63 s	0.49	25.88 s	1.66	18.97 s	1.21
$256 \times 256 \times 256$	191.00 s	1.0	82.02 s	0.43	321.34 s	1.68	201.40 s	1.05
$512 \times 512 \times 512$	2679.85 s	1.0	1173.54 s	0.44	4507.88 s	1.68	2817.78 s	1.05

trated in Fig. 5.12. The solutions were resolved on a $256 \times 256 \times 256$ grid resolution. The pseudo-color map ranges between $[0.5, 2.65]$, and 40 levels of contour lines are over-plotted using the same range. As depicted in Fig. 5.12, each surface of 3D computational domain evolves different 2D Riemann problems, including the diagonal plane which is separately plotted on the left panel. The recursive SF-PIF4 method is able to capture all the important features as much as the RK4 result, confirming the validity of the SF-PIF4 method in 3D simulation with strong shocks.

Table 5.3 shows the performance results for the 3D Riemann problem test on four grid resolutions. As shown in the table, the SF-PIF4 method demonstrates nearly the same performance as the *third*-order RK method, especially in high-resolution cases. It is important to note that the performance gains from the SF-PIF methods are more compensated on the high-resolution grids, which are indispensable for high fidelity physical simulation studies.

5.3 SF-PIF method with GP-WENO

As mentioned in Chapter 4, the SF-PIF method is an entirely independent temporal solver, which does not require any modification in the spatial high-order part of the simulation codes alike RK methods. As the purpose of demonstrat-

ing the portability of the SF-PIF method, this section will conduct several test problems using GP-WENO (instead of the conventional WENO as in the previous sections) described in Section 3.1.2 as a spatial high-order reconstruction method combining with SF-PIF methods for time integration strategy.

5.3.1 Hyperparameters

Unlike the polynomial-based reconstruction schemes, the GP method lacks any analytical considerations of the behavior of numerical errors with respect to the grid resolutions. This is further complicated by the use of nonlinear weighting in the GP-WENO method, which is necessary to capture the discontinuities appropriately. Consequently, direct numerical experiments should be conducted to predict the numerical errors from the GP-WENO method.

The GP-WENO method has two hyperparameters that need to be tuned, the length hyperparameter ℓ and the shock-capturing hyperparameter σ . The numerical errors from the 2D vortex advection problem with varying hyperparameters are illustrated in Fig. 5.13. The simulations are conducted on 400×400 grid resolutions, resolved with SF-PIF3 temporal solver with the same setup in Section 5.1.2. As dotted white lines represent, the minimum error has been found with $\ell = \sigma = 1$ for this systematic test.

Fig. 5.14 shows the slice plots by following the dotted lines in Fig. 5.13, showing the L_1 errors with the best choice of ℓ and σ . Surprisingly, the shock-capturing hyperparameter σ affects the solution accuracy, even though the solution is entirely smooth. Theoretically speaking, the vortex advection test is a nonlinear smooth problem, and σ only plays a role in the presence of a shock discontinuity; thus, it has to have the same errors across all sigma values. The different errors with varying sigma in the smooth problem are the indication of numerical errors

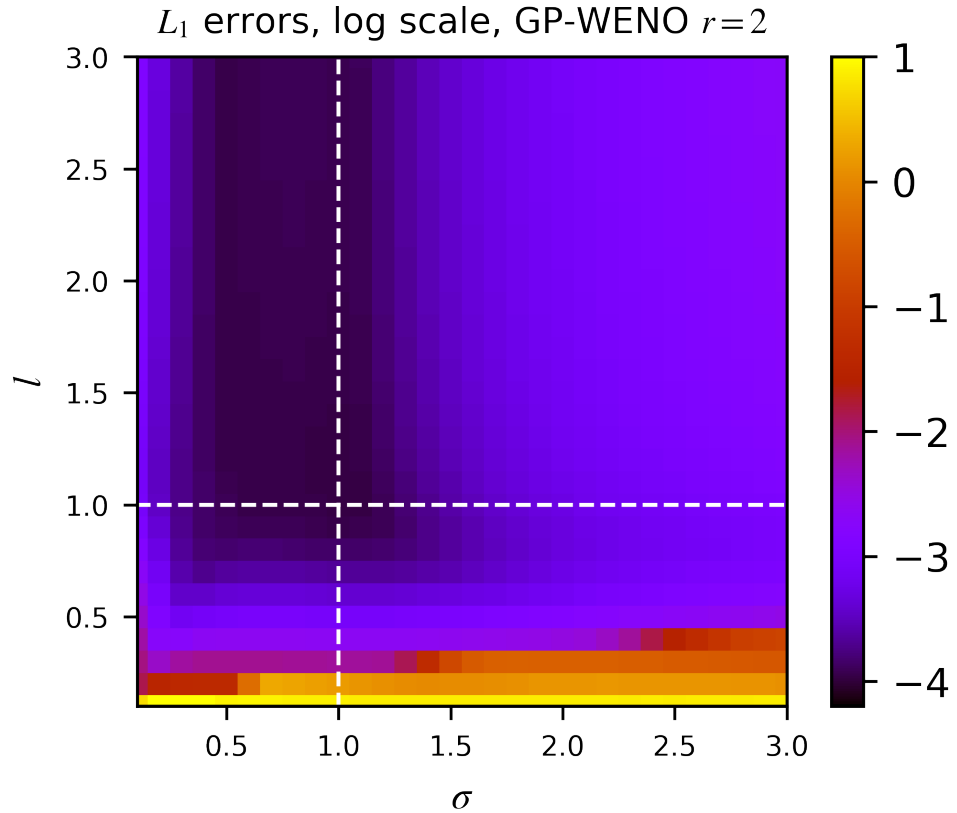


Figure 5.13: The log of L_1 errors of vortex advection problem solved by GP-WENO and SF-PIF3 on a 400×400 grid resolution. The radius of GP-WENO stencil is $r = 2$, which is the same stencil size of the fifth-order WENO method. The white dotted-lines are represent the hyperparameters of minimum error.

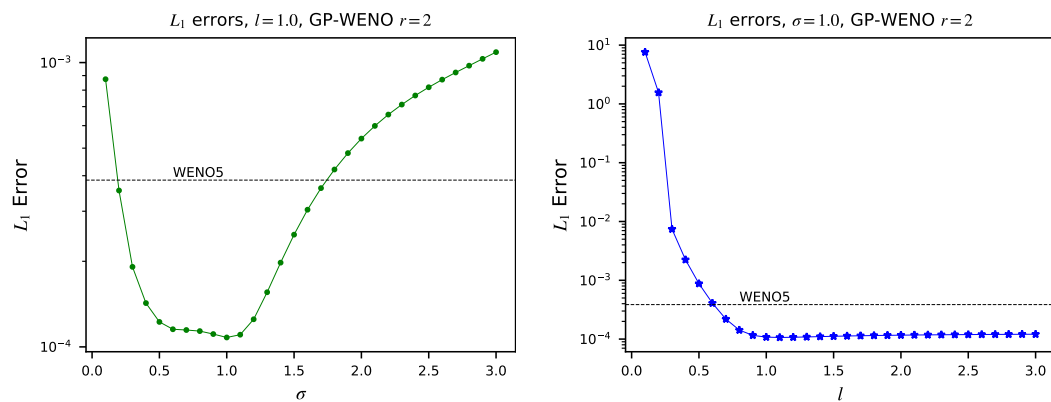


Figure 5.14: The slices of Fig. 5.13 at the minimum error. The horizontal dotted line is the target error obtained from WENO method with same configurations.

in calculating nonlinear weights of GP-WENO. This could be arisen from calculating the linear weights, (i.e., solving the overdetermined system Eq. (3.37)) or calculating smoothness indicators in Eq. (3.39), which requires further studies. Nonetheless, since the numerical solvers are involved in calculating both the linear weights and smoothness indicators, e.g., least square method and QR algorithm, numerical errors are inevitable in GP-WENO nonlinear weights.

5.3.2 2D Riemann problem: Configuration 3

what else...

Chapter 6

Conclusion

Bibliography

- [1] Antxón Alberdi, JL Gómez Fernández, Event Horizon Telescope Collaboration, et al. First m87 event horizon telescope results. i. the shadow of the supermassive black hole. 2019.
- [2] Francisco Alcrudo and Pilar Garcia-Navarro. A high-resolution Godunov-type scheme in finite volumes for the 2D shallow-water equations. *International Journal for Numerical Methods in Fluids*, 16(6):489–505, 1993.
- [3] Heng-Bin An, Ju Wen, and Tao Feng. On finite difference approximation of a matrix-vector product in the Jacobian-free Newton-Krylov method. *Journal of Computational and Applied Mathematics*, 236(6):1399–1409, 2011.
- [4] Norbert Attig, Paul Gibbon, and Th Lippert. Trends in supercomputing: The european path to exascale. *Computer physics communications*, 182(9):2041–2046, 2011.
- [5] Dinshaw S Balsara. Three dimensional HLL Riemann solver for conservation laws on structured meshes; application to Euler and magnetohydrodynamic flows. *Journal of Computational Physics*, 295:1–23, 2015.
- [6] Dinshaw S Balsara. Higher-order accurate space-time schemes for computational astrophysics—part I: finite volume methods. *Living reviews in computational astrophysics*, 3(1):2, 2017.
- [7] Dinshaw S Balsara, Sudip Garain, and Chi-Wang Shu. An efficient class of weno schemes with adaptive order. *Journal of Computational Physics*, 326:780–804, 2016.
- [8] Dinshaw S Balsara, Chad Meyer, Michael Dumbser, Huijing Du, and Zhiliang Xu. Efficient implementation of ADER schemes for Euler and magnetohydrodynamical flows on structured meshes—speed comparisons with Runge-Kutta methods. *Journal of Computational Physics*, 235:934–969, 2013.
- [9] Dinshaw S Balsara, Tobias Rumpf, Michael Dumbser, and Claus-Dieter Munz. Efficient, high accuracy ADER-WENO schemes for hydrodynam-

- ics and divergence-free magnetohydrodynamics. *Journal of Computational Physics*, 228(7):2480–2516, 2009.
- [10] Dinshaw S Balsara and Chi-Wang Shu. Monotonicity preserving weighted essentially non-oscillatory schemes with increasingly high order of accuracy. *Journal of Computational Physics*, 160(2):405–452, 2000.
 - [11] Marsha J Berger and Phillip Colella. Local adaptive mesh refinement for shock hydrodynamics. *Journal of computational Physics*, 82(1):64–84, 1989.
 - [12] Marsha J Berger and Randall J Leveque. Adaptive mesh refinement using wave-propagation algorithms for hyperbolic systems. *SIAM Journal on Numerical Analysis*, 35(6):2298–2316, 1998.
 - [13] Rafael Borges, Monique Carmona, Bruno Costa, and Wai Sun Don. An improved weighted essentially non-oscillatory scheme for hyperbolic conservation laws. *Journal of Computational Physics*, 227(6):3191–3211, 2008.
 - [14] Peter N Brown and Youcef Saad. Hybrid Krylov methods for nonlinear systems of equations. *SIAM Journal on Scientific and Statistical Computing*, 11(3):450–481, 1990.
 - [15] Paweł Buchmüller and Christiane Helzel. Improved accuracy of high-order weno finite volume methods on cartesian grids. *Journal of Scientific Computing*, 61(2):343–368, 2014.
 - [16] Marcos Castro, Bruno Costa, and Wai Sun Don. High order weighted essentially non-oscillatory weno-z schemes for hyperbolic conservation laws. *Journal of Computational Physics*, 230(5):1766–1792, 2011.
 - [17] Chaó-Kuang Chen and Shing-Huei Ho. Application of differential transformation to eigenvalue problems. *Applied mathematics and computation*, 79(2-3):173–188, 1996.
 - [18] Andrew J Christlieb, Xiao Feng, Yan Jiang, and Qi Tang. A high-order finite difference weno scheme for ideal magnetohydrodynamics on curvilinear meshes. *SIAM Journal on Scientific Computing*, 40(4):A2631–A2666, 2018.
 - [19] Andrew J Christlieb, Yaman Guclu, and David C Seal. The Picard integral formulation of weighted essentially nonoscillatory schemes. *SIAM Journal on Numerical Analysis*, 53(4):1833–1856, 2015.
 - [20] Phillip Colella and Paul R Woodward. The piecewise parabolic method (PPM) for gas-dynamical simulations. *Journal of computational physics*, 54(1):174–201, 1984.

- [21] Nelida Črnjarić-Žic, S Vuković, and Luka Sopta. On different flux splittings and flux functions in weno schemes for balance laws. *Computers & fluids*, 35(10):1074–1092, 2006.
- [22] L Del Zanna, N Bucciantini, and P Londrillo. An efficient shock-capturing central-type scheme for multidimensional relativistic flows-ii. magnetohydrodynamics. *Astronomy & Astrophysics*, 400(2):397–413, 2003.
- [23] L Del Zanna, O Zanotti, N Bucciantini, and P Londrillo. Echo: a eulerian conservative high-order scheme for general relativistic magnetohydrodynamics and magnetodynamics. *Astronomy & Astrophysics*, 473(1):11–30, 2007.
- [24] Anargiros I Delis and Th Katsaounis. Numerical solution of the two-dimensional shallow water equations by the application of relaxation methods. *Applied Mathematical Modelling*, 29(8):754–783, 2005.
- [25] Wai-Sun Don, Zhen Gao, Peng Li, and Xiao Wen. Hybrid compact-WENO finite difference scheme with conjugate Fourier shock detection algorithm for hyperbolic conservation laws. *SIAM Journal on Scientific Computing*, 38(2):A691–A711, 2016.
- [26] Jack Dongarra, Jeffrey Hittinger, John Bell, Luis Chacon, Robert Falgout, Michael Heroux, Paul Hovland, Esmond Ng, Clayton Webster, and Stefan Wild. Applied mathematics research for exascale computing. Technical report, Lawrence Livermore National Lab.(LLNL), Livermore, CA (United States), 2014.
- [27] Michael Dumbser, Dinshaw S Balsara, Eleuterio F Toro, and Claus-Dieter Munz. A unified framework for the construction of one-step finite volume and discontinuous galerkin schemes on unstructured meshes. *Journal of Computational Physics*, 227(18):8209–8253, 2008.
- [28] Michael Dumbser, Martin Käser, Vladimir A Titarev, and Eleuterio F Toro. Quadrature-free non-oscillatory finite volume schemes on unstructured meshes for nonlinear hyperbolic systems. *Journal of Computational Physics*, 226(1):204–243, 2007.
- [29] Francesco Fambri, Michael Dumbser, and Olindo Zanotti. Space-time adaptive ADER-DG schemes for dissipative flows: Compressible Navier-Stokes and resistive MHD equations. *Computer Physics Communications*, 220:297–318, 2017.
- [30] Kyle Gerard Felker and James M Stone. A fourth-order accurate finite volume method for ideal mhd via upwind constrained transport. *Journal of Computational Physics*, 375:1365–1400, 2018.

- [31] Jim A Gaffney, Scott T Brandon, Kelli D Humbird, Michael KG Kruse, Ryan C Nora, J Luc Peterson, and Brian K Spears. Making inertial confinement fusion models more predictive. *Physics of Plasmas*, 26(8):082704, 2019.
- [32] Charles William Gear and Youcef Saad. Iterative solution of linear equations in ODE codes. *SIAM journal on scientific and statistical computing*, 4(4):583–601, 1983.
- [33] SK Godunov. A difference scheme for numerical computation of discontinuous solutions of fluid dynamics. *Mat. Sb*, 47:271–306, 1959.
- [34] Sigal Gottlieb, David I Ketcheson, and Chi-Wang Shu. *Strong stability preserving Runge-Kutta and multistep time discretizations*. World Scientific, 2011.
- [35] Sigal Gottlieb and Chi-Wang Shu. Total variation diminishing Runge-Kutta schemes. *Mathematics of computation of the American Mathematical Society*, 67(221):73–85, 1998.
- [36] Sigal Gottlieb, Chi-Wang Shu, and Eitan Tadmor. Strong stability-preserving high-order time discretization methods. *SIAM review*, 43(1):89–112, 2001.
- [37] Brian M Haines, Gary P Grim, James R Fincke, Rahul C Shah, Chad J Forrest, Kevin Silverstein, Frederic J Marshall, Melissa Boswell, Malcolm M Fowler, Robert A Gore, et al. Detailed high-resolution three-dimensional simulations of omega separated reactants inertial confinement fusion experiments. *Physics of Plasmas*, 23(7):072709, 2016.
- [38] Ami Harten, Bjorn Engquist, Stanley Osher, and Sukumar R Chakravarthy. Uniformly high order accurate essentially non-oscillatory schemes, iii. In *Upwind and high-resolution schemes*, pages 218–290. Springer, 1987.
- [39] WH Hui, PY Li, and ZW Li. A unified coordinate system for solving the two-dimensional Euler equations. *Journal of Computational Physics*, 153(2):596–637, 1999.
- [40] Oliver James, Eugénie von Tunzelmann, Paul Franklin, and Kip S Thorne. Gravitational lensing by spinning black holes in astrophysics, and in the movie interstellar. *Classical and Quantum Gravity*, 32(6):065001, 2015.
- [41] Guang-Shan Jiang and Chi-Wang Shu. Efficient implementation of weighted ENO schemes. *Journal of computational physics*, 126(1):202–228, 1996.
- [42] Soshi Kawai. Divergence-free-preserving high-order schemes for magnetohydrodynamics: an artificial magnetic resistivity method. *Journal of Computational Physics*, 251:292–318, 2013.

- [43] Friedemann Kemm. On the proper setup of the double Mach reflection as a test case for the resolution of gas dynamics codes. *Computers & Fluids*, 132:72–75, 2016.
- [44] Dana A Knoll and David E Keyes. Jacobian-free Newton-Krylov methods: a survey of approaches and applications. *Journal of Computational Physics*, 193(2):357–397, 2004.
- [45] Dana A Knoll, H Park, and Kord Smith. Application of the Jacobian-free Newton-Krylov method to nonlinear acceleration of transport source iteration in slab geometry. *Nuclear Science and Engineering*, 167(2):122–132, 2011.
- [46] Peter Lax. Systems of conservation laws. Technical report, LOS ALAMOS NATIONAL LAB NM, 1959.
- [47] Dongwook Lee, Hugues Faller, and Adam Reyes. The piecewise cubic method (pcm) for computational fluid dynamics. *Journal of Computational Physics*, 341:230–257, 2017.
- [48] Youngjun Lee and Dongwook Lee. A single-step third-order temporal discretization with jacobian-free and hessian-free formulations for finite difference methods. *Journal of Computational Physics*, 427:110063, 2021.
- [49] Youngjun Lee, Dongwook Lee, and Adam Reyes. A recursive system-free single-step temporal discretization method for finite difference methods. *Journal of Computational Physics: X*, 12:100098, 2021.
- [50] Richard Liska and Burton Wendroff. Comparison of several difference schemes on 1D and 2D test problems for the Euler equations. *SIAM Journal on Scientific Computing*, 25(3):995–1017, 2003.
- [51] Xu-Dong Liu, Stanley Osher, Tony Chan, et al. Weighted essentially non-oscillatory schemes. *Journal of computational physics*, 115(1):200–212, 1994.
- [52] Peter McCorquodale and Phillip Colella. A high-order finite-volume method for conservation laws on locally refined grids. *Communications in Applied Mathematics and Computational Science*, 6(1):1–25, 2011.
- [53] Jena Meinecke, HW Doyle, Francesco Miniati, Anthony R Bell, R Bingham, Robert Crowston, RP Drake, Milad Fatenejad, Michel Koenig, Yasuhiro Kuroamitsu, et al. Turbulent amplification of magnetic fields in laboratory laser-produced shock waves. *Nature Physics*, 10(7):520–524, 2014.
- [54] Andrea Mignone, Petros Tzeferacos, and Gianluigi Bodo. High-order conservative finite difference GLM–MHD schemes for cell-centered MHD. *Journal of Computational Physics*, 229(17):5896–5920, 2010.

- [55] Gino Montecinos and Eleuterio Toro. Solver for the generalized riemann problem for balance laws with stiff source terms: the scalar case. In *Hyperbolic Problems: Theory, Numerics and Applications (In 2 Volumes)*, pages 576–583. World Scientific, 2012.
- [56] Gino I Montecinos and Dinshaw S Balsara. A simplified cauchy-kowalewskaya procedure for the local implicit solution of generalized riemann problems of hyperbolic balance laws. *Computers & Fluids*, 202:104490, 2020.
- [57] Gino I Montecinos and Eleuterio F Toro. Reformulations for general advection–diffusion–reaction equations and locally implicit ader schemes. *Journal of Computational Physics*, 275:415–442, 2014.
- [58] Matthew R Norman. Algorithmic improvements for schemes using the ADER time discretization. *Journal of Computational Physics*, 243:176–178, 2013.
- [59] Matthew R Norman. A WENO-limited, ADER-DT, finite-volume scheme for efficient, robust, and communication-avoiding multi-dimensional transport. *Journal of Computational Physics*, 274:1–18, 2014.
- [60] Matthew R Norman and Hal Finkel. Multi-moment ADER-Taylor methods for systems of conservation laws with source terms in one dimension. *Journal of Computational Physics*, 231(20):6622–6642, 2012.
- [61] Adam Reyes, Dongwook Lee, Carlo Graziani, and Petros Tzeferacos. A new class of high-order methods for fluid dynamics simulations using gaussian process modeling: One-dimensional case. *Journal of Scientific Computing*, 76(1):443–480, 2018.
- [62] Adam Reyes, Dongwook Lee, Carlo Graziani, and Petros Tzeferacos. A variable high-order shock-capturing finite difference method with gp-weno. *Journal of Computational Physics*, 381:189–217, 2019.
- [63] Carsten W Schulz-Rinne. Classification of the Riemann problem for two-dimensional gas dynamics. *SIAM journal on mathematical analysis*, 24(1):76–88, 1993.
- [64] Carsten W Schulz-Rinne, James P Collins, and Harland M Glaz. Numerical solution of the Riemann problem for two-dimensional gas dynamics. *SIAM Journal on Scientific Computing*, 14(6):1394–1414, 1993.
- [65] David C Seal, Qi Tang, Zhengfu Xu, and Andrew J Christlieb. An explicit high-order single-stage single-step positivity-preserving finite difference WENO method for the compressible Euler equations. *Journal of Scientific Computing*, 68(1):171–190, 2016.

- [66] Chaopeng Shen, Jing-Mei Qiu, and Andrew Christlieb. Adaptive mesh refinement based on high order finite difference weno scheme for multi-scale simulations. *Journal of Computational Physics*, 230(10):3780–3802, 2011.
- [67] Chi-Wang Shu. Total-variation-diminishing time discretizations. *SIAM Journal on Scientific and Statistical Computing*, 9(6):1073–1084, 1988.
- [68] Chi-Wang Shu. Essentially non-oscillatory and weighted essentially non-oscillatory schemes for hyperbolic conservation laws. In *Advanced numerical approximation of nonlinear hyperbolic equations*, pages 325–432. Springer, 1998.
- [69] Chi-Wang Shu and Stanley Osher. Efficient implementation of essentially non-oscillatory shock-capturing schemes. *Journal of computational physics*, 77(2):439–471, 1988.
- [70] Chi-Wang Shu and Stanley Osher. Efficient implementation of essentially non-oscillatory shock-capturing schemes, ii. In *Upwind and High-Resolution Schemes*, pages 328–374. Springer, 1989.
- [71] Gary A Sod. A survey of several finite difference methods for systems of nonlinear hyperbolic conservation laws. *Journal of computational physics*, 27(1):1–31, 1978.
- [72] Seth C Spiegel, HT Huynh, and James R DeBonis. A survey of the isentropic Euler vortex problem using high-order methods. In *22nd AIAA Computational Fluid Dynamics Conference*, page 2444, 2015.
- [73] Raymond J Spiteri and Steven J Ruuth. A new class of optimal high-order strong-stability-preserving time discretization methods. *SIAM Journal on Numerical Analysis*, 40(2):469–491, 2002.
- [74] Raymond J Spiteri and Steven J Ruuth. Non-linear evolution using optimal fourth-order strong-stability-preserving Runge-Kutta methods. *Mathematics and Computers in Simulation*, 62(1-2):125–135, 2003.
- [75] James M Stone, Thomas A Gardiner, Peter Teuben, John F Hawley, and Jacob B Simon. Athena: a new code for astrophysical MHD. *The Astrophysical Journal Supplement Series*, 178(1):137, 2008.
- [76] Vladimir A Titarev and Eleuterio F Toro. ADER: Arbitrary high order Godunov approach. *Journal of Scientific Computing*, 17(1-4):609–618, 2002.
- [77] Vladimir A Titarev and Eleuterio F Toro. Finite-volume weno schemes for three-dimensional conservation laws. *Journal of Computational Physics*, 201(1):238–260, 2004.

- [78] Vladimir A Titarev and Eleuterio F Toro. ADER schemes for three-dimensional non-linear hyperbolic systems. *Journal of Computational Physics*, 204(2):715–736, 2005.
- [79] Eleuterio F Toro. *Shock-capturing methods for free-surface shallow flows*. John Wiley, 2001.
- [80] Eleuterio F Toro, RC Millington, and LAM Nejad. Towards very high order godunov schemes. In *Godunov methods*, pages 907–940. Springer, 2001.
- [81] Eleuterio F Toro and Gino I Montecinos. Implicit, semi-analytical solution of the generalized riemann problem for stiff hyperbolic balance laws. *Journal of Computational Physics*, 303:146–172, 2015.
- [82] P Tzeferacos, A Rigby, AFA Bott, AR Bell, R Bingham, A Casner, F Cattaneo, EM Churazov, J Emig, F Fiuzza, et al. Laboratory evidence of dynamo amplification of magnetic fields in a turbulent plasma. *Nature communications*, 9(1):1–8, 2018.
- [83] Bram Van Leer. Towards the ultimate conservative difference scheme. v. a second-order sequel to godunov’s method. *Journal of computational Physics*, 32(1):101–136, 1979.
- [84] Paul Woodward and Phillip Colella. The numerical simulation of two-dimensional fluid flow with strong shocks. *Journal of computational physics*, 54(1):115–173, 1984.
- [85] Olindo Zanotti and Michael Dumbser. Efficient conservative ADER schemes based on WENO reconstruction and space–time predictor in primitive variables. *Computational astrophysics and cosmology*, 3(1):1, 2016.
- [86] Rui Zhang, Mengping Zhang, and Chi-Wang Shu. On the order of accuracy and numerical performance of two classes of finite volume weno schemes. *Communications in Computational Physics*, 9(3):807–827, 2011.
- [87] Tong Zhang and Yu Xi Zheng. Conjecture on the structure of solutions of the Riemann problem for two-dimensional gas dynamics systems. *SIAM Journal on Mathematical Analysis*, 21(3):593–630, 1990.